LITHIUM DEPLETION BOUNDARY AGES OF YOUNG PLANET-HOSTING STELLAR ASSOCIATIONS

Mackenna L. Wood

A dissertation submitted to the faculty of the University of North Carolina at Chapel Hill in partial fulfillment of the requirements for the degree of Doctor of Philosophy in the Department of Physics and Astronomy.

Chapel Hill
2023

Approved by:

Andrew Mann

Jaqueline Faherty

Julieta Gruzco

Nicholas Law

Gregory C. Sloan

©2023
Mackenna L. Wood
ALL RIGHTS RESERVED

ABSTRACT

Mackenna L. Wood: Lithium Depletion Boundary Ages of Young Planet-Hosting Stellar Associations
(Under the direction of Andrew Mann)

Stellar associations - groups of coeval, co-moving stars - are fundamental to our understanding of stellar ages and critical for the study of stellar and planetary evolution. All stellar age measurements, with the sole exception of the Sun, are based on the ages of stellar associations or on methods developed through studies of associations. Young associations in particular provide excellent benchmarks to study stellar and planetary evolution, as many important evolutionary steps occur during the first billion years of a star's existence. The combination of the *Gaia*, *Kepler*, and *TESS* missions have ushered in a golden age for studying stellar and planetary evolution. These studies will require both robust, accurate age measurements for stellar associations and numerous planets within those associations to study.

However, commonly used methods of measuring age, such as isochrone fitting, are imprecise and depend strongly on poorly-understood physical parameters such as magnetic fields. An alternative, more precise way to achieve association ages, the Lithium Depletion Boundary (LDB) method is less model-dependent but requires observationally expensive spectra of low-mass association members. Moreover, less than one hundred young ($< 1Gyr$) planets have yet been discovered, offering few vantage points into a highly important and dynamic time period.

In this thesis I characterize several nearby, planet-hosting associations and planets within them. I clarify the associations' membership and kinematics using 6D astrometric data available from the *Gaia* mission, and the `BANYAN` Σ tool for association membership. I

measure the ages of the associations using the LDB method and spectra obtained on the Goodman HTS on the SOAR telescope. When possible these ages are confirmed using additional age-measurement methods, making the resulting ages robust and accurate.

The products of this thesis are new ages and membership lists for several previously known associations and subpopulations (Musca, LCC-A, LCC-B, LCC-C, Carina, Theia 92, Theia 113), the discovery and characterization of an entirely new association (MELANGE-4), and the discovery or confirmation of three exoplanets within those associations. Collectively, the associations studied here contain thousands of stars and 7 known planets, forming an impressive sample of accurately age-dated stars and planets on which future studies can rely.

To my mother who instilled in me a love for science.

ACKNOWLEDGEMENTS

I would like to acknowledge the many people who supported and encouraged me throughout my graduate career. Without them, this dissertation would never have been possible. My family, whose love and support were indispensable. Christopher, who continuously offered support, distraction, and proofreading as needed. My advisor, Andrew Mann, whose guidance and teaching gave me the confidence to ask questions and the tools to answer them. My friends and labmates who made struggling through code and long nights at the telescope fun. Juan, Sergio, Carlos, Rodrigo, Patrico, and all the people at SOAR who helped through many nights of observing.

TABLE OF CONTENTS

LIST OF TABLES

LIST OF FIGURES

LIST OF ABBREVIATIONS AND SYMBOLS

CMD	Color Magnitude Diagram
DSS	Digital Sky Survey
ESO	European Southern Observatory
LCC	Lower Centaurus Crux
LDB	Lithium Depletion Boundary
MS	Main Sequence
PDSCAP	Pre-Search Data Conditioning Simple Aperture Photometry
PMS	Pre-Main Sequence
PSF	Point-Spread Function
RV	Radial Velocity
Sco-Cen	Scorpius Centaurus OB Association
SED	Spectral Energy Distribution
SNR	Signal-to-Noise Ratio
SOAR	Southern Astrophysical Research (Telescope)
TESS	Transiting Exoplanet Survey Satellite
TOI	*TESS* Object of Interest
Tuc-Hor	Tucana-Horologium Stellar Association
α	Right Ascension
βPic	β Pictoris Moving Group
δ	Declination
π	Parallax
ρ_*	Stellar Density

CHAPTER 1: INTRODUCTION

Stellar associations are the foundation of our entire understanding of stellar and planetary formation and evolution. The remnants of stellar nurseries, where dozens or hundreds of stars formed together, stellar associations are astronomical "experiments", showing a single stage of evolution and set of initial conditions across a wide range of stellar types. Studies of associations at various ages are used to reconstruct the evolutionary processes shaping stars and planets and illuminate the collapse of giant molecular clouds and the triggers of star formation. However for these studies to be accurate, the age measurements of the associations which provide the framework for them must be accurate and precise.

Unfortunately, current age measurement methods are rife with uncertainty: the method, model, and membership list used for a given age measurement all have the potential to significantly change the result. Different methods, for example the fitting of evolutionary models to an association's Color-Magnitude Diagram, or fitting the magnitude of an association's Lithium Depletion Boundary (LDB), can produce ages varying by up to a factor of two (Malo et al., 2014; Binks et al., 2022). Moreover, applying a single method to stars with different underlying physics produces different ages. A single CMD isochrone, fitting the F-G members of an association, is significantly underluminous when applied to M dwarfs of the same association, such that a fit to only M-dwarfs would result in a much younger age than a fit to only F-G dwarfs (e.g., Malo et al., 2014; Feiden, 2016; Binks et al., 2021). Ages derived by comparison to different evolutionary models are similarly discrepant, with different treatment of convective mixing (Dotter et al., 2008; Baraffe et al., 2015), magnetic models (Feiden, 2016), or stellar activity (Somers et al., 2020) resulting in different ages. Finally, it is possible for the membership list used to derive an age to have a significant effect. Two different measurements of the Carina association's age, both using CMD isochrone fits,

resulted in ages of $13^{+1.1}_{-0.6}$ Myr (Booth et al., 2021) and 45^{+11}_{-7} Myr (Bell et al., 2015), largely based on Booth et al. (2021)'s inclusion of a high-mass, evolved star as a member of the association. These differences in derived ages caused by using different methods, models, or membership lists (e.g., Booth et al., 2021), cause significant uncertainty in individual age measurements. Many associations have multiple age measurements varying by $\gtrsim 100\%$ (see Figure 1.1).

The Lithium Depletion Boundary (LDB) method is thought to be both highly accurate, and model independent, due to its reliance on the well understood process of Li depletion in fully-convective low mass stars. Ages derived using LDB vary by only $\sim 5-10\%$ with changes in model (Burke et al., 2004; Tognelli et al., 2015), making them significantly more robust than ages derived with isochrone fitting or other methods. Unfortunately, the necessity for mid-resolution optical spectra of the faintest, lowest mass members of an association means that this method has not been applied to very many associations. If applied to a greater number of associations, spanning a range of ages, the LDB method has the potential to provide a strong foundation against which other age methods can be calibrated.

New survey missions and computational methods have made it much easier to identify associations and association members, enabling more accurate and complete membership lists. Utilizing the 6D astrometric information available from the *Gaia* mission, it is possible to fully calculate the galactic positions and velocities of stars, avoiding confusion caused by projection effects, and create accurate kinematic definitions of associations. New methods, such as clustering algorithms, have been used to find new associations and divide existing ones into subpopulations, preventing pollution of membership lists between neighboring populations. Using these new tools we can create more accurate membership lists, which combined with the precision of LDB age measurements significantly reduce the uncertainty in the resulting age measurements.

With accurate ages, associations are valuable tools for studying the processes by which stars are formed and shaped. The classical view of stellar associations assumes they form

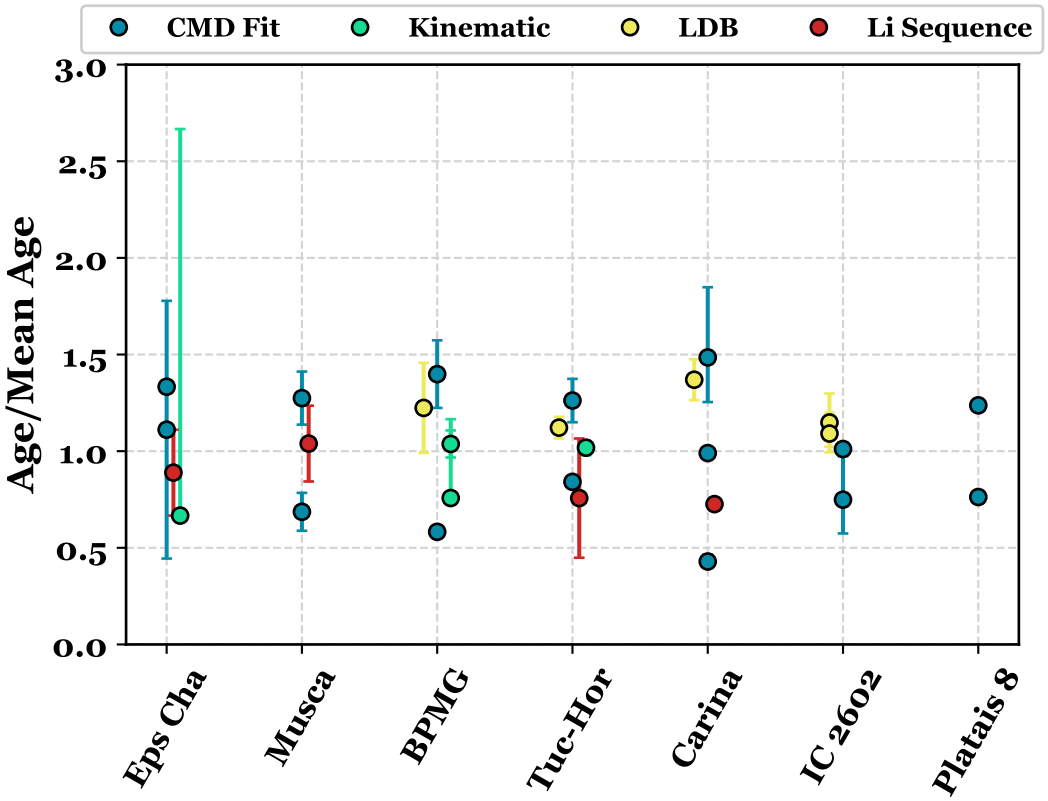

Figure 1.1 Literature age measurements of nearby stellar associations. Age measurements derived using different methods, models, or membership lists are shown for several nearby young stellar associations, with color indicating methods. Age variation by 100% is common. Error bars show 1σ uncertainties, but reflect only the uncertainty of a single method or observable and not the underlying uncertainty of all age measurements. Ages are taken from: Musca - Goldman et al. (2018); Kerr et al. (2021); Mann et al. (2022), ϵ Cha - Torres et al. (2008); Kerr et al. (2021); Miret-Roig et al. (2018); Dickson-Vandervelde et al. (2021), β Pic - Torres et al. (2008); Miret-Roig et al. (2018); Crundall et al. (2019); Mentuch et al. (2008); Binks & Jeffries (2014); Bell et al. (2015), Tuc-Hor - Torres et al. (2008); Mentuch et al. (2008); Kraus et al. (2014); Bell et al. (2015); Miret-Roig et al. (2018); Crundall et al. (2019), Carina - Torres et al. (2008); Bell et al. (2015); Booth et al. (2021); Wood et al. (in prep), IC 2602 - Kerr et al. (2021); Randich et al. (2018); Dobbie et al. (2010), Platais 8 - Gagné et al. (2021); Kerr et al. (2021). Errors are not shown for ages taken from Gagné et al. (2021); Torres et al. (2008) or Kraus et al. (2014).

when a giant cloud of molecular hydrogen collapses, triggering simultaneous star formation. However, recent studies have found granularity within individual associations, suggesting much smaller formation scales involving only a few stars (Pecaut & Mamajek, 2016), opening new questions about the triggers and structure of star formation (e.g., Zucker et al., 2022b). Following their formation, stars undergo radical changes as they progress from proto-stars to disk-bearing pre-main sequence (PMS) stars onto the hydrogen burning main sequence (MS), and then to advanced stages of stellar evolution. By examining stars at various stages of this evolutionary sequence, the details and mechanisms involved can be reconstructed.

Stellar associations also provide the richest source of young planets, hosting most of the young planets yet discovered (Miyakawa et al., 2022), and the most accurate sources for measuring their ages (Soderblom et al., 2014).

The first hundred million years after a planet's formation are critical for determining its final size, orbital dynamics, and atmospheric composition. With ever more discoveries of young planets (e.g., Mann et al., 2016a; Bouma et al., 2022), and the advent of JWST to study them, we will soon have unprecedented insight into the composition, atmospheres, and dynamics of young exoplanets. But, without a solid foundation of accurate and precise age measurements, at best we will learn nothing, and at worst draw erroneous conclusions about the evolution of planetary systems. For example, the masses of directly imaged planets (e.g., Rameau et al., 2013; Bohn et al., 2020a) are determined by comparing their luminosity to planet evolution models at a given age. Age uncertainty of only a few Myr leads to a mass uncertainty of $3M_{Jup}$ or more. This dramatically changes planet characterization and can cause brown dwarfs to be incorrectly classified as gas giant planets (Hinkley et al., 2013). Of 19 directly imaged planets cataloged by Lazzoni et al. (2022), seven are within 3 or $4M_{Jup}$ of the mass limit for brown dwarfs. Only with an accurate picture of both the membership and ages of stellar associations can we correctly place planets in an evolutionary sequence and gain understanding of the processes which govern planet formation and evolution.

In this dissertation, I examine of a number of nearby, planet-hosting young associations, including the newly discovered MELANGE-4 association. I measure their ages using the Lithium Depletion Boundary method and confirm using a combination of other methods. By using both the highly accurate and precise LDB method and other methods I am able to determine a precise final age for each association. These ages will allow more detailed studies of stellar evolution. They will also empower understanding of planetary evolution, as there are seven known young planets within the studied associations, including the largest known planet orbiting an M-dwarf star (Mann et al., 2022), and two of the smallest known < 100 Myr planets (Wood et al., 2023).

In the remainder of Chapter 1 I discuss the properties of young stars and planets, stellar associations, and the methods which can be used to determine their ages. In Chapter 2 I present our characterization and age measurement for several subpopulations with Lower Centaurus Crux (LCC). The discovery and characterization of a new association, which we name MELANGE-4, and two super-Earth sized planets within it is discussed in Chapter 3. Chapter 4 covers the age measurement of the Carina association, a member of the Carina-Columba complex, and two additional groups which are candidate members of the same complex. Finally, I summarize the results of this work and discuss the outlook for future studies of association ages in Chapter 5.

1.1 Young Stars as Individuals

While in most of this thesis I will discuss the bulk properties of young stars in associations, in this section I will talk about properties of individual young stars.

1.1.1 Magnetic Fields and Stellar Activity

Magnetic fields and activity are critical for understanding stellar parameters and observations, particularly of young stars. Magnetic fields within stars give rise to a variety of phenomena which fall under the umbrella term "stellar activity" (e.g., Linsky, 2017). Mag-

netic field strength can be observed in several ways. Strong magnetic fields produce Zeeman splitting of spectral lines. Certain spectral lines are magnified in the presence of strong fields, especially Ca II, H and K lines. And while less directly related to magnetic field strength, surface features such as spots, flares, and prominences are correlated with high magnetic activity.

Observations of these phenomena have shown that young stars are more magnetically active than old or field stars. In solar type stars this activity-age relation arises because the magnetic fields are generated by the shearing at the transition between the radiative and convective layers as the star rotates. The faster rotation of young stars (see Section 1.1.2), creates a stronger magnetic field.

The nature of magnetic fields in fully convective M-dwarfs is not fully understood, as there is no tachocline to generate a magnetic fields through shearing. Nevertheless a correlation between age and activity has been observed in a variety of studies (Kiman et al., 2021).

One manifestation of this age-activity relation in M-dwarfs is strong chromospheric Hα emission, arising from chromospheric heating of hydrogen (e.g., Kiman et al., 2021). This appears as a strong emission line in M-dwarfs due to the chromosphere being optically thin and the background continuum faint (Linsky, 2017). A large fraction of M-dwarfs are observed to show Hα emission (Linsky, 2017), making the presence of Hα emission in a individual stars an uncertain indicator of youth. Kiman et al. (2021) looked at Hα emission in congregate, measuring the fraction of dwarfs in a certain age bin which exhibited Hα activity. They found that fraction of Hα active M-dwarfs decreases with age with a mass-dependence, so that at ages $\gtrsim$ 500 Myr few M0-M3 dwarfs exhibit Hα emission, but late M's show Hαemission at even very old ages, so that $\sim$ 80% of field M7's are active (Kiman et al., 2021).

In active PMS M-dwarfs, magnetic fields may play an important role in determining fundamental stellar properties (Feiden, 2016). By using models incorporating magnetic fields,

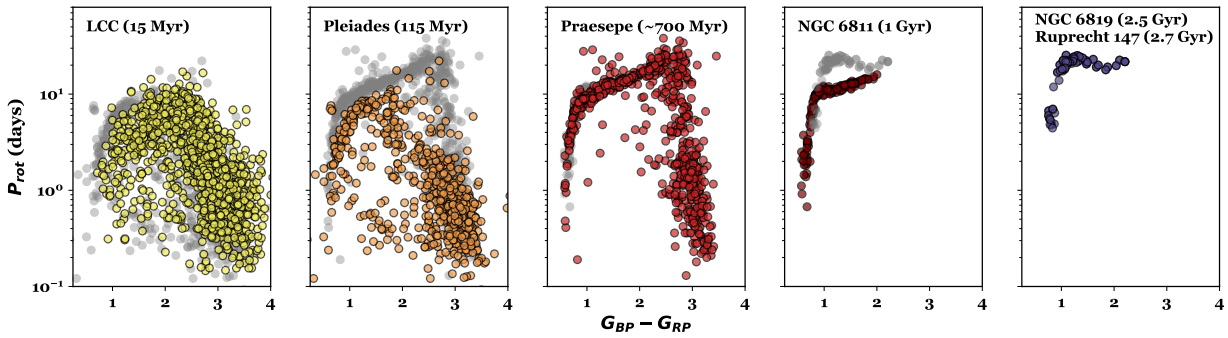

Figure 1.2 Period-Color diagrams showing the rotation sequences of several nearby associations. Association age increases from left to right, with stars spinning down and converging into the fast and slow rotator sequences. In each plot gray dots show the next oldest association. Data are taken from Curtis et al. (2020); Rebull et al. (2022).

more consistent age measurements using different methods can be achieved (e.g., Feiden, 2016; Binks et al., 2021).

Overall, while the effects of magnetic fields are critical for understanding young stars, they cannot be used for age determination, because age-activity relations are not well defined and have significant scatter (Soderblom et al., 2014).

1.1.2 Rotation

All stars rotate, such that Barnes (2003) claim that rotation is the most fundamental observational characteristic after brightness, color, and possibly metallicity. As stars age, magnetic braking slows their rotation, a process known as spin-down. This process is more complex than the initially proposed braking law, $P_{rot} \propto t^n$(Skumanich, 1972), with both slow-rotating and fast-rotating sequences of stars (Barnes, 2003). In young stars this picture is further complicated as stars do not begin spinning down until they reach the hydrogen-fusing main-sequence (MS). For low-mass M-dwarfs this does not occur until long after mid- and high- mass stars, so that in coeval groups of stars M-dwarfs will not begin spinning down until ages of $100 - 150$ Myr. Despite this complexity, studies of rotation in open clusters have shown a clear pattern of rotation evolution with age, shown in Figure 1.2.

Combined with the high spot incidence of young stars, the fast rotation means that we can use light curves to measure the rotation speed. The abundance of light-curve data available from surveys such as *K*2 and *TESS* have increased the ease with which rotation periods of stars can be measured (e.g., Rebull et al., 2018; Rebull et al., 2022), making rotation an even more important observable characteristic. Age-dependent and readily measured from easily found data, rotation periods can function as an important indicator of youth in stars. A rotation period of $\lesssim 10 - 50$ days can be considered an indicator that a star is young (Newton et al., 2016; Kounkel et al., 2022b) However significant scatter in the relationship between color and P_{rot}, and complications from factors such as binarity, mean that this cannot be used as a direct measure of age for any individual star.

1.1.3 Li Abundance

Lithium abundance is also used as an indicator of youth in stars, as all stars contain an initial amount of Li upon formation, which is depleted over time through reactions in the stellar core. The $^7Li(p,\alpha)$ reaction which is responsible for this depletion is highly temperature dependent and will only occur at temperatures of $> 2.5 \times 10^6$ K, adding a mass-dependence to the depletion process (see, e.g., Zuckerman & Song, 2004; Soderblom et al., 2014, for a review). Stars with $M_* < 0.35\mathrm{M}_\odot$ are fully-convective throughout the pre-Main Sequence (PMS) evolutionary stage, so lithium is depleted rapidly through the whole stars following the onset of the reaction. In higher mass stars a radiative core forms prior to the depletion onset, so that Li in the convective layer can remain for several Myr.

Baraffe & Chabrier (2010) suggest that early cold accretion of material onto the star may result in premature Li depletion, by temporarily raising the core temperature of the star. If so, this would reduce the utility of Li as an age indicator, as very young stars could be fully Li depleted. However, Sergison et al. (2013) found no evidence for such early depletion while looking at an independently selected sample of stars from two young associations. Later

modelling suggests that while possible, early Li depletion from cold accretion is very rare (Baraffe et al., 2017).

Due to the relationship between age, mass and Li abundance, Li measurements can serve as indicators of youth. However, the potential scatter and low rate of change of this relationship make it unreliable as a source of definite age estimates for individual stars, especially $M_* > 0.35\mathrm{M}_\odot$ stars, which have radiative cores.

1.2 Young Planets

Understanding young planets is critical for understanding their mature configurations. Fundamental planet properties like size, atmospheric composition, and orbital position all change within the first $\sim$ 1 Gyr of a planet's existence. To understand those changes we need to observe planets at various stages of undergoing them, which means young planets. Unfortunately only a few dozen planets $< 1Gyr$ have yet been discovered, although that number is rapidly growing (e.g., Bouma et al., 2022). By determining the ages of young associations with planets, or by finding planets in associations with known ages, we can place constraints on the mechanisms by which planets form and evolve. In this Section, I will discuss a few of the fundamental properties of planets thought to undergo significant changes, and the current observational constraints on them.

1.2.1 Planet Migration

Orbital period is a planet's most fundamental and easily observed property. The first discovery of an exoplanet around a MS star (Mayor & Queloz, 1995) revealed a planet unlike any in our solar system, with a mass half that of Jupiter but an orbital period of only 4.2 days. Since that first discovery of an exoplanet, astronomers have found numerous so-called "hot Jupiter" planets, those with $M \gtrsim 0.25 M_{Jup}$, and orbits with $P < 10d$. This led to a re-evaluation of planet-formation theories. Neither of the two primary planet-formation mechanisms, core-accretion (see Mordasini et al., 2008, for a review) and gravitational insta-

bility (see Durisen et al., 2007, for a review), are able to form such large planets at such close orbital periods (see Dawson & Johnson, 2018, for a review). So the existence of hot Jupiters suggests that they may have formed further out in the system and then migrated inwards. Two main migration mechanisms have been suggested, disk migration, and Kozai-Lidov high-eccentricity migration. One way to differentiate between these mechanisms is through the timescales on which they occur. Disk migration must occur before a protoplanetary disk dissipates, meaning that very young, < 10 Myr hot Jupiter planets should be possible, while tidal migration can occur over longer timescales. Determining precise ages for young associations which may host Hot Jupiter planets will help constrain these mechanisms.

1.2.2 Planet Size Evolution

Exoplanet discoveries have found an abundance of planets smaller than Neptune ~ 4 $R_{\oplus}$. The radius distribution of these planets is bimodal, with a gap between $1.5 < R < 2.0$ $R_{\oplus}$(Owen & Wu, 2017). This gap, known as the "sub-Neptune desert" may represent a transition between rocky "Earth-like" planets and icy Neptune-like planets. A proposed mechanism for the creation of the gap is photoevaporation, wherin the smaller planets which form in the gap lose their atmospheres under high-energy stellar radiation, but the somewhat larger sub-Neptunes do not. Other proposed mechanisms include core-powered mass loss (Gupta & Schlichting, 2019). Fully understanding the causes of this gap require a better understanding of how when it forms and how it changes over time (Berger et al., 2020).

Separate from the sub-Neptune desert, there is a second, more dramatic gap, found between the radii of Jupiter and Neptune (see Figure 1.3). However, numerous young planets have been found with radii in this gap, suggesting that young planets have inflated radii compared to their older counterparts (e.g., Rizzuto et al., 2017; Barragán et al., 2019; Benatti et al., 2019; Newton et al., 2019), which they may lose over time. Different mechanisms have been suggested to explain this size evolution (Owen, 2020). The timescales of these

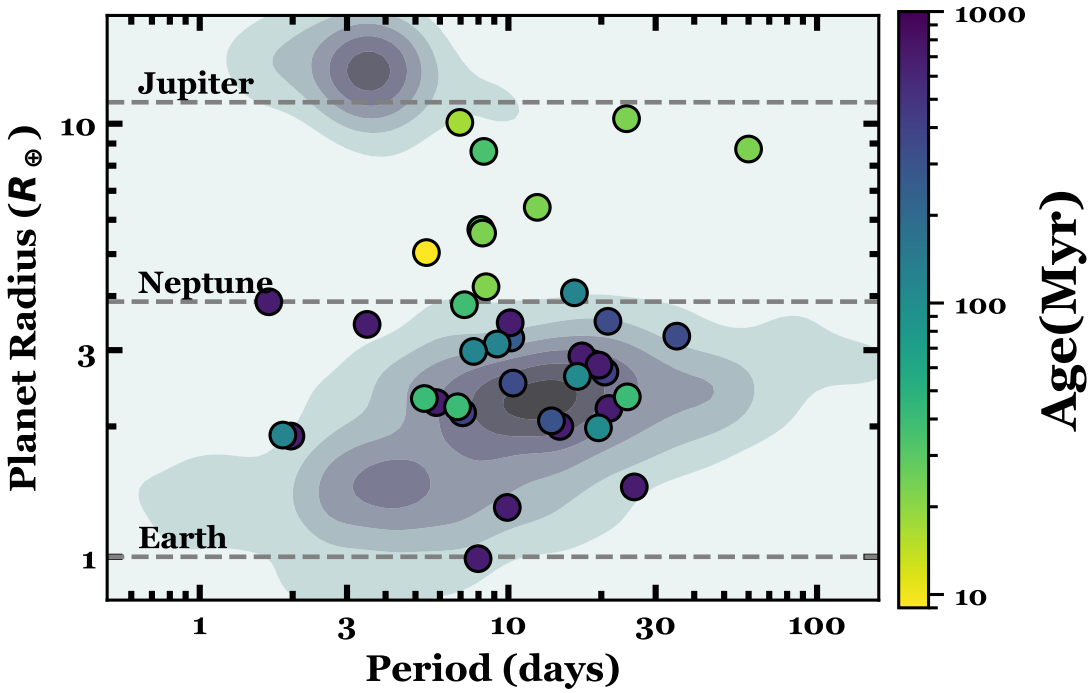

Figure 1.3 Radius-period distribution of known exoplanets. Planets with ages $< 700 Myr$ are shown as individual points, with the older population of stars shown as a density plot. Young planets are more likely to occur in the radius gap between Neptune- and Jupiter-sized planets, indicating that planets may form in that gap and then shrink. Reproduced from Wood et al. (2023) under CC 4.0 license.

mechanisms are different, so one way to distinguish between them is by mapping out how this gap changes in time.

1.3 Associations

Thanks to the difficulty of determining the ages of individual stars, stellar associations have been fundamental to our understanding of stellar formation and evolution.

The term "stellar association" is often used interchangeably with a variety of similar terms (e.g. stellar stream, moving group, open cluster, OB association) so it is worth a moment to define the differences between them and how I will use each of them in this dissertation. I use "association" as a general term for any group of stars which share a common formation time and location. An open cluster is a gravitationally bound association,

resulting in less dispersion. Open clusters (e.g. Hyades, Praesepe, Ruprecht 147) survive longer than other associations, as the gravitational forces between the stars resist the galactic tidal forces, and thus are often older. Due to their small dispersion many open clusters were discovered earlier than other types of association, and some, like the Pleiades, can even be seen with the naked eye.

OB Associations are another type of association which was discovered early when early 20th century astronomers determined that many of the most massive stars, of O and B stellar types, were grouped together. This is because these very massive stars are short lived compared to other stars, lasting only a few to tens of Myr, less than the dispersion time of a stellar nursery. Thus, the term OB Association is often applied to the youngest associations which still have numerous massive stars (e.g., Scorpius-Centaurus). Similarly, star-forming regions are the youngest associations, in which stars are actively being formed.

Stellar streams are defined by a high dispersion in one direction (along the galactic orbit) and a small transverse dispersion (e.g., Meingast et al., 2019; Ibata et al., 2018). While the same term has been used to describe remnants of stellar accretion into the galaxy (Helmi, 2020), here I use it only for groups of stars formed in-situ within the Milky Way which share a common age (e.g., Curtis et al., 2019).

A "moving group" is another general term, applying to groups of stars which are co-moving, and is largely redundant with "stellar association". In this dissertation I will only use the term moving group for associations which are traditionally named such (e.g., the β Pictoris Moving Group, BPMG) and will typically use the term "stellar association". Associations which do not fit into one of the discussed categories are typically more dispersed, as they are not gravitationally bound. The Galactic potential will typically fully disperse a group which is not gravitationally bound within a hundred Myr or so. This means that these associations are the best samples for studying young stars and planets between their formation and maturity.

1.3.1 Identifying Associations

Associations with different masses and ages are at different levels of dispersion, meaning that different techniques are needed to identify them and their members. Open clusters like the Hyades can be easily found by looking at stellar positions and proper motions, but unbound association are more difficult to locate. Projection effects and the high dispersion scatter association members across large portions of the sky and necessitate detailed kinematic information to identify them. To find associations correlated in all six dimensions of position and velocity, we need not only astrometric information like RA and Dec or on-sky proper motions, but also information about the distance and radial velocity (RV), requiring parallax and spectroscopic measurements. The recent *Gaia* mission has made this feasible across large portions of the sky with 6-parameter astrometry measurements for almost a billion stars (Gaia Collaboration et al., 2022). This massive expansion in available kinematic information has led to a corresponding explosion in the discovery and kinematic characterization of associations and association members (e.g., Kounkel et al., 2019; Meingast et al., 2019; Kerr et al., 2021).

1.3.1.1 BANYAN

Many techniques and tools to identify associations and association members using kinematic information have been developed, utilizing different information or algorithms (e.g., Malo et al., 2012; Kounkel et al., 2019; Kerr et al., 2021). The tool which I will be using the most in this dissertation is `BANYAN` Σ (Gagné et al., 2018), which I describe briefly in this section.

`BANYAN` Σ[1] is a bayesian probability tool for determining association membership of given stars. Using galactic coordinates $< X, Y, Z, U, V, W >$[2], `BANYAN` Σ defines an associ-

[1] `https://github.com/jgagneastro/banyan.sigma`

[2] In this coordinate system in which the sun is at $< 0, 0, 0 >$, X points towards the galactic center, Y is in the direction of galactic rotation, and Z is out of the galactic plane. U, V, and W are the velocities in the X, Y, and Z directions, respectively.

ation as a multivariate Gaussian distribution with some mean and dispersion. For a given star the likely galactic coordinates are calculated using a combination of position, proper motion, distance and velocity information, and compared to the distributions of nearby associations and the field, and a probability of membership in each is calculated. While the most accurate results are obtained when using full 6-D kinematic measurements, BANYAN Σ can also probabilistically estimate the position of a star in galactic coordinates without a provided distance or radial velocity. With a missing distance or RV measurement, the galactic position of the star will be optimized for each association hypothesis, producing a prediction of π or RV that produces the best match for each association. For each star in the input sample, BANYAN Σ will output a probability of membership in each association, a predicted RV and distance for each association, and list the best matching hypothesis (field or association) and best matching association.

BANYAN Σ is very useful because of its adaptability. It contains definitions for 27 associations within 150 pc based on lists of confirmed association members, but these definitions can be altered or new associations added as needed. Additionally, BANYAN Σ can be run on samples of as few or as many stars as necessary. Unlike clustering algorithms which need large, representative samples of stars to locate the associations within, BANYAN Σ can compare against the pre-defined associations and determine membership of one or a million stars.

These benefits make BANYAN Σ an excellent tool for determining the membership of nearby stellar associations, but it does have limitations. First, since it only compares stellar positions to the kinematics of known associations, it cannot be used to identify previously unknown groups. It also may miss extended populations of known groups, whose kinematics are outside the pre-defined Gaussian. BANYAN Σ only uses kinematic information to determine membership probability, so it may include kinematic interlopers within the membership of an association. Interlopers are stars from the field which coincidentally share the position and motion of the association. They can sometimes be identified as older by other stellar fea-

tures, such as activity or rotation, but these measures are far from certain (see Sections 1.1.1 and 1.1.2). They are more likely in older, more dispersed groups, making robust membership determination more difficult.

1.3.2 Association Ages

Associations are unmatched in their utility for studying stellar and planetary astrophysics because they provide a large sample of stars with an identical or nearly identical age across a range of spectral types. Any stellar dating method that can be applied to one or a group of the stars can be applied to the whole population, and the large sample size makes the resulting age more robust to scatter in age relations. The range of stellar masses also increases the accuracy of resulting ages by reducing ambiguity from regions with little age-dependence. For example, a single star with $G - G_{RP} \sim 0.5$ may be difficult to age using the isochrone method because there is little change in the expected magnitude at that color between $\sim$ 40 Myr and 2 Gyr. But using an association with a range of types reduces this ambiguity because higher-mass association members have much more change in the expected color with age.

In addition to producing more robust ages than individual stars, associations also allow us to calibrate additional age measurement techniques. With ages for all members, we can observe the relationship between age and properties such as spin-down (Curtis et al., 2013), chemical diffusion (Souto et al., 2018), binary evolution (Leiner et al., 2015), activity (Stelzer et al., 2013) and more (Torres et al., 2010; Stauffer, 2000), building and calibrating empirical relations which allow further age determinations.

In this Section I will describe four common methods for measuring the ages of associations.

1.3.2.1 Isochrone Fitting

The most commonly applied method for determining association age is fitting stellar evolutionary models to a CMD. This requires only measurements of color, magnitude, and distance, making it applicable to most of the sky thanks to surveys such as Gaia. But there are several drawbacks to this method. As discussed above, it produces different ages when applied to stars of different stellar types. Additionally, a high population of overluminous binary stars may lead the association to look younger than it is. So, while CMD fitting is a useful first step, calibration is needed to determine its accuracy and limits, and other methods are needed to supplement it.

1.3.2.2 Lithium Depletion Boundary

The most accurate and precise ages are derived using the LDB method (e.g., Soderblom, 2010). Stars contain an initial Li amount, which is unchanged until the core reaches 2.5×10^6 K, when it is rapidly depleted. In fully convective stars this leads to a clear relationship between mass, age, and surface Li abundance (see Figure 1.4). The relationship between stellar age, mass, and Li abundance in fully convective stars is well-understood, so resulting ages vary by $< 10\%$ regardless of model Burke et al. (2004); Tognelli et al. (2015). However it can only be applied to associations between 15 and 200 Myr, below which all M dwarfs have Li and above which none do, and is observationally expensive. Additionally, the effects of factors such as accretion, metallicity, and activity have not yet been fully explored (Baraffe & Chabrier, 2010; Jackson & Jeffries, 2014; Sergison et al., 2013).

1.3.2.3 Li Sequence

One can also estimate an association's age by examining the full sequence of Li abundance as a function of color (Soderblom et al., 2014). This method uses Li abundance, rather than the threshold used by the LDB, and requires conversion between modeled abundance, A(Li), and measured equivalent width, EW(Li), so it is more model-dependent than LDB. It can,

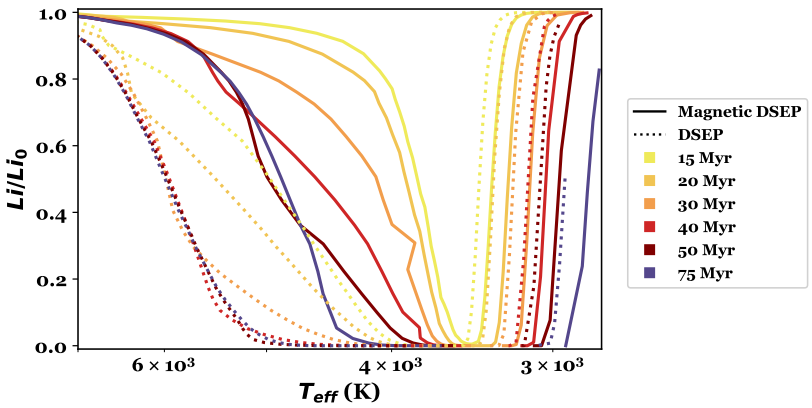

Figure 1.4 Stellar evolutionary models of Li abundance as a function of $T_{\rm eff}$. Models with magnetic field treatment (solid lines, Feiden, 2016) and standard ones (dotted lines, Dotter et al., 2008) are shown. The sharp cutoff of abundance for stellar types later than M3 comprises the LDB and is relatively model-independent. The more gradual Li sequence in higher mass stars has significantly greater model dependence.

however, serve as an additional check on the association age, or an alternative method for associations which are too young or old for LDB.

1.3.2.4 Gyrochronology

Gyrochronology uses empirical relationships between stellar rotation, mass, and age to estimate association age. The color-period relationship is a function of age, allowing the rotation speed to serve as a stellar clock. This is particularly useful for planet detections since transit lightcurves intrinsically contain information about stellar rotation. TESS provides nearly full-sky photometric coverage for stars with $T < 14$, making gyrochronology widely applicable. However, gyrochronological relations are only well-defined between 100 Myr and 1 Gyr, as younger groups are still spinning up, and the spin down of older groups stalls (Curtis et al., 2013), and there are still unknown factors (see e.g., Bouvier et al., 2018).

1.3.3 Association Structure

In the last decades, detailed surveys of nearby associations have shown a much more complicated picture of the properties, structure, and formation history of stellar associa-

tions than previously known. The advent of the high-precision position, velocity, and color measurements of *Gaia* (Gaia Collaboration et al., 2016) combined with new techniques for locating associations (e.g., HDBSCAN; McInnes & Healy, 2017) have significantly altered our view of young associations near the Sun. One discovery has been the level of sub-grouping within well-known associations. For example, Wright & Mamajek (2018) and Krolikowski et al. (2021) found that the distribution of stellar ages and kinematics within large associations is likely the result of many localized star-formation events occurring over periods of $5 - -10$ Myr as opposed to the collapse of a single molecular cloud. Some studies have revealed entirely new young populations (Oh et al., 2017; Kounkel et al., 2019), including some that are far more diffuse than those previously known (Meingast et al., 2019). Other studies have found that groups thought to be distinct may be fragments of a single star-formation event (Gagné et al., 2021). This simultaneous fragmenting and merging of known groups, combined with the discovery of new young stellar associations has created a complex picture of young associations and has direct implications on our understanding of the origin of nearby stellar associations (e.g., Zucker et al., 2022b).

We don't know if complexes form from single molecular clouds which break up after the stars are formed, or if they form from neighboring clouds which collapse around the same time. Nearly simultaneous collapse of adjacent clouds could be caused by supernovae within one group triggering collapse in its neighbors — as has been proposed as the cause of all recent star formation near the sun (Zucker et al., 2022b), or by the clouds moving through a Galactic spiral arm (Fernández et al., 2008). Or, the complexes could be the dispersed progeny of a single cloud collapse, resulting from Galactic forces tearing off clumps of an originally tightly-bound group (Gagné et al., 2021). Each of these scenarios should create different arrangements of star formation. Supernova-triggered collapses could produce a pattern with the oldest groups at the center of the complex, and the youngest at the edges. We would expect to see gaps of only a few million years between each generation of star formation, as this is the timescale for the most massive supernovae. In contrast, if the

collapses were triggered by an outside event, we would expect to see no clear ripple-effect pattern, but still see very similar ages. If the ages of the associations are different by more than a few million years, it could indicate some other formation mechanism.

1.4 Specific Associations

1.4.1 Scorpius-Centaurus

The Scorpius-Centaurus Association (Sco-Cen) is the nearest OB association to the Sun, harboring $\simeq$150 B-type stars and tens of thousands of lower-mass members (de Zeeuw et al., 1999). The association is classically divided into three populations; Upper Scorpius (US), Upper Centaurus Lupus (UCL), and Lower Centaurus Crux (LCC), with ages varying from 11 to 17 Myr (Pecaut et al., 2012). The Sco-Cen complex (sometimes called Greater Sco-Cen) includes many other molecular clouds and star-forming groups (e.g., Ophiuchus and Lupus), but none of the main three groups show evidence of ongoing star formation (Preibisch & Mamajek, 2008). This combination of factors makes Sco-Cen an exceptional laboratory to test models of early stellar evolution, and has motivated more than a century of intense research (e.g., Kapteyn, 1914; Pecaut et al., 2012; Feiden, 2016; Wright & Mamajek, 2018).

However, there is still much to be understood about the structure and formation of Sco-Cen, particularly with the arrival of astrometry from *Gaia* (Gaia Collaboration et al., 2016). Pecaut & Mamajek (2016) found a strong age gradient across Sco-Cen in general and LCC in particular, noting that the southern region of LCC is younger than the northern. Goldman et al. (2018) found a separate moving group within the southern portion of LCC, dividing it into multiple sub-populations with ages ranging from 7 to 10 Myr. This result was confirmed by Kerr et al. (2021), who recovered those four groups and included the younger ϵ Chamaeleontis (ϵ Cha) as a fifth. These discoveries paint a more complicated picture of Sco-Cen than the classical three single-aged populations, and raise the possibility that the census of the Sco-Cen region is still incomplete.

Mapping out Sco-Cen is particularly important because of its outsized role in the study of young planets. It is nearby and young enough for direct imaging of young planets on wide orbits (e.g., Hinkley et al., 2015; Bohn et al., 2020b). The association is also diffuse enough to separate out individual stars even with large $K2$ and *TESS* pixels, enabling the discovery of young transiting planets. The youngest known transiting planet, (K2-33 b; David et al., 2016; Mann et al., 2016a) the youngest transiting hot Jupiter, (HIP 67522 b; Rizzuto et al., 2020), and the largest planet known to orbit a mid-M dwarf (TOI 1227 b; Mann et al., 2022) are all in Sco-Cen. Such systems are critical to our understanding of the early evolution of planetary systems, but the sample is still small. New sub-structures in Sco-Cen would provide new regions to search for such planets, potentially with a wider range of (young) ages.

1.4.2 Carina-Columba

The Carina–Columba region is an understudied 40-Myr old complex in the southern sky. It was first discovered in the early 2000s, and named the GAYA complex, composed of three separate associations: Carina, Columba, and Tucana-Horologium (Torres et al., 2008). These associations are close in space and have similar velocities, and all three have estimated ages of around 40 Myr. However, recent research suggests that Tucana-Horologium is not related to the other two, which, with other nearby groups, form their own complex (Gagné et al., 2021). Other nearby associations include Theia 92, 113 and 208, which were discovered using Gaia DR2 and machine-learning clustering algorithms (Kounkel & Covey, 2019), and could be a bridge between the Carina and Columba associations and the Platais 8 association (Gagné et al., 2021). I propose to test the relationship between these associations and current hypotheses on formation mechanisms by measuring the ages of each association within the Carina complex to map out the history of the region.

CHAPTER 2: MUSCA AND LOWER CENTAURUS CRUX

As part of the *TESS* Hunt for Young and Maturing Exoplanets collaboration (THYME; Newton et al., 2019), our team searches *TESS* data using a specialized pipeline to identify young planets missed by standard searches (e.g., Rizzuto et al., 2020), and checks previously identified planet candidates for signs of membership in a young association (e.g., Mann et al., 2020; Newton et al., 2021) [1]. We identified TOI-1227 (2MASS J12270432-7227064, TIC 360156606) as a member of a young association, with a planet candidate (TOI1227.01) identified by the *TESS* mission, and astrometry consistent with membership in the Lower Centaurus Crux (LCC) region of the Scorpius-Centaurus (Sco-Cen) OB association (Goldman et al., 2018; Damiani et al., 2019). The *TESS*-identified transit signal is $\simeq$2% deep, suggesting a Jovian-sized planet orbiting a pre-main-sequence low-mass star. As giant planets with periods <100 days are rare around older stars of similar mass (< 1% Bonfils et al., 2013), validation of this planet would provide strong evidence of radius evolution.

The LCC region which contains TOI-1227 is one of the three major components of the Scorpius-Centaurus association. Additional substructure within LCC was discovered by Goldman et al. (2018) and Kerr et al. (2021), who each divided LCC into 4 or 5 subpopulations (Kerr et al. (2021) included ϵ Cha as a 5th subpopulation of LCC). Each of these subpopulations has a distinct age and kinematics, which vary slightly from the others.

In this chapter, we present validation, characterization, and age estimates for TOI-1227 b, a $0.85 R_{Jup}$ planet orbiting a $\simeq$11 Myr pre-main-sequence M5V star ($0.17 M_{\odot}$) every 27.26 days. In Section 2.1, we detail the photometric and spectroscopic follow-up of the

[1]Sections 1-3 of this chapter are adapted from the paper *"TESS Hunt for Young and Maturing Exoplanets (THYME). VI. An 11 Myr Giant Planet Transiting a Very-low-mass Star in Lower Centaurus Crux"* by A. Mann, M. Wood et al. AJ 163, 4 (2022), reproduced under the CC 4.0 license with author permission.

planet and host star. We derive an updated age of 11 ± 2 Myr for the parent population, Musca, in Section 2.2. We use our ground-based follow-up to statistically validate the planet in Section 2.3. We kinematically define each of the subpopulations of LCC in Section 2.4, and determine the ages of the other subpopulations in Section 2.5.

2.1 Observations

2.1.1 *TESS* Photometry

TOI-1227 was observed by the *TESS* mission (Ricker et al., 2015) from UT 22 Apr 2019 through 19 Jun 2019 (Sectors 11 and 12) and then again from 2021 Apr 28 through 2021 May 26 (Sector 38). In all three sectors, the target fell on Camera 3. The first two sectors had 2 min cadence data as part of a search for planets around M dwarfs (G011180; PI Dressing). Sector 38 had 20 s cadence data, as it was known to be a young TOI at that phase (G03141; PI Newton). We initially used the data with a 2 min cadence for all analysis for computational efficiency and *TESS* cosmic-ray mitigation[2] (not included in 20 s data), but also ran a separate analysis using the Sector 38 20 s data. In both cases, we used the Pre-Search Data Conditioning Simple Aperture Photometry (PDCSAP; Stumpe et al., 2012; Smith et al., 2012; Stumpe et al., 2014) *TESS* light curve produced by the Science Process Operations Center (SPOC; Jenkins et al., 2016) and available through the Mikulski Archive for Space Telescopes (MAST)[3].

2.1.2 Identification of the transit signal

The planet signal, TOI1227.01, was first detected in a joint transit search of sectors 11 and 12 (one transit in each) with an adaptive wavelet-based detector (Jenkins, 2002a; Jenkins et al., 2010). The candidate was fitted with a limb-darkened light curve (Li et al.,

[2]https://archive.stsci.edu/files/live/sites/mast/files/home/missions-and-data/active-missions/tess/_documents/TESS_Instrument_Handbook_v0.1.pdf

[3]https://mast.stsci.edu/portal/Mashup/Clients/Mast/Portal.html

2019) and passed all diagnostic tests (Twicken et al., 2018). Although the difference image centroiding failed to converge, the difference images indicate that the transit source location was consistent with the location of the host star, TOI-1227. A search of the residual light curve failed to identify additional transiting planet signatures. The TESS Science Office reviewed the diagnostic test results and issued an alert for this planet candidate as a TESS object of interest (TOI) on 2019 August 26 (Guerrero et al., 2021). A third transit was detected in the Sector 38 *TESS* data, consistent with the expected period and depth.

We searched for additional planets using the Notch and LoCoR pipelines, as described by Rizzuto et al. (2017) [4]. This included using the significance of adding a trapezoidal Notch to the light curve detrending, as characterized by the Bayesian information criterion (BIC). The method was more effective than periodic methods for finding planets with $\lesssim$3 transits, as was the case for HIP 67522 b (Rizzuto et al., 2020). The transits were quite clear from the BIC test. However, no additional significant signals were detected.

TOI-1227 is a relatively faint star ($T = 13.8$) in a crowded region (see Figure 2.1). Within 2′ ($\simeq$6 *TESS* pixels), there are four sources brighter than TOI-1227, one of which is $T = 8.4$ (TIC 360156594). Two sources brighter than TOI-1227 are within 1′. While the *TESS* aperture was small (4–6 pixels over the 3 sectors), background contamination was likely to be a problem for the *TESS* data. Correcting for contamination and confirming the planet were the major motivations for our ground-based follow-up.

2.1.3 Ground-Based Photometry

Table 2.1 summarizes the photometric observations. We provide details by instrument below.

We observed two transits of TOI-1227 b using the SOAR 4.1 m telescope at Cerro Pachón, Chile, with the Goodman High Throughput Spectrograph in imaging mode (Clemens et al., 2004). For both observations, we used the red camera. In this mode, Goodman has a default

[4] `https://github.com/arizzuto/Notch_and_LOCoR`

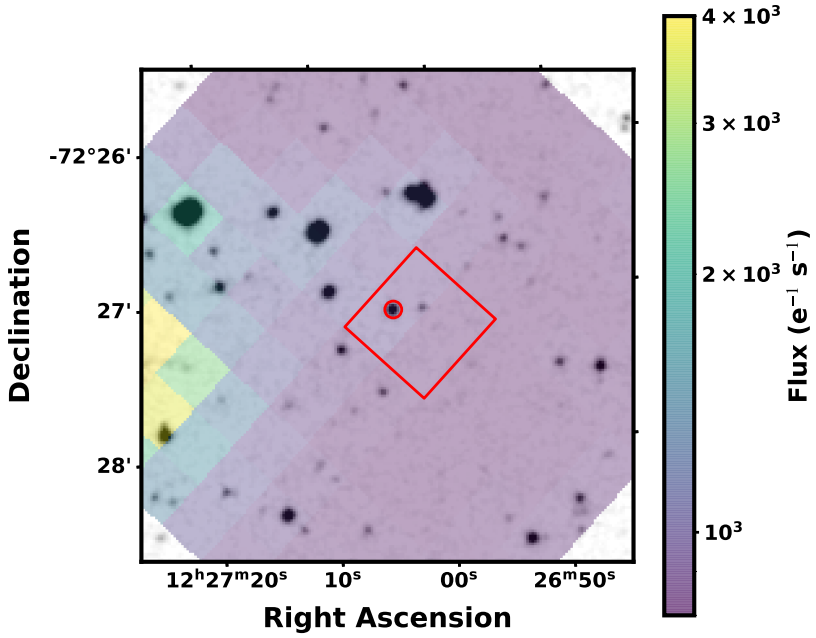

Figure 2.1 *TESS* Sector 11 image (colorbar) of TOI-1227 overplotted on a Digital Sky Survey (DSS) image (grayscale). The red circle indicates TOI-1227 and the red box indicates the *TESS* aperture used for Sector 11 (the aperture varied between sectors). The *TESS* PSF in this region has a full-width half-max of approximately 1.9 *TESS* pixels. The large *TESS* PSF combined with a faint source meant that there were high levels of contamination around TOI-1227.

7.2′ diameter circular field of view with a pixel scale of 0.15″/pixel. The first transit was observed on 2020 Jan 15 with the SDSS i' filter, and the second transit was observed on 2021 Mar 28 with the SDSS g' filter. Both nights had photometric conditions for the full duration of the transit observations. Although TOI-1227 is much fainter in g' than in i', we used a 120 s exposure time for both filters to resolve any flares and sample the ingress. We selected a smaller region-of-interest in the readout direction (1598 pixels) to decrease readout time to 1.7 s. Due to the small pixel scale, no defocusing was required and counts were well below half-well depth for both the target and all but one target in the field of view (HD 108342).

About 1 hour into the 2021 Mar 28 transit observations, the SOAR guider began to fail, causing the target to shift $\simeq$5 pixels per exposure and forcing us to shift it back manually every $\sim$10 exposures. During egress, the guider completely failed and had to be reset before re-acquiring the field. We positioned the target back to its starting location and continued

Table 2.1 Log of transit observations.

Start	Telescope	Filter	Transit #	T_{exp} (s)	Obs Duration (h)
2019 Apr 22[a,b]	*TESS* S11	*TESS*	1	120	N/A
2019 Apr 22[a,b]	*TESS* S12	*TESS*	2	120	N/A
2020 Jan 15[b]	SOAR	i'	9	120	8.1
2020 Jan 15	LCO	i'	9	200	2.8
2020 May 03[b]	LCO	i'	13	200	1.9
2020 Jul 24	LCO	r'	16	200	2.5
2020 Jul 24[b]	LCO	z_s	16	200	2.5
2021 Mar 28[b]	SOAR	g'	25	120	7.6
2021 Apr 24	ASTEP	Rc'	26	200	5.7
2021 Apr 24	LCO	g'	26	300	6.2
2021 Apr 24[b]	LCO	z_s	26	210	6.2
2021 Apr 28[a,b]	*TESS* S38	*TESS*	27	20	N/A
2021 Jun 17[b]	LCO	g'	28	300	4.1

[a] *TESS* observed TOI-1227 for one transit in each of Sectors 11, 12, and 38.
[b] Included in the global fit.

the observations as normal. This resulted in poorer photometric precision than normally achievable with Goodman/SOAR, and a $\simeq$15 min gap in the data near the end of the egress.

We applied bias and flat-field corrections before extracting photometry for TOI-1227 using a 10-pixel radius aperture and used an annulus of 30–60 pixels to determine the local sky background. The aperture center for each exposure was the stellar centroid, calculated within a 10-pixel radius of the nominal location. We repeated this on eight nearby stars that were close in brightness to the target and showed little or no photometric variation when compared to other stars in the field. We corrected the target light curve using the weighted mean of the comparison-star curves.

2.1.4 Goodman/SOAR Spectroscopy

We took additional spectroscopic observations of TOI-1227 with the Goodman spectrograph (see above) on two nights. We used the red camera, the 1200 l/mm grating in the

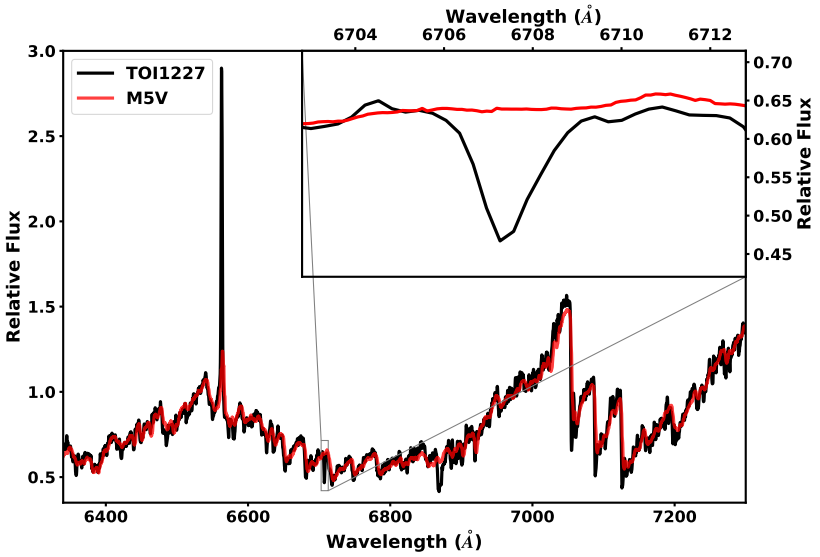

Figure 2.2 Goodman spectrum of TOI-1227 (black) and a template M5V dwarf from Kesseli et al. (2017). Because of extinction around TOI-1227 and imperfect flux calibration from Goodman, we fit and divide by a 2nd-order polynomial on the Goodman spectrum to better match the template. The Goodman spectrum is also higher resolution than the template (R of 5880 vs 2000). The inset highlights the Li 6708Å line, which is absent in the spectrum of older stars like the template, but strong in TOI-1227's spectrum.

M5 setup, and the 0.46″ slit rotated to the parallactic angle. This setup gave a resolution of $R \simeq 5880$ spanning 6150–7500Å.

We obtained the first spectrum on 2019 Dec 12 (UT) shortly after the target was alerted as a TOI, to check for signs of youth. We obtained three back-to-back exposures of TOI-1227, each with an exposure time of 800 s. The resulting spectrum showed the Li and Hα expected for a young star and TiO features consistent with an M5 dwarf, as we show in Figure 2.2. Once we confirmed the planetary signal (based on ground-based transits), we obtained an additional spectrum on 2021 Feb 23 (UT) under clear conditions. Our goal was a spectrum with a signal-to-noise ratio (SNR) $>$ 100 per pixel across the full wavelength range, to use for stellar characterization. To this end, we used an exposure time of 1800 s for five back-to-back exposures.

To better determine the age of TOI-1227, we also observed 13 nearby stars that are likely part of the same grouping in LCC as TOI-1227 (see Section 2.2). The 13 targets observed

with Goodman were selected from the parent sample to map out lithium levels from M0 to M5, which can constrain the age of the population. These targets were observed between 2021 Feb 23 and 2021 Apr 24 using an identical setup to the observations for TOI-1227. Exposure times were set to ensure a SNR greater than 50 (per pixel) around the Li line and varied from 90 s to 420 s per exposure with at least 5 exposures per star for outlier (cosmic ray) removal.

Using custom scripts, we performed bias subtraction, flat fielding, optimal extraction of the spectra (Horne, 1986), and mapping pixels to wavelengths using a 5th-order polynomial derived from the Ne lamp spectra obtained right before or after each spectrum. Where possible, we applied a small linear correction to the wavelength solution based on the sky emission or absorption lines. We stacked the individual extracted spectra using the robust weighted mean. For flux calibration, we used an archival correction based on spectrophotometric standards taken over a period of a year. Due to variations on nightly or hourly scales, this correction is only good to $\simeq$10%.

2.2 The Age of Musca

2.2.1 Age from Li measurements

Lithium (Li) is a powerful indicator of age in young stars (Chabrier et al., 1996). M dwarfs deplete their lithium over 10–200 Myr at a rate that depends on their spectral type; this forms a region where stars have no surface lithium (i.e., the lithium depletion boundary or LDB). The location and size of the LDB are strongly sensitive to the association's age, and LDB ages are largely independent of the isochronal age (Soderblom et al., 2014). At the youngest ages (<20 Myr), lithium is only partially depleted, leading to a "dip" in the Li levels short of a full boundary (Figure 2.3; also see Rizzuto et al., 2015). The location and depth of the lithium dip also depend strongly on age.

For our Li determinations, we measured the equivalent width of the Li 6708 Å absorption line for 22 stars using our high-resolution ESO archival (11 targets) and Goodman (13

targets) spectra (two stars overlap). To account for the variations in resolution, $v \sin i_*$, and velocity between targets and the instrument used, we first fit nearby atomic lines with a Gaussian profile (e.g., iron lines for warmer stars and potassium lines for the M dwarfs). We used the width from these fits to define the bounds of the Li line. To estimate the pseudo-continuum, we iteratively fit the 6990–6720 Å region excluding the Li line, each time removing regions $>4\sigma$ below the fit (there were no emission lines in this region). We did not attempt to correct for contamination from the Fe line at 6707.44 Å or broad molecular contamination in the cooler stars, which likely set a limit on the precision of our equivalent widths at the $\simeq$10% level.

A single star, TIC 359357695, had two clear sets of nearly equal-depth lines. Interestingly, this star is a known TOI (1880), indicating a roughly equal-mass eclipsing binary. For the Li equivalent width, we measured each line individually with a manually applied offset. We then combined the two equivalent widths.

In Figure 2.3b we compare the Li sequence for Musca to that from β Pic ($\simeq$24 Myr; Shkolnik et al., 2017) and ϵ Cha (3-5 Myr; Murphy et al., 2013). The ϵ Cha cluster has high Li levels over the full sequence, while β Pic showed a full depletion around M3–M5. Musca resides between these two, with a dip in Li levels around M3 but not full depletion; this effectively bounds the age of Musca between the two groups. Based on Li predictions from the Dartmouth Stellar Evolution Program (DSEP; Dotter et al., 2008) with magnetic enhancement (Feiden & Chaboyer, 2013), we estimate the Li age to be 8–14 Myr (Figure 2.3).

2.2.2 Comparison to theoretical isochrones

We compare the candidate members of Musca to the PARSECv1.2S stellar isochrones (Bressan et al., 2012), and the magnetically enhanced DSEP models (Feiden, 2016). To handle contamination from binaries and nonmember interlopers, we used a mixture model described in detail in Mann et al. (2022). We also removed stars with RUWE$>$ 1.3 (likely binaries) and stars outside the parameters included in the isochrones (i.e., stars with $M_G >$

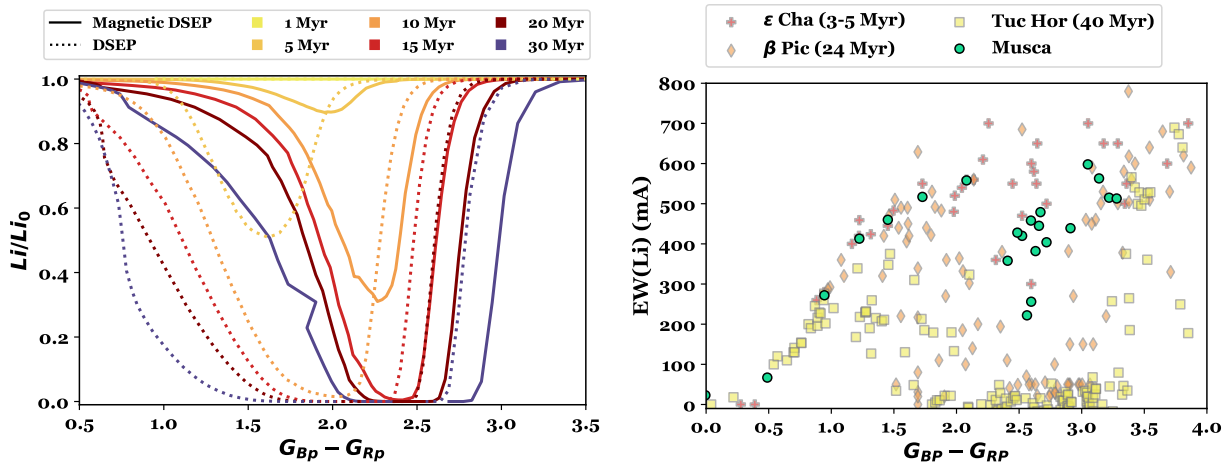

Figure 2.3 The Li sequence of Musca compared to models and benchmark associations. Left: Li abundance relative to the initial level predicted by the DSEP magnetic models for two different Solar abundance scales (dashed and solid lines) with colors corresponding to different times. The existence of a significant drop in the Li levels without a full depletion limits an association's age to 8–14 Myr, depending on the assumed abundance scale (Grevesse & Sauval, 1998; Asplund et al., 2009). Right: lithium equivalent width of TOI-1227 (red) and its kinematic neighbors measured from Goodman or high-resolution ESO archival spectra. We compare this to the sequence from ϵ Cha (red; Murphy et al., 2013), β,Pic (orange; Shkolnik et al., 2017) and Tuc-Hor (yellow da Silva et al., 2009) and (Kraus et al., 2014). Arrows indicate upper limits. ϵ Cha shows a clear sequence, while β Pic shows full Li depletion around M2–M4. The stars associated with TOI-1227 show a dip around M3, but not a full depletion, bracketing the age between the two groups (5 Myr and 24 Myr).

11.8 and $G - R_P > 1.45$). Many tight pairs were resolved in *Gaia*, but not in 2MASS or similar ground-based surveys. The mixture model is not set up to handle these cases; a data point has a single outlier probability independent of the band. Thus, we performed this comparison using *Gaia* magnitudes only. An inspection of the sequence using 2MASS magnitudes suggested that this would not change the derived age in any significant way.

The fit using the PARSECv1.2S models, shown in Figure 2.4, yielded an age of 11.6 ± 0.5 Myr, consistent with 11.8 Myr from Goldman et al. (2018), 13.0 ± 1.4 Myr from Kerr et al. (2021), and $\simeq$ 12 Myr for the lower end of LCC from Pecaut & Mamajek (2016). The age errors were likely underestimated, as our fit did not fully account for model systematics (often $\simeq$1–3 Myr, e.g., Bell et al., 2015). Indeed, the fit slightly under-predicted the luminosity of K2–K5 dwarfs and overpredicted the value for M4 and later. The fit to magnetic DSEP

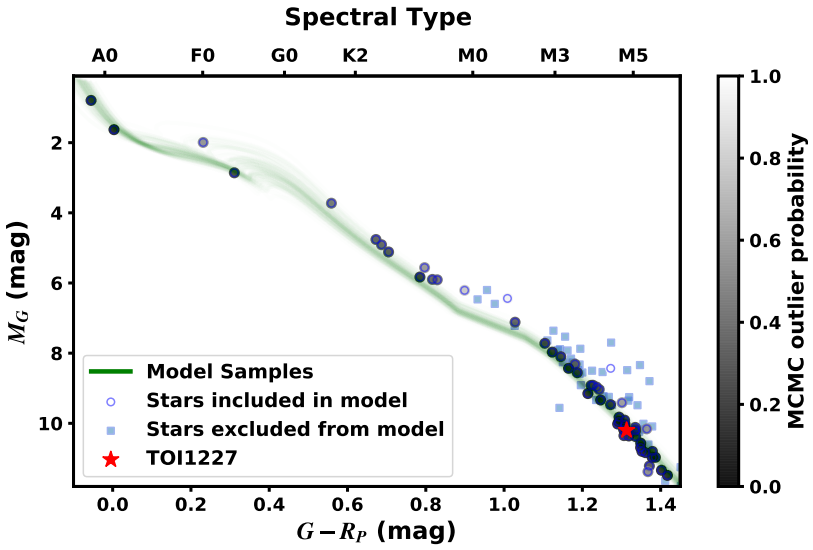

Figure 2.4 Comparison of Musca members (circles) with PARSECv1.2 stellar evolutionary models. The model comparison is done using color, but approximate spectral classes are given on the top axis. Stars included in the fit (blue circles) are filled based on their outlier probability. Excluded points (mostly due to a high RUWE) are shown as blue squares. The green lines are 200 random samples from the MCMC posterior. Models predict slightly different ages at different mass ranges; the mixture model takes the majority age by down-weighting stars in poorly matched regions (increasing their outlier probability).

models yielded a consistent age of 11.1±1.4 Myr, suggesting model differences are comparable to our measurement errors.

We repeat this process for the other LCC groups, described in Section 2.5, with results shown in Table 2.2.

2.3 Confirmation of TOI-1227 b

We considered three potential false positive scenarios to explain the transit signal: an eclipsing binary, a background eclipsing binary, and a hierarchical (bound) eclipsing binary — i.e. an secondary pair of eclipsing stars which is bound to the host star. Other scenarios which could apply specifically to young stars (e.g., stellar variability) were quickly dismissed due to the depth, duration, and shape of the transit, as well as its consistency over more than a year.

To check for an eclipsing binary, we use the MOLUSC code (Wood et al., 2021). MOLUSC simulated binary companions following an empirically-motivated random distribution in binary parameters. We limit the mass of the synthetic companions to between $10\,M_J$ to $0.17\,M_\odot$, as the goal was only to identify any unseen stellar or brown dwarf companion. For each synthetic binary, MOLUSC computed the corresponding velocity curve, brightness, and sky-projected separation, as well as enhancement to the noise that would be measured by *Gaia*. The results were compared directly to our observed high-resolution images, radial velocities, and the *Gaia* astrometry. When running MOLUSC, we included all radial velocity data, high-resolution imaging, *Gaia* astrometry, and limits implied by TOI-1227's CMD position compared to the population (the latter effectively rules out companions $<$0.3 mag fainter than TOI-1227 at the bandpass and resolution of *Gaia*). In total, MOLUSC generated 5 million synthetic companions and determined which could not be ruled out by the data (i.e. the survivors).

MOLUSC found that only 9% of the generated companions survived (Figure 2.5). Most of the survivors were faint or stars on wider orbits that happen to have orbital parameters that put them behind or in front of TOI-1227 during all observations. Furthermore, when we restricted the survivors to those that could reproduce the observed transit (unresolved in imaging and sufficiently bright for the observed transit), only 1% of the possible companions remained.

Additional false-positive checks are described by Mann et al. (2022).

2.4 Kinematic Definitions of LCC Sub-Populations

The LCC substructures found by Goldman et al. (2018) and Kerr et al. (2021) were only discovered after the publication of BANYAN Σ, and so are not included in the kinematic definition of LCC used therein.[5] LCC is instead treated as a single population and modeled

[5]This section is adapted from an appendix to the paper *"TESS Hunt for Young and Maturing Planets (THYME). IX. A 27 Myr Extended Population of Lower Centaurus Crux with a Transiting*

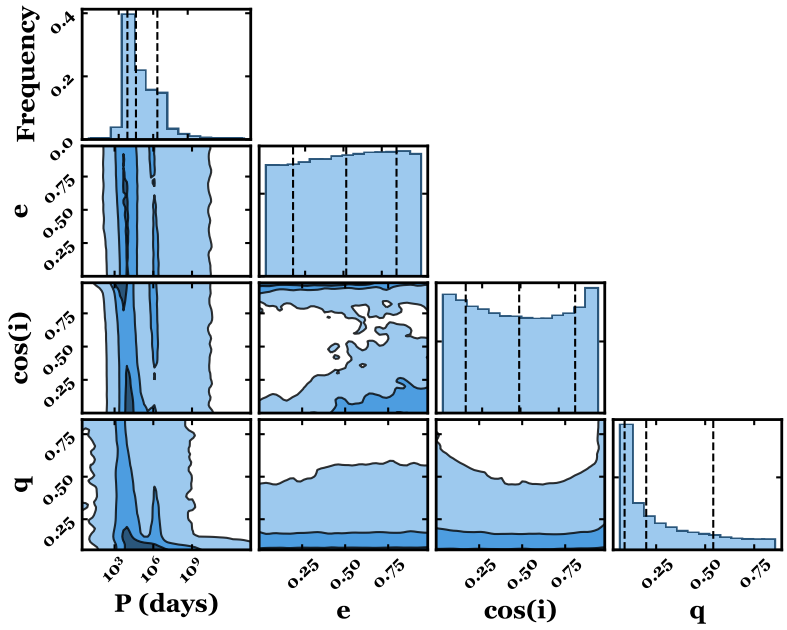

Figure 2.5 Distribution of surviving companions from `MOLUSC` in period (P), eccentricity (e), cosine of the inclination ($\cos(i)$) and mass ratio (q). The distribution represents only 9% of the total generated companions, the rest of which were ruled out by the observational data.

as using a single multivariate Gaussian. In order to determine the membership of each subpopulation and the relative probability of membership between groups, we add definitions of each to the list of `BANYAN` Σ groups.

The LCC sub-populations were independently found by Goldman et al. (2018) and Kerr et al. (2021), who used different naming schemes for the groups. We use the names from Goldman et al. (2018), and note that the groups A0 (referred to here as Musca), A, B, and C correspond to B, C, E and D from Kerr et al. (2021) (see Table 2.2 for summary). Kerr et al. (2021)'s group LCC A has no counterpart in the paper by Goldman et al., but is more commonly known as ϵ Cha, and was already in `BANYAN` Σ.

First we define the membership of the LCC sub-populations by combining the membership lists from Goldman et al. (2018) and Kerr et al. (2021). We obtain the candidate members of groups A0, A, B, and C from Goldman et al. (2018, Table 2), and use the

Two-Planet System" by M. Wood et al. (2023), reproduced under the CC 4.0 license with author permission. I led and wrote the paper.

Table 2.2 Parameters of LCC Sub-populations.

Goldman Name	Kerr Name	N_{Total}	X (pc)	Y (pc)	Z (pc)	U (km s^{-1})	V (km s^{-1})	W (km s^{-1})	Age (Myr)
A0	B	79	52	-87	-15	-8.48	-21.69	-8.88	11.1±1.4
A	C	211	53	-91	-3	-9.80	-19.71	-7.79	12.0±1.8
B	E	474	53	-94	11	-8.92	-20.30	-6.88	14.9±1.6
C	D	494	61	-96	22	-8.55	-20.36	-6.14	16.6±1.1

provided *Gaia* DR2 coordinates to crossmatch the sources with *Gaia* DR3, searching a 1 arcminute area around each star and taking the closest source as a match. The Kerr et al. (2021) candidate members are obtained from Table 3 of Kerr et al. (2021), and the provided *Gaia* DR2 coordinates used to crossmatch the sources with *Gaia* eDR3, using the same radius as for the Goldman et al. (2018) match. We then combine the membership lists for the two, using their *Gaia* DR3 source IDs.

For sub-populations A0, A, and B the majority of the candidate members were recovered by both surveys, and the selections of each are similar, with a common core, and some variation on the outskirts. However, few of the sub-population C candidates were recovered by Kerr et al. (2021), so that the Goldman et al. (2018) membership list contains the vast majority of the members and has a significantly larger extent than the Kerr et al. (2021) membership.

To calculate the center vector and covariance matrix of each sub-population we use the combined membership lists, cut to only those stars with *Gaia* DR3 RV measurements. The covariance matrices of all four populations are shown below, and the values of the center vector listed in Table 2.2.

Musca (LCC-A0)

$$\bar{\bar{\Sigma}}_{A0} = \begin{bmatrix} 6.774 & -3.706 & 12.025 & 1.906 & -2.431 & 1.222 \\ -3.706 & 13.499 & -1.037 & 5.263 & -7.798 & -1.359 \\ 12.025 & -1.037 & 27.141 & 9.426 & -13.696 & 1.53 \\ 1.906 & 5.263 & 9.426 & 19.13 & -30.034 & -3.405 \\ -2.431 & -7.798 & -13.696 & -30.034 & 47.339 & 5.521 \\ 1.222 & -1.359 & 1.53 & -3.405 & 5.521 & 1.094 \end{bmatrix}.$$

LCC-A

$$\bar{\bar{\Sigma}}_{A} = \begin{bmatrix} 5.364 & -0.873 & -0.807 & 0.165 & 0.614 & 0.16 \\ -0.873 & 17.4 & -4.569 & 1.271 & -0.026 & -0.283 \\ -0.807 & -4.569 & 9.034 & 0.815 & -1.742 & 0.378 \\ 0.165 & 1.271 & 0.815 & 5.792 & -9.457 & -0.28 \\ 0.614 & -0.026 & -1.742 & -9.457 & 16.059 & 0.449 \\ 0.16 & -0.283 & 0.378 & -0.28 & 0.449 & 0.149 \end{bmatrix}.$$

LCC-B

$$\bar{\bar{\Sigma}}_{B} = \begin{bmatrix} 54.486 & 3.078 & -4.913 & 1.8 & 3.413 & -0.675 \\ 3.078 & 16.729 & -4.972 & 0.169 & 1.887 & -0.477 \\ -4.913 & -4.972 & 28.202 & 0.205 & -1.079 & 2.185 \\ 1.8 & 0.169 & 0.205 & 2.052 & -3.02 & 0.348 \\ 3.413 & 1.887 & -1.079 & -3.02 & 6.021 & -0.673 \\ -0.675 & -0.477 & 2.185 & 0.348 & -0.673 & 0.392 \end{bmatrix}.$$

LCC-C

$$\bar{\bar{\Sigma}}_C = \begin{bmatrix} 114.137 & 4.809 & 5.911 & 7.288 & 0.418 & 0.815 \\ 4.809 & 44.83 & -7.989 & 1.304 & 3.228 & -1.043 \\ 5.911 & -7.989 & 16.065 & 0.677 & -0.809 & 0.81 \\ 7.288 & 1.304 & 0.677 & 3.529 & -3.895 & 0.911 \\ 0.418 & 3.228 & -0.809 & -3.895 & 6.345 & -1.198 \\ 0.815 & -1.043 & 0.81 & 0.911 & -1.198 & 0.58 \end{bmatrix}.$$

We add the groups to `BANYAN` Σ using the parameters listed above. To test the recovery of the initial samples we run `BANYAN` Σ on a sample of stars from *Gaia* EDR3 within 100 pc of the central position of LCC (using the original definition from Gagné et al., 2018). We use all resulting candidates with a kinematic membership probability greater than 50% as the output sample for each population.

We recover a majority of the input stars for all four populations, with Musca having the lowest recovery rate at 56%, and C having the highest, recovering 92% of the initial sample. Musca has the smallest number of stars, and only a fraction of them have radial velocity measurements on which to base the `BANYAN` Σ definition, a likely contributor to the lower recovery fraction. For sub-populations A, B, and C, the recovery rates were $> 75\%$. Many of the stars that are not recovered are placed into a different sub-population (so still part of LCC). In particular, there was significant cross-contamination between groups A and B, and between groups B and C. This was expected, as both groups show significant overlap in spatial and kinematic space, and it is likely the input lists were imperfect.

2.5 Revised ages of the other LCC sub-groups

The LCC subpopulations have discrepant ages in the literature; Goldman et al. (2018) assigned ages of 7–10 Myr for all populations while Kerr et al. (2021) find ages ranging from

13-23 Myr for the same groups. [6] These differences are likely a reflection of differences in methodology and models, as evident by the fact that both references agree on ordering of groups in terms of age. In Section 2.2 we revisited the age of one subgroup (Musca, known as A0 in Goldman et al. 2018 and LCC B in Kerr et al. 2021) and found an age of 11.1±1.4, which is in between and marginally consistent with both (7 Myr and 13 Myr). In this Section we revise the ages of the remaining subpopulations using the isochrone method as in Section 2.2.2.

To ensure a more robust comparison, we place the ages of each population on a consistent scale. We adopt a target selection for each of the four sub-groups using our updated `BANYAN` Σ model described in Section 2.4. We then fit each group using a mixture model identical to what was described in Section 2.2.2. For simplicity, we restrict our analysis to the PARSEC models and solar metallicity. All fits are run with 20 walkers until they passed 50 times the autocorrelation time (checking every 5,000 steps), for a total of 10,000–30,000 steps.

In all cases, our ages are between the values from Goldman et al. (2018) and Kerr et al. (2021). We summarize the results in Table 2.2.

Our fits are mildly sensitive to membership selection, assumed metallicity, or the model grid. Using the original membership list from Goldman et al. (2018) or Kerr et al. (2021) changes our ages at the 1–2 Myr level, small compared to the difference between the two literature ages (5–13 Myr). Adjusting the assumed metallicity at the 0.1 dex level or swapping to the DSEP-magnetic models also changes the derived ages by $\lesssim$2 Myr, but impacted all groups in the same direction.

[6] This section is adapted from an appendix to the paper *"TESS Hunt for Young and Maturing Planets (THYME). IX. A 27 Myr Extended Population of Lower Centaurus Crux with a Transiting Two-Planet System"* by M. Wood et al. (2023), reproduced under the CC 4.0 license with author permission. I led and wrote the paper.

CHAPTER 3: MELANGE-4

This chapter discusses the confirmation and characterization of the MELANGE-4 association. [1]

We report the discovery and characterization of a nearby ($\sim 85\,pc$), older (27 ± 3 Myr), distributed stellar population near Lower-Centaurus-Crux (LCC), initially identified by searching for stars co-moving with a candidate transiting planet from *TESS* (HD 109833; TOI-1097). We determine the association membership using *Gaia* kinematics, color-magnitude information, and rotation periods of candidate members. We measure its age using isochrones, gyrochronology, and Li depletion. While the association is near known populations of LCC, it is older than any previously found LCC sub-group (10–16 Myr) and distinct in both position and velocity. In addition to the candidate planets around HD 109833 the association contains four directly-imaged planetary-mass companions around 3 stars, YSES-1, YSES-2, and HD 95086, all of which were previously assigned membership in the younger LCC. Using the Notch pipeline (Rizzuto et al., 2017), we identify a second candidate transiting planet around HD 109833. We use a suite of ground-based follow-up observations to validate the two transit signals as planetary in nature. HD 109833 b and c join the small but growing population of < 100 Myr transiting planets from *TESS*. HD 109833 has a rotation period and Li abundance indicating a young age ($\lesssim 100$ Myr), but a position and velocity on the outskirts of the new population, lower Li levels than similar members, and a CMD position below model predictions for 27 Myr. So, we *cannot* reject the possibility that HD 109833 is a young field star coincidentally near the population.

[1] This chapter is adapted from the paper *"TESS Hunt for Young and Maturing Planets (THYME). IX. A 27 Myr Extended Population of Lower Centaurus Crux with a Transiting Two-Planet System"* by M. Wood et al. (2023), reproduced under the CC 4.0 license with author permission. I led and wrote the paper.

In Section 3.1, we describe our iterative process for locating members and removing field and LCC interlopers. We discuss our observational program in Section 3.2, with observations both of the planet host and the association members. We describe the properties of the association, including its age, in Section 3.3, and some notable directly-imaged planet-hosting candidate members in Section 3.4. Section 3.5 discusses the properties of the planet host HD 109833, and Section 3.6 the properties of the planets.

3.1 Discovery and Membership

In this Section, we discuss our confirmation that the population of stars spatially and kinematically near HD 109833 is part of a real, co-eval association and the effort to separate out interlopers from nearby LCC populations and the field. As shown later, this does not appear to be part of a known group, so we refer to the association as MELANGE-4 following the naming convention from Tofflemire et al. (2021).

To select the membership of MELANGE-4 we use an iterative four-step process, using a mix of kinematic and age-based indicators of membership. During the first two steps, our goal is to produce a clean membership list, preferring to exclude member stars than to include non-member stars. We then use that clean list to define the properties of the group. This initial list is used to define the group's kinematics for a more expansive search for members in the next two steps. This process is outlined below, and detailed in Sections 3.1.1 – 3.1.4.

1. Initial Selection – we select nearby co-moving stars using the `Comove` algorithm.

2. Remove Interlopers – we apply cuts to the initial candidate list using color, magnitude, and rotation to remove interlopers from LCC and the field.

3. `BANYAN` Σ – we use the refined candidate list to define the group kinematics, then use `BANYAN` Σ and full 6D kinematics (or 5D for those lacking a radial velocity measure-

ment) of each candidate to determine kinematic membership probabilities and search for additional candidate members.

4. Reapply Cuts – We reapply the color and magnitude cuts to the kinematic candidates. This produces the final candidate list, comprised of stars that are clustered in color, magnitude, kinematics, and rotation.

We note that these steps inevitably create some biases in the list. For example, the use of colors and magnitudes to select members may bias the age (depending on how the cuts are applied). For this reason, we provide the candidate membership lists from each step so that readers can apply their own cuts on the data based on the specific scientific case.

3.1.1 Initial Selection

We initially select the co-moving neighbors of HD 109833 using `Comove`[2]. Details of the algorithm are given by Tofflemire et al. (2021). To summarize, `Comove` uses astrometry from the *Gaia* Data Release 3 (DR3, Lindegren et al., 2021; Riello et al., 2021; Gaia Collaboration et al., 2022) and a user-provided velocity of HD 109833 to compute its XYZ position, and UVW velocity [3]. `Comove` then selects every *Gaia* star within a user-defined threshold of HD 109833 in three-dimensional distance and expected tangential velocity ($V_{t,exp}$) assuming a UVW matching HD 109833. We opted to use thresholds of 30 pc and 2 km s^{-1}. This tight limit likely removes many real members (particularly fainter stars with tangential velocity uncertainties larger than 2 km s^{-1}), but larger search radii led to significant contamination from younger LCC stars. From this sample we took those which had valid *Gaia* B_P and R_P magnitudes, yielding an initial selection of 207 stars.

In addition to *Gaia* astrometry, velocities, and photometry, we retrieve the *Gaia* renormalized unit weight error (RUWE) for each candidate member star. The RUWE value is

[2] `https://github.com/adamkraus/Comove`

[3] This is using a galactic coordinate system in which the sun is at $< 0, 0, 0 >$, X points towards the galactic center, Y is in the direction of galactic rotation, and Z is out of the galactic plane. U, V, and W are the velocities in the X, Y, and Z directions, respectively.

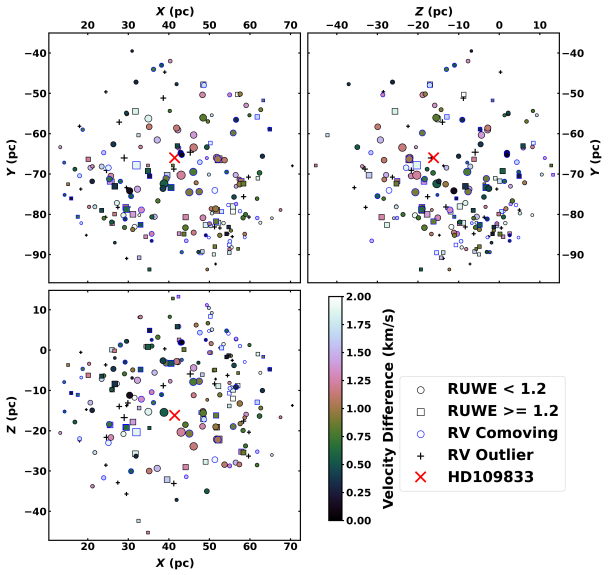

Figure 3.1 The results of the `Comove` search around HD 109833. HD 109833 and neighbors within 30 pc and 2km s^{-1}, are shown in X, Y, and Z coordinates. The size of the points corresponds inversely to their distance from HD 109833, and the color with the velocity difference, so that the largest points are closest to HD 109833 and the darkest points most similar in velocity. Stars with *Gaia* $RUWE \geq 1.2$ are represented with squares. The velocity differences of binary stars are poor indicators of membership, due to velocity from binary motion. Circles are used to represent stars with *Gaia* $RUWE < 1.2$.

related to the goodness-of-fit from the *Gaia* astrometry, normalized to correct for color and brightness dependent effects[4]. The RUWE should be around 1 for well-behaved sources, and higher values suggest the presence of a stellar companion (Ziegler et al., 2018; Belokurov et al., 2020; Wood et al., 2021).

The selection reveals a population of pre-MS stars close to HD 109833 in both position and velocity (Figure 3.1), indicating a young co-moving population. We use this population as our initial membership list. However, it includes many stars which do not appear to be a part of the main population (e.g., main-sequence field interlopers). To remove these probable interlopers, we make a series of cuts on the initial list.

[4]`https://gea.esac.esa.int/archive/documentation/GDR2/Gaia_archive/chap_datamodel/sec_dm_main_tables/ssec_dm_ruwe.html`

3.1.2 Removing LCC and Field interlopers

We make four cuts on the initial sample of candidate members, divided into those meant to remove LCC interlopers and those meant to remove field interlopers. Nearby members of LCC are young, so they cannot be distinguished from this population by CMD position or other age-based qualities, but are kinematically distinct. In contrast, nearby field stars may have similar position and motion to population members, but are unlikely to be young and thus can be identified through differences in age indicators.

For our first cut, we use the empirical main-sequence (MS) defined by Pecaut & Mamajek (2013). We remove all candidates which have $B_P - R_P > 1$, $G - R_P > 0.5$ and are fainter than the interpolated empirical MS (Figure 3.2). This removes 28 candidates out of the initial 207. The anomalous CMD positions of some of these stars are likely caused by poor B_P magnitude and parallax measurements from *Gaia*, but those are still "contaminants" from the perspective of our analysis as including them would bias estimates of the group's age.

The rotation period of a star can also be used as an indicator of age since stars are known to spin down with increasing age. To this end, we measure the rotation periods of 166 candidate members using the Lomb-Scargle periodogram of *TESS* light curves (see Section 3.3.5 for more details). We remove any stars which have high-quality *TESS* data, but do not show a reliable rotation period. Stars with *TESS* magnitude $T > 15$ are not removed, since they are too faint to have adequate signal-to-noise ratio (SNR) for rotation measurement, and thus we cannot reject them as members, as our goal here is to remove only those which we are confident are not members. A total of eight candidates show no reliable rotation, of which four also had a low CMD position (and hence are removed by the cut above).

We remove 18 candidates with *Gaia* DR3 RVs > 5 km s^{-1} from the values predicted by `Comove`, and RV errors < 3 km s^{-1}. These stars may be binaries that are genuine members, but we err on the side of a clean rather than a complete sample.

Lastly, to remove interlopers from the nearby LCC populations, we cross-match our candidate list against the membership list from Goldman et al. (2018), and remove all candidates which are considered LCC members in that paper. We remove five stars for this reason, with an additional Goldman member removed by the earlier velocity cut. It is possible that these stars, which were believed to be members of one of the LCC subpopulations, are actually members of MELANGE-4, but at this stage the goal is to get a clean list even at the cost of removing some true members.

These steps are outlined in the top panel of Figure 3.2. The cuts give a final sample of 152 candidate members.

3.1.3 BANYAN

The `Comove` selection has a sharp radius cutoff, which misses more distant (spatially and kinematically) stars and gives us only general information about the relative probability that a given star is a member. Once a general sense of the spatial distribution is known, a better approach is to use Bayesian membership probabilities that weight the relative likelihood that a star is within MELANGE-4 compared to the field or a nearby association (Rizzuto et al., 2011; Malo et al., 2012).

To this end, we use the `BANYAN` Σ tool. `BANYAN` Σ is a Bayesian probability tool to determine membership probabilities of stars in young moving groups (Gagné et al., 2018)[5]. For each star, `BANYAN` Σ computes the membership probability using kinematic models of 27 nearby, young moving groups defined by Gagné et al. (2018) and the field population.

Significant substructure has been discovered within the LCC association since the publication of `BANYAN` Σ and is not accounted for there, so to correctly select members of MELANGE-4, we use updated parameters for the nearby LCC subpopulations in `BANYAN` Σ, detailed in Section 2.4.

[5] `https://github.com/jgagneastro/banyan.sigma`

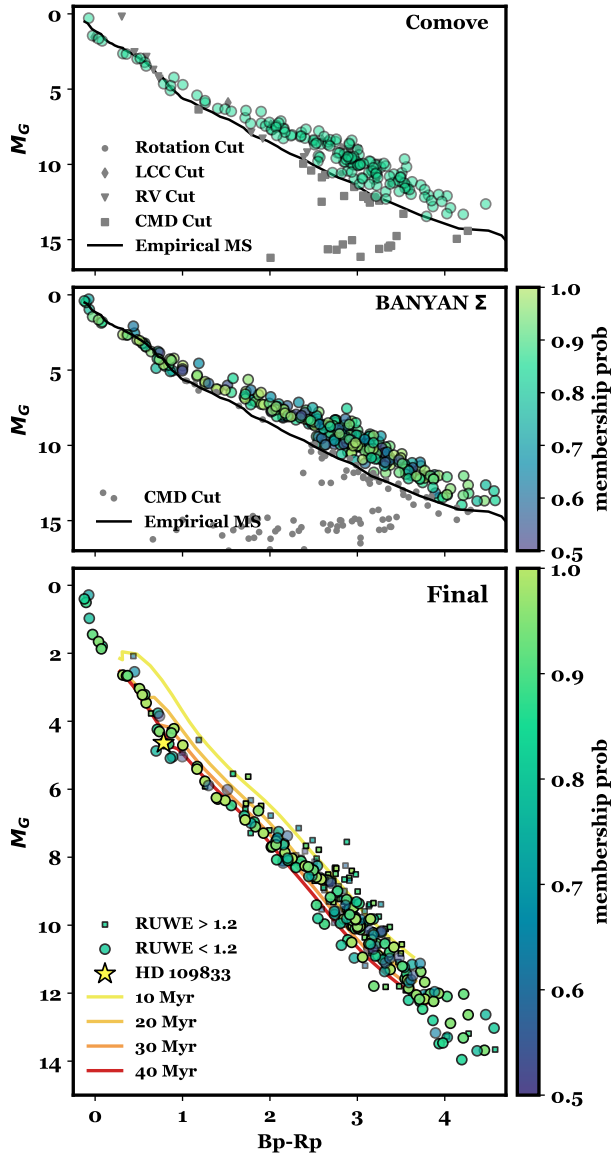

Figure 3.2 A CMD of MELANGE-4 candidates, showing each step of the membership search. The top panel shows the results of `Comove`, and the cuts made on those results to make a tight core membership. The second panel shows the results of `BANYAN` Σ and the subsequent cut on CMD position to remove old interlopers and stars with poor color measurements. Candidates which survived this cut are colored by their kinematic membership probability. The bottom panel shows the final membership list, colored by membership probability. Stars with $GaiaRUWE > 1.2$, possible binaries, are marked as small squares, and form a binary sequence above the main association. Four DSEP magnetic isochrones (Feiden, 2016), showing 10, 20, 30, and 40 Myrs are plotted alongside the sequence. In the top two panels, the ZAMS is shown as a black line, derived empirically by Pecaut & Mamajek (2013).

We add MELANGE-4 to BANYAN Σ following Gagné et al. (2018) by calculating the covariance matrix and center vector of the candidate members which survived all cuts from Section 3.1.2, and had *Gaia* DR3 RV measurements. These are, in units of pc and km s^{-1}:

$$\bar{\bar{\Sigma}} = \begin{bmatrix} 152.32 & 30.929 & 12.03 & 2.813 & 8.634 & 1.424 \\ 30.929 & 143.941 & -22.231 & -0.124 & 4.127 & -1.1 \\ 12.03 & -22.231 & 86.511 & 3.7 & -1.383 & -1.119 \\ 2.813 & -0.124 & 3.7 & 2.732 & -3.434 & -0.535 \\ 8.634 & 4.127 & -1.383 & -3.434 & 7.304 & 1.027 \\ 1.424 & -1.1 & -1.119 & -0.535 & 1.027 & 1.048 \end{bmatrix}$$

$$\bar{x}_0 = \begin{bmatrix} 42.238 & -69.627 & -8.228 & -9.386 & -20.475 & -5.596 \end{bmatrix}$$

Using the updated $UVWXYZ$ matrix for MELANGE-4 and LCC sub-populations, we run BANYAN Σ on all stars within 100 pc of HD 109833 with a *Gaia* DR3 parallax and a parallax over error of > 20. There may be stars outside this range, but those more distant stars would require a more sophisticated model than the multivariate Gaussians used by BANYAN Σ, and we expect them to be a negligible fraction of the overall population at such a young age.

BANYAN Σ yielded 424 candidate members with membership probability greater than 50%. Of the original 152 stars found by Comove, 122 are included in the BANYAN Σ results. There are 168 candidate members with membership probability greater than 90%, which we consider high-probability members. These kinematic candidate members are shown in the middle panel of Figure 3.2.

3.1.4 Final Membership

Since `BANYAN` Σ only considers kinematic information when determining membership probabilities, it is possible that old interlopers, which match the association in $UVWXYZ$ but not in age, are included in the membership list. As with our initial selection from `Comove`, the `BANYAN` Σ selection includes a large number of stars that are below the main sequence. Therefore, we reapply the CMD cut discussed in Section 3.1.2. We also remove 20 stars without *Gaia* Bp or Rp measurements. In total, this step removes 118 stars, yielding a final membership list of 306 stars. Many of these targets may be real members with poor magnitudes or parallaxes. The final membership is shown in the last panel of Figure 3.2. Their membership probabilities and stellar properties are listed in Table 3.2.

3.2 Observations

Below we describe observations of both HD 109833 and candidate members of the parent association. The goal of the former was to characterize the host star and the candidate transiting planets. The latter set of observations focused on confirming membership and measuring the age and kinematic properties of the association. For details of how the sample of 306 candidate association members are identified, see Section 3.1.

3.2.1 TESS Photometry

We use *TESS* photometry to measure the transit properties and to measure rotation periods for the planet host and association members. We use different light curve extractions for these two purposes, as described below.

3.2.1.1 Observations of the planet host

The planet host, HD 109833 (TIC 360630575, TOI-1097), was observed by the *TESS* mission (Ricker et al., 2015) from 2019 Apr 22 through 2019 Jun 18 (Sectors 11 and 12),

then again from 2021 Apr 29 through 2021 Jun 24 (Sectors 38 and 39). The first two sectors have 30 min cadence data, and the Sectors 38 and 39 have 20 s, 2 min, and 10 min cadence data. We employed the 30 min data from the first two sectors and the 20 s data from the last two sectors in this work.

We retrieve light curves for the planet host and candidate members of the parent association from the Mikulski Archive for Space Telescopes (MAST)[6]. For analysis of the planet host, we use the Presearch Data Conditioning Simple Aperture Photometry (PDCSAP; Smith et al., 2012; Stumpe et al., 2012, 2014) *TESS* light curve produced by the Science Processing Operations Center (SPOC; Jenkins et al., 2016).

3.2.1.2 Observations of association members

The PDCSAP reduction can weaken long-term trends in the light curve, which favors exoplanet discovery, but impedes measuring rotation periods beyond $\simeq$10 days. So, to measure the rotation periods of candidate association members, we extract light curves from *TESS* full-frame images using Causal Pixel Models (CPM; Wang et al., 2016) with the `unpopular` package (Hattori et al., 2021). Parameters for running `unpopular` are identical to those described by Barber et al. (2022). We do not extract light curves for stars that were too faint ($T > 15$) or too contaminated by nearby stars (*contratio* > 1.6). In total, we are able to extract usable light curves for 203 of the 306 candidate members. All the *TESS* light curves used in this paper can be found in MAST [7].

We use the resulting *TESS* CPM light curves to measure single-sector rotation periods for stars. For each individual star, we search for periods from 0.1–30 days using a Lomb-Scargle periodogram (Lomb, 1976; Scargle, 1982; Press & Rybicki, 1989). While we search up to 30 days, only stars with $P_{rot} < 12$ days are considered, as the narrow observing window of *TESS* (27 days) makes longer periods unreliable. We perform an eye check following

[6] `https://mast.stsci.edu/portal/Mashup/Clients/Mast/Portal.html`

[7] http://dx.doi.org/10.17909/4cwh-0n56

Rampalli et al. (2021), assigning Quality 0 for clear spot-modulated light curves, Quality 1 to clearly young stars with some ambiguity in their periodogram peaks, Quality 2 to spurious measurements, and Quality 3 to complete non-detections. We visually removed eclipsing binary signals and targets with blended light curves (not all get captured by our contamination ratio requirements). If multiple sectors are available, we report the average of the single-sector measurements after clipping ones that disagree with the clearest signal (strongest Lomb-Scargle power) by more than 25% to eliminate double or half harmonics. Out of 185 candidate members with usable light curves, we assign Quality 0 or 1 to 173 stars.

3.2.2 High Contrast Imaging

We use High Contrast Imaging to search for close-companion stars to HD 109833. The data we use can be found on ExoFOP-TESS[8].

3.2.2.1 ZORRO/Gemini

To search for close-companion stars that might dilute the transit signal, we observed HD 109833 on 2020 Mar 13 UT with the Gemini South speckle imager, Zorro (Scott et al., 2021). We used the standard speckle imaging mode with narrowband 562 nm and 832 nm filters. The 'Alopeke-Zorro instrument team took all data as part of their program queue operations and reduced the data with their standard pipeline (Howell et al., 2011).

No close companions were detected in either band. The 832 nm filter sets stronger contrast limits, ruling out equal-mass companions at separations $\rho > 0.05''$, additional companions with $\delta 832 < 4.6$ magnitudes at $0.1''$, and with increasing contrast sensitivity from there out to $\rho = 1.2''$.

[8] `https://exofop.ipac.caltech.edu/tess/target.php?id=360630575`

3.2.2.2 HRCam/SOAR

We also search for previously unknown companions to HD 109833 using data from the SOAR speckle imaging camera (HRCam; Tokovinin, 2018) taken on 2020 Feb 10 UT. Observations were taken using the I band. As with the Zorro data, we detect no companions in the HRCam data out to $\rho = 3''$. Companions with $\delta I < 1$ are ruled out for $\rho > 0.1''$, and those with $\delta I < 4.5$ ruled out at $\rho > 0.25''$.

3.2.3 Spectroscopy

To confirm membership in the association and measure the association's age we gather spectra of candidate association members. Our goals are to estimate the equivalent width of the Li I 670.8 nm line. The extracted equivalent widths are given in Table 3.2.

We also obtain spectra of TOI-1097 over three years with the goal of checking for signs of binarity. Our analysis of the resulting velocities, detailed in Section 3.6.3 , shows no evidence of binarity. All radial velocities, organized by instrument, are given in Table 3.1.

3.2.3.1 Goodman/SOAR Spectroscopy

We observe a total of 26 candidate association members using the Goodman High Throughput Spectrograph (Clemens et al., 2004). Goodman is part of the Southern Astrophysical Research Telescope (SOAR) atop Cerro Pachon, Chile. Observations were taken over 8 nights between 2021 Mar 29 and 2021 Sept 20, under mostly photometric conditions.

From the list of candidate association members, these 26 are selected for observation with the goal of mapping out the lithium depletion boundary (LDB). To choose stars to observe we estimate the age of the association from an isochrone, and use that age to predict the magnitude of the LDB in M_{Ks}. We then select stars with $\Delta K < 1$ from the predicted boundary. This estimate was updated as we took more data and revised the age of the group, so there was no single observing list. We choose stars for observing based on their magnitude in *Gaia* R_P (prioritizing brighter stars that need shorter exposures), *Gaia* RUWE

Table 3.1 RV Measurements of TOI-1097.

Telescope	BJD UT	RV km s^{-1}
HARPS/La Silla	2458858.8137	10.563 ± 0.002
HARPS/La Silla	2458859.8226	10.598 ± 0.003
HARPS/La Silla	2458861.8281	10.571 ± 0.002
HARPS/La Silla	2458862.8580	10.614 ± 0.003
HARPS/La Silla	2458863.8108	10.548 ± 0.002
HARPS/La Silla	2458864.8653	10.577 ± 0.002
HARPS/La Silla	2458865.8660	10.603 ± 0.002
CHIRON/SMARTS	2459240.8846	10.577 ± 0.052
CHIRON/SMARTS	2459306.7098	10.568 ± 0.03
CHIRON/SMARTS	2459308.7235	10.689 ± 0.064
CHIRON/SMARTS	2459312.6771	10.621 ± 0.04
CHIRON/SMARTS	2459314.7458	10.576 ± 0.042
CHIRON/SMARTS	2459322.7661	10.528 ± 0.058
CHIRON/SMARTS	2459337.6306	10.646 ± 0.083
CHIRON/SMARTS	2459338.6142	10.558 ± 0.115
CHIRON/SMARTS	2459339.6936	10.573 ± 0.053
CHIRON/SMARTS	2459346.5901	10.571 ± 0.074
CHIRON/SMARTS	2459742.5434	10.599 ± 0.037
NRES/LCO	2459672.5589	10.757 ± 0.138
NRES/LCO	2459673.5576	10.809 ± 0.203
NRES/LCO	2459675.6047	10.917 ± 0.162

Note. — Measured radial velocities of HD 109833. A 1.4 km s^{-1} offset was added to the measurements from CHIRON/SMARTS in accordance to the zero-point of that instrument.

(omitting stars with $RUWE > 1.2$ as they are more likely to be binaries), and location on sky (prioritizing short slews between targets and middle elevations).

Observations were designed to measure the EW of the Li I 670.8 nm line; we use the red camera, the 1200 l/mm grating, and the M5 mode, which provides a wavelength coverage of $630 - -740$ nm. We use either the 0.45" slit, or the 0.6" slit, depending on the magnitude of the target and atmospheric seeing. This setup should give a resolving power of $R = 4500 - -5800$, although in practice the true resolution is lower and varies with exposure

time (see below). For each target, we take five spectra with exposure times varying from 10 s to 300 s each.

For reduction, we perform standard bias subtraction, flat-fielding, and optimal extraction of the target spectrum. The spectra show large wavelength shifts while observing, likely due to issues with the mount model and flexure compensation system. In extreme cases, this shifts the spectrum by 5-10 pixels between exposures of the same target, which corresponds to several resolution elements (depending on the slit). To mitigate the effect, we take Ne arcs prior to each target and use simultaneous skyline spectra to calibrate the wavelength solution of individual spectra. The combination of a pre-target arc and skylines performs better than bracketing the data with arcs. We make an initial map of pixels to wavelengths using a fourth-order polynomial derived from the nearest Ne arc, then apply a linear correction to each spectrum based on the sky lines. We stack the extracted and wavelength-calibrated spectra using a robust weighted mean. The stacked spectra have mean $SNR > 40$ for all targets.

We correct each star to its rest wavelength using radial-velocity standards taken with the same setup. Although the resulting spectra were sufficient for spectral typing and measuring relevant equivalent widths (e.g., EW[Li]), the radial velocities proved to be poor ($\sigma_{\rm rv} \simeq 5 - -10$ km s^{-1} based on stars with known velocity). This is likely due to non-linearity in the wavelength shifts impacting the edges of the spectrum and regions with fewer sky lines and non-uniform shifts during an exposure. As a result, we do not report velocities based on these spectra.

3.2.3.2 NRES/LCO

To increase the baseline of our RV characterization of HD 109833, we obtain three spectra of HD 109833 using the Network of Robotic Echelle Spectrographs (NRES) (Siverd et al., 2018) at the Las Cumbres Observatory. Observations were taken the nights of 2022 Apr 3, 4, and 5.

NRES spectra cover $380 - -860$ nm at high resolving power ($R \sim 53,000$). The data are reduced using the LCO NRES pipeline `BANZAI-NRES`[9]. This includes extraction of radial velocities by cross-correlating observed spectra with PHOENIX model atmospheres (Husser et al., 2013).

3.2.3.3 HARPS

For RV characterization of the planet host HD 109833, we also obtain seven spectra of that star taken with the High Accuracy Radial velocity Planet Searcher (HARPS) fiber-fed Echelle Spectrograph on the ESO 3.6m telescope at La Silla Observatory under the NCORES large programme (ID 1102.C-0249, PI: Armstrong). The spectra have high-resolution ($R \sim$ 115000), and cover a spectral range of 378–691 nm. Observations were taken on the nights of 2020 Jan 10–11 and 13–17 in high-accuracy mode (HAM), with an exposure time of 1500-1800s, depending on observing conditions, and a typical SNR per pixel of 100. The standard online HARPS data reduction pipeline reduces the data, using a G2 template to form the weighted cross-correlation function (CCF) to determine the RVs. We find a typical error on the RVs of 2–3 $\mathrm{m\,s^{-1}}$.

3.2.3.4 CHIRON/SMARTS

We acquired twelve spectra of HD 109833 using CHIRON at the SMARTS 1.5 m telescope at Cerro Tololo Inter-American Observatory (Tokovinin et al., 2013) between 2021 Jan 26 and 2022 June 12. We used CHIRON in its image slicer mode, which gives a resolving power of $\approx$ 79,000 across 415–880 nm.

We also acquire spectra of two MELANGE-4 candidate members on 2021 Apr 30, and 2021 May 4 using the same setup and reduction.

To derive the RVs and stellar parameters for the eleven spectra that met our SNR requirements, we follow the methods described by Zhou et al. (2018). We perform a least-squares

[9] `https://github.com/LCOGT/banzai-nres`

deconvolution of the spectra using non-rotating synthetic spectral templates (Donati et al., 1997). These templates are constructed using the ATLAS9 atmosphere models (Castelli & Kurucz, 2004) and the `SPECTRUM` script (Gray & Corbally, 1994). The resulting line profiles were fit using a broadening kernel that included terms for the rotational, macroturbulent, and instrumental broadening. We then fit the line profile from each observation independently, yielding the RVs listed in Table 3.1, as well as a mean rotational broadening velocity of $v \sin i_\star = 10.5 \pm 0.2 \mathrm{km\,s^{-1}}$.

Table 3.2 Members of MELANGE-4.

DR3 ID	RA	Dec	RUWE	G	P_{BANYAN}
	°	°		mag	
Gaia DR3 5269346361575307264	121.3139	-71.103	0.927	11.62	0.815
Gaia DR3 5314992445071183872	130.1828	-57.550	1.354	14.22	0.554
Gaia DR3 5215182391566488448	135.4216	-77.933	1.112	15.12	0.868
Gaia DR3 5304828971900544896	136.2097	-56.294	1.159	12.64	0.706
Gaia DR3 5216186726719969792	139.3644	-74.734	1.070	5.86	0.921
Gaia DR3 5219515292014933760	139.6958	-70.615	1.078	15.67	0.540
Gaia DR3 5217812354662194048	140.9457	-73.682	1.227	13.38	0.555
Gaia DR3 5250471114189790336	141.6836	-63.023	2.249	14.26	0.546
Gaia DR3 5219351911459314048	142.6309	-70.697	0.944	10.08	0.755
Gaia DR3 5217846851839896832	142.8546	-73.747	1.589	9.19	0.815
Gaia DR3 5217846817480160640	142.9057	-73.751	1.966	13.90	0.728
Gaia DR3 5217554622264363008	143.5176	-74.093	1.277	14.29	0.729
Gaia DR3 5250926999202194688	143.8354	-62.367	1.206	14.45	0.730
Gaia DR3 5251098523021221376	144.8372	-61.328	0.791	4.48	0.723
Gaia DR3 5244271552233795200	145.1523	-67.755	1.108	16.46	0.618
Gaia DR3 5307852908070273792	145.5575	-56.027	1.128	14.39	0.598
Gaia DR3 5218453026345066368	147.2531	-71.634	2.566	13.90	0.582
Gaia DR3 5257836605156299776	147.5025	-58.472	1.163	14.23	0.537
Gaia DR3 5218262707753445760	147.6715	-71.783	1.111	14.79	0.887
Gaia DR3 5257392295070412032	148.5564	-60.275	1.070	12.32	0.952
Gaia DR3 5259151277454731008	149.3857	-58.390	14.572	15.49	0.509
Gaia DR3 5258252942105518080	150.9937	-59.401	1.285	14.23	0.552
Gaia DR3 5230321567172871040	151.3447	-71.616	2.216	14.60	0.968
Gaia DR3 5230321361014440704	151.3556	-71.624	5.079	12.45	0.952
Gaia DR3 5253295141117135104	152.1298	-61.633	1.138	15.46	0.743
Gaia DR3 5246284685000163968	152.6949	-65.380	1.214	12.94	0.502
Gaia DR3 5254979283697117440	154.0168	-59.909	1.225	13.88	0.966
Gaia DR3 5255082603415689600	154.3064	-59.640	1.181	15.42	0.968
Gaia DR3 5251591482193147776	154.7628	-64.681	1.303	13.38	0.978
Gaia DR3 5251591477884660352	154.7696	-64.676	1.119	6.48	0.844

Note. — Table is truncated. The full version is available online.

Table 3.3 Observations of MELANGE-4 candidate members.

Object	Telescope	ObsDate YYYYMMDD	M_K mag	EW(Li) mÅ
TIC 427036962	Goodman/SOAR	20210329, 20210919	6.52	413.0
TIC 258101273	Goodman/SOAR	20210329	4.83	29.0
TIC 259726904	Goodman/SOAR	20210329	5.01	< 10
TIC 68515382	Goodman/SOAR	20210423	6.09	153.0
TIC 378413560	Goodman/SOAR	20210423	4.98	< 10
TIC 253067348	Goodman/SOAR	20210423	6.38	680.0
TIC 303048907	Goodman/SOAR	20210423	5.90	< 10
TIC 378126824	Goodman/SOAR	20210423	5.27	20.0
TIC 406249571	Goodman/SOAR	20210423	5.73	583.0
TIC 401561267	Goodman/SOAR	20210501	5.42	34.0
TIC 453766186	Goodman/SOAR	20210501	5.63	< 10
TIC 453808153	Goodman/SOAR	20210501	5.78	< 10
TIC 401484858	Goodman/SOAR	20210507	6.11	16.0
TIC 402030604	Goodman/SOAR	20210507	5.72	< 10
TIC 335366271	Goodman/SOAR	20210507	5.93	33.0
TIC 451425923	Goodman/SOAR	20210507	6.23	< 10
TIC 402808278	Goodman/SOAR	20210507, 20210810	5.70	< 10
TIC 425871236	Goodman/SOAR	20210810	5.53	< 10
TIC 299610396	Goodman/SOAR	20210810	5.78	< 10
TIC 97882429	Goodman/SOAR	20210810	5.84	< 10
Gaia5227091236372916864	Goodman/SOAR	20210810	6.09	414.0
TIC256168939	Goodman/SOAR	20210810	5.89	204.0
TIC189421351	Goodman/SOAR	20210919	4.07	313.0
TIC461148251	Goodman/SOAR	20210919	5.17	< 10
TIC443273186	Goodman/SOAR	20210920	6.90	< 10
TIC361571108	Goodman/SOAR	20210920	6.87	456.0
TYC 9034-968-1	CHIRON/SMARTS	20210430	3.70	250.0
TYC 8992-346-1	CHIRON/SMARTS	20210504	3.34	340.0

3.3 Properties of the MELANGE-4 Association

3.3.1 MELANGE-4 in the context of nearby associations

The central position and velocity of MELANGE-4 is near the LCC population on the southern part of Sco-Cen and is on the western edge of the Carina association. Despite its proximity to these populations, the positions and velocities of members make it clear that

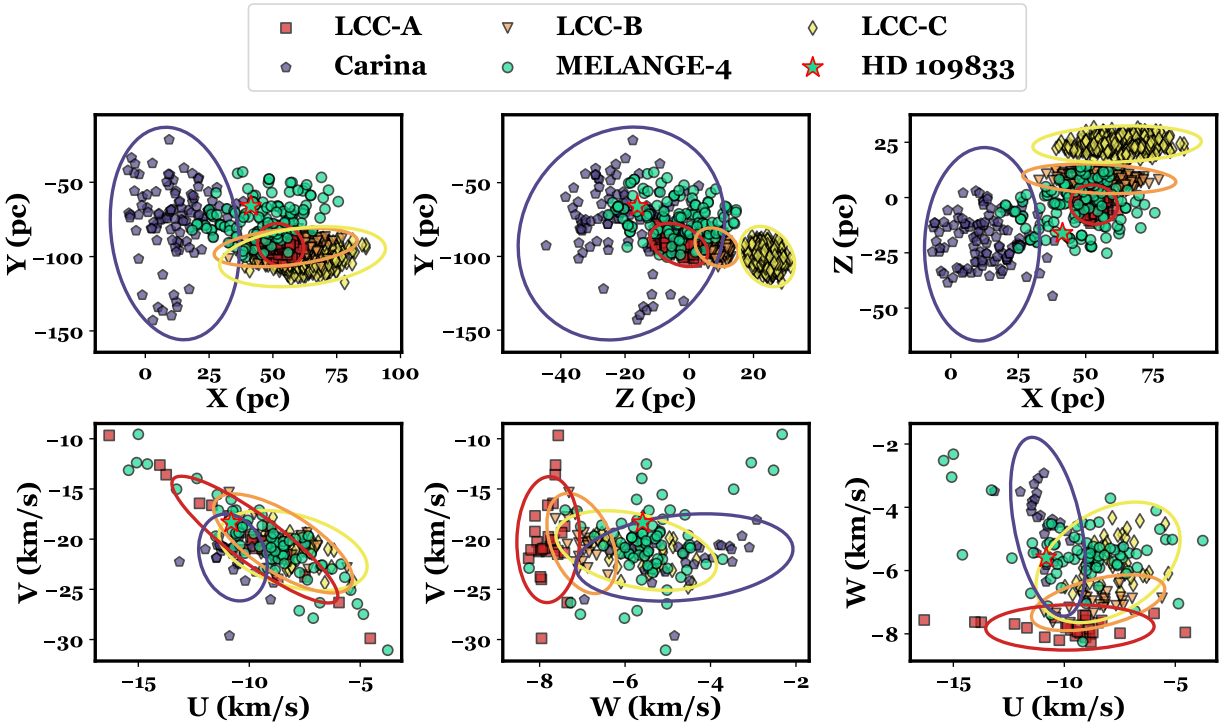

Figure 3.3 The spatial and velocity spreads of MELANGE-4, the nearby LCC sub-populations, and Carina. The top row shows the galactic position (X, Y, and Z) for each population, and the bottom row the velocities (U, V, and W). The membership candidates for MELANGE-4 are shown in turquoise, and high probability ($> 99\%$) members of LCC-A, LCC-B, LCC-C, and Carina are shown in red, orange, yellow, and purple respectively. Ellipses show the 1σ extents of the Gaussian model of the associations. The position of HD 109833 is marked with a turquoise star.

MELANGE-4 is not part of any known associations. This is demonstrated in Figure 3.3 and described in further detail below.

Recent research has split LCC into 4 sub-populations (Goldman et al., 2018; Kerr et al., 2021), which we consider separately. Goldman et al. (2018) found four sub-populations: LCC-A0, LCC-A, LCC-B, and LCC-C, from youngest to oldest. The same sub-populations were found by Kerr et al. (2021), where they were named LCC-B, LCC-C, LCC-E, and LCC-D, respectively. We use the names from Goldman et al. (2018) and focus on LCC-A, LCC-B, and LCC-C, as these are the closest to MELANGE-4. Musca (LCC-A0) is the youngest of

the sub-populations (11 ± 2Myr), and the furthest from MELANGE-4. More details on the kinematics and ages of these sub-populations are discussed in Chapter 2.

MELANGE-4 shows significant spatial overlap with LCC-A and partial spatial overlap with LCC-B, but is completely separate from both sub-populations in W. In terms of velocity, it overlaps partially with LCC-C, from which it is furthest in XYZ. Only 3-4 stars in our list of candidate members of MELANGE-4 overlap with a single LCC group in both XYZ and UVW (the sources with the most negative W in Figure 3.3). As expected, these have the lowest membership probabilities (50–60%). As we show later in this Section, at 27 ± 3 Myr, MELANGE-4 is also significantly older than the closest LCC sub-groups.

In addition to the LCC subgroups, MELANGE-4 has kinematic overlap with the Carina association. However, the mean X of MELANGE-4 is $\simeq 40$ pc from the center of Carina. Similarly, most age estimates for Carina find an age of $\simeq 40$ Myr (e.g., Torres et al., 2008; Bell et al., 2015; Wood et al., in prep) which are inconsistent with the age we find for MELANGE-4. Booth et al. (2021) find a younger age for Carina ($\simeq$15 Myr), but this is still inconsistent with our age of MELANGE-4.

One thing that stands out is how diffuse the group is in XYZ space compared to known LCC populations. This makes it look like a group transitioning from the more tightly packed population within large complexes towards the more diffuse moving groups (e.g., Kraus et al., 2017). The broad distribution can explain why the group was not noticed prior to the arrival of *Gaia* data, as well as why many members were previously thought to be part of LCC or Carina.

3.3.2 Lithium Depletion Boundary

We measure the LDB age of the association using the SOAR/Goodman spectra described in Section 3.2.3.1. We estimate the equivalent width of the Li I 6708 Åline (EW[Li]), using a pseudo-continuum estimate from a linear fit to the region on either side of the line. To account for variations in the line width ($v \sin i_*$ and resolution differences between spectra)

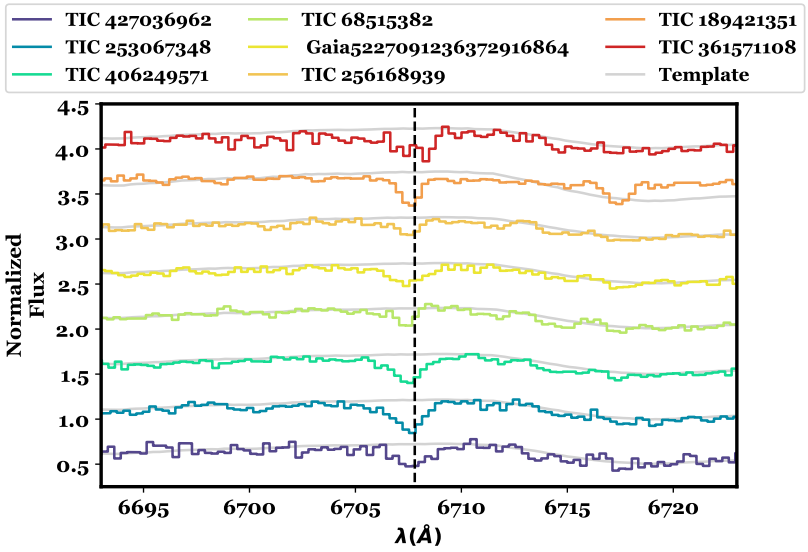

Figure 3.4 Spectra of all MELANGE-4 members with measured Li absorption, overplotted with a Li free M-dwarf template (gray; Bochanski et al., 2007). The location of the Li line, 6707.8 Å, is marked with a dashed black line. Two of these stars, TIC 68515382 (light green) and TIC 256168939 (light orange), have $EW(Li) < 300$ mÅ, and thus are not fully Li-depleted.

we manually adjust the width of the Li region to include both line edges. Spectra of all association members with measured Li absorption are shown in Figure 3.4. Our analysis does not account for contamination from the nearby Fe line (6707.4 Å) in the FGK stars nor molecular contamination of the continuum in the cooler M dwarfs. As a result, the uncertainties are likely no better than 10% independent of SNR. The EWs are listed in Table 3.3 and plotted in Figure 3.6.

To locate the LDB we must define a threshold between Li-rich and Li-poor stars. We have chosen a threshold of EW[Li]$\geq$ 300 mÅ, following the reasoning of Binks et al. (2021), and using the curve of growth from Zapatero Osorio et al. (2002). As a proxy for stellar mass or $T_{\rm eff}$, we use the absolute K_S-band magnitudes from 2MASS with parallaxes from *Gaia* DR3. K_S is less sensitive to metallicity (Mann et al., 2019), reddening, and spots (Somers et al., 2020) than *Gaia* colors, and is broadly available for our targets.

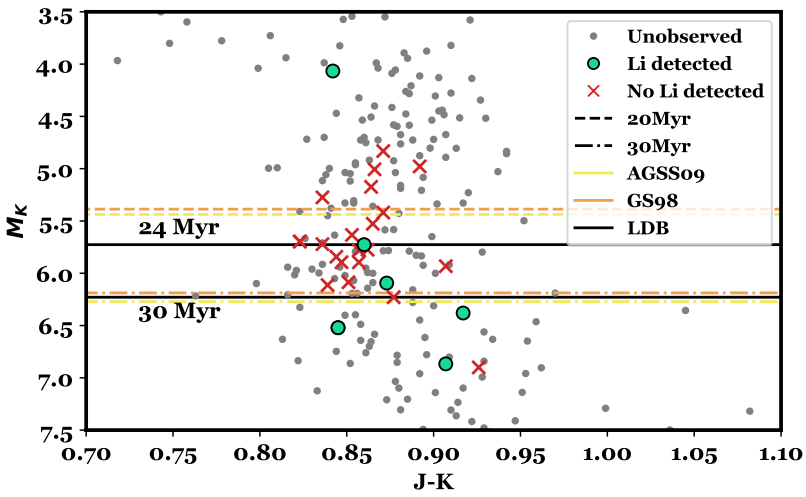

Figure 3.5 The Lithium Depletion Boundary of MELANGE-4. Shown is the color (J−K) and absolute magnitude (K_s) of members of MELANGE-4. Observed stars with $EW(Li) > 300$ mÅ are shown as colored dots, and stars with $EW(Li) < 300$ mÅ as red X's. Candidate association members which were not observed are shown as gray dots. Orange and yellow lines show the predicted 20 and 30 Myr 99% lithium depletion boundaries using the DSEP magnetic models with two different solar abundances. The 30 Myr GS98 line has been moved up by 0.03 magnitudes to increase visibility. The solid black lines through the brightest M-dwarf with Li absorption, and the faintest likely member without Li absorption show the edges of the boundary region.

As expected, we identify a region above which no Li is present and below which all high-probability members have Li (see Figure 3.5). The single star with a Li detection at $M_K = 4$ (TIC 189421351) is more massive than the other stars and is expected to have undepleted Li (see Figure 3.6). The star with no detected Li and $M_K = 6.9$ (TIC 443273186) has a low CMD position and is a likely field interloper, so we exclude it from this analysis. The upper boundary of this region is defined as the magnitude of the brightest star which we have observed to have $pEW(Li) > 300$ mÅ, and the lower boundary by the magnitude of the faintest star with $pEW(Li) < 300$ mÅ. Using that definition, we find that the LDB region spans $5.7 < M_K < 6.1$. Using a more generous definition of 200 mÅ for Li-rich (e.g., Binks & Jeffries, 2014) adds one additional Li-rich star at $M_K = 5.9$. This did not affect our LDB region or measured age.

We determine the age of MELANGE-4 by comparing this LDB location to several stellar evolution models with varying assumptions (e.g., magnetic field strength and spot coverage). For each model, we define the LDB as the magnitude at which Li has been depleted from the initial amount by 99%. We use isochrones taken from Baraffe et al. (2015) (BHAC15), and the Dartmouth Stellar Evolution Program (DSEP; Dotter et al., 2008) as our baseline models. For the treatment of magnetic fields, we use isochrones from Feiden (2016), which are built on top of the DSEP models. The magnetic DSEP models include grids built on two different sets of solar abundances, from Grevesse & Sauval (1998) (GS98), and Asplund et al. (2009) (AGSS09). These different abundance scales produce slightly different predictions for Li depletion, leading to different LDB ages, as shown in Table 3.4. For spots, we used the spot models from Somers et al. (2019, 2020).

We list the resulting age bounds from each model in Table 3.4. The age ranges from each model are broadly consistent, with lower age bounds ranging from 23 Myr to 26 Myr, and upper age bounds between 28 Myr and 32 Myr. The largest age discrepancies come from using the SPOT models with spot fractions >50%. While individual stars may have large spot fractions (Gully-Santiago et al., 2017), we expect the bulk of the stars here to have spot fractions $\lesssim 30\%$ (Cao et al., 2022; Savanov et al., 2018; Klein et al., 2022). Thus, we include the ages from the SPOT model of only 17% and 34% spot coverage in the table, both of which are consistent with the ages from the other models tested.

We take 27 ± 3 Myr as the age of the association to encompass all these estimates.

A number of effects could cause Li-poor stars to appear above the LDB or vice versa. Unresolved binary stars which are Li-rich could appear to be as much as 0.75 magnitudes brighter than the individual components, raising them on the CMD to look younger. Baraffe & Chabrier (2010) suggested that cold, episodic accretion onto young low-mass stars could cause early Li depletion in individual stars, leading a star to look older, but Sergison et al. (2013) found no evidence for this in two young associations, and it should not impact the age estimates here because we have multiple reliable detections. Poor parallaxes (e.g., on

Table 3.4 LDB results for MELANGE-4.

Model	Lower Bound	Upper Bound
BHAC15	24 Myr	28 Myr
DSEP (GS98)	23 Myr	29 Myr
DSEP Mag (GS98)	24 Myr	30 Myr
DSEP Mag (AGSS09)	26 Myr	32 Myr
SPOT (17%)	23 Myr	31 Myr
SPOT (34%)	24 Myr	31 Myr

.

Note. — Upper and lower age bounds given by each of the models used. The upper bound corresponds to the age given an LDB at the magnitude of the faintest observed star without Li, and the lower bound corresponds to the age given an LDB at the magnitude of the brightest observed stars with Li.

binaries), and stellar variability may also affect the CMD position at the $\lesssim 0.1$ mag level, which can explain some of the spread.

The most likely cause of anomalous stars is non-member interlopers, either younger interlopers from the nearby LCC populations or older interlopers from the field. A possible example of this is the star TIC 443273186, which is the least luminous star we observed at $M_K = 6.9$, but has no significant Li detection. This star has a low CMD position compared to other association candidate members, and is likely a field interloper rather than an association member.

3.3.3 Li Sequence

While the LDB in low-mass stars is the most accurate method of using Li measurements to determine association age, it is also possible to estimate an association's age by examining the full sequence of Li abundance as a function of color (see Soderblom et al., 2014, for a review). Because this method uses Li abundance, rather than the simple threshold used by the LDB and requires conversion between modeled A(Li) and measured EW(Li), it is more model-dependent than the LDB method, but serves here as an additional check on the association age.

First, we compare the magnetic DSEP stellar-evolution models (Feiden, 2016) against the Li measurements of MELANGE-4 M-dwarf members, shown in the left panel of Figure 3.6. We convert EW(Li) to Li/Li_0 by dividing each by the predicted initial EW(Li) for M-dwarfs from Zapatero Osorio et al. (700 mÅ 2002). The measured values lie between the models for 20 and 30 Myr associations. Next, we compare the Li sequence of MELANGE-4 against that of three benchmark associations with ages ranging from 3–40 Myr. We supplement our EW(Li) measurements of MELANGE-4 members (see Section 3.2.3 and Table 3.3) with literature measurements for five higher-mass stars, taken from Mamajek et al. (2002); Torres et al. (2006), and Pecaut & Mamajek (2016). The Li sequence of MELANGE-4 lies on top of that of the 24 Myr old β Pic association, shown in orange in the right panel of Figure 3.6. The association has more Li at $B_P - R_P \simeq 3.0$ than the older Tuc-Hor association ($40\,Myr$), and lower Li (more depletion) at $1.7 < B_P - R_P < 3.0$ when compared to the younger 3–5 Myr ϵ Cha association. Both of these tests support our measured LDB age of 27 ± 3 Myr.

3.3.4 Age from Isochrones

We independently estimate the age of MELANGE-4 by comparing the CMD to solar-metallicity isochrones using a Gaussian mixture model. For this analysis, we use the solar-metallicity PARSEC (v1.2S) models (Bressan et al., 2012) rather than one of the models used in the lithium analysis (Section 3.3.2), as those models do not reach the most massive association members critical for differentiating between ages. Following Mann et al. (2022), we use a mixture model,[10] based on the method outlined by Hogg et al. (2010) and a Monte-Carlo Markov-Chain framework with `emcee` (Foreman-Mackey et al., 2017). The basic method is to fit the population with the combination of two models, one describing the single-star sequence of members, and one describing everything else (outliers). The second population may itself contain multiple populations, such as binaries, field interlopers, and young stars in Sco-Cen but not part of MELANGE-4.

[10] `https://github.com/awmann/mixtureages`

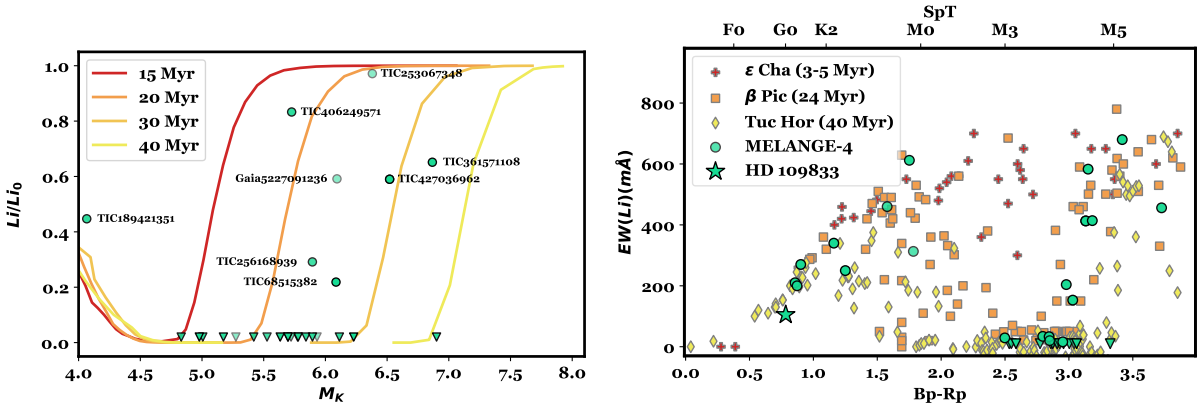

Figure 3.6 Lithium measurements of MELANGE-4 members. Left) Fraction of initial Li abundance as a function of absolute K magnitude, overplotted with DSEP magnetic isochrones (Feiden, 2016). Equivalent widths of association members were converted to Li/Li_0 using the curve of growth from Zapatero Osorio et al. (2002). The transparency of the points corresponds to their kinetic membership probability from `BANYAN` Σ, such that the most likely interlopers are the faintest. Right) Comparison of MELANGE-4 Li sequence and Li sequences of known associations. For members of each association, Li equivalent widths are shown as a function of *Gaia* Bp−Rp. Equivalent widths of MELANGE-4 members marked with downward triangles are upper limits. The transparency of the points corresponds to their kinetic membership probability from `BANYAN` Σ, such that the most likely interlopers are the faintest. Li measurements of MELANGE-4 members are supplemented with additional five measurements from Mamajek et al. (2002); Torres et al. (2006), and Pecaut & Mamajek (2016). The Li measurements of β Pic members are taken from Shkolnik et al. (2017), measurements of ϵ Cha members from Murphy et al. (2013), and measurements for Tuc-Hor from da Silva et al. (2009) and Kraus et al. (2014)

.

The fit has six free parameters (units in brackets): the association age (τ [myr]), the average reddening across the association ($E(B-V)$ [mags]), the amplitude of the outlier population (P_B), the offset of the outlier population from the main population CMD (Y_B [mags]), the variance of the outliers around the mean (V_B [mags]), and a term to capture missing uncertainties or differential reddening across the association (f [mags]). All parameters evolve under uniform priors bounded by physical barriers, although E(B−V) is allowed to go negative to avoid Lucy-Sweeney bias. We re-sample the isochrone grid to ensure uniform sampling in age. We run the MCMC with 50 walkers until it passed at least 50 times the autocorrelation time after a burn-in of 5,000 steps (a total of 30,000 steps).

We compare the models to *Gaia* photometry and parallaxes of the final membership list described in Section 3.1.4. While the mixture model can handle outliers, it can be sensitive to multiple kinds of outliers as we expect here (binaries, LCC members, field stars, targets with poor parallaxes or photometry). To account for this, we remove stars with RUWE$>$ 1.4 (likely to be binaries; Ziegler et al., 2019; Wood et al., 2021), stars with SNR$<$30 in their parallax or any photometry, and any target outside the range of our model grid. This reduces the list of stars to 219.

As Figure 3.7 shows, the isochrone fits the sequence relatively well. One region of disagreement are the under-luminous G dwarfs around $B_P - R_P \simeq 0.9$, which includes HD 109833. At 20–30 Myr, this part of the CMD corresponds to a stars' transition into He-3 burning, which leads to a rapid drop in the brightness of the star during the transition period. The resulting bend in the CMD is seen in the models as well as the similar-aged β Pic (Mamajek & Bell, 2014). The fit is marginally consistent with the observations of HD 109833, but the three redder stars appear to be main-sequence interlopers. HD 109833's CMD position is an excellent match to the 30 Myr (and older) isochrones, so the discrepancy may be due to a modest (2–3 Myr) age spread, or other systematics in the models. Another possibility is that HD 109833 is a young field interloper, which we discuss further in Section 5.1.2.

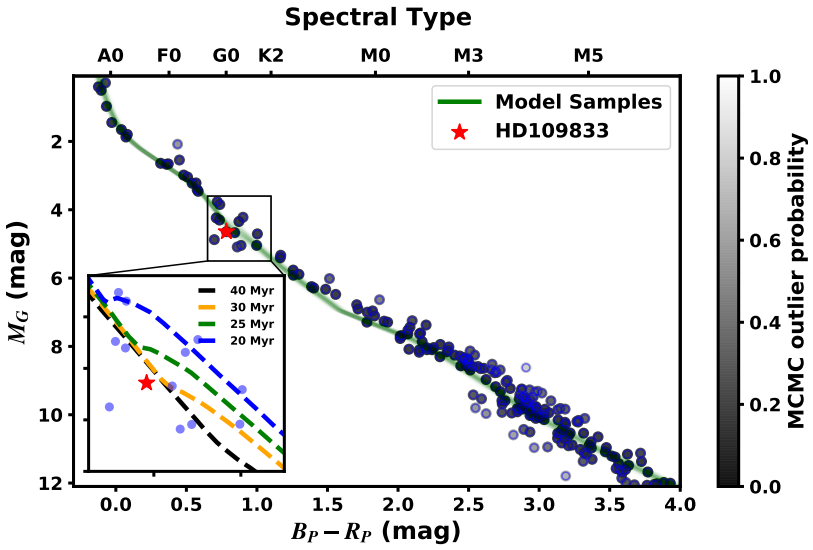

Figure 3.7 Comparison of high-probability MELANGE-4 members (circles) with PARSECv1.2 stellar evolutionary models. Stars are shaded by their outlier probability, as determined by the mixture model fit. Outliers are not necessarily non-members. The red star shows the planet host (HD 109833). The green lines are 100 random draws from the MCMC using the PARSEC isochrones and fit reddening. The inset shows the region around HD 109833 and representative-age model predictions of representative ages.

The best-fit age from our fit is 26.0±2.1 Myr. Repeating the analysis with the Dartmouth Stellar Evolution Program (DSEP; Dotter et al., 2008) with magnetic enhancement (Feiden, 2016) yields a consistent but slightly older age of 27.1 ± 2.3 Myr. We use the age from the PARSEC fit because the DSEP models did not include stars above $1.7 M_\odot$ at this age. These high-mass stars provide an age constraint independent of the LDB age (which relies on mid-M dwarfs).

Fitting the full population without the cuts above gives a younger age (23 ± 3 Myr). However, when using the full sample the outlier model fits the main-sequence interlopers, treating binaries and LCC interlopers as part of the main population (both of which bias the fit to younger ages). Similar small adjustments to the fitting method, such as non-solar composition, also change the resulting age at the $\simeq 2$ Myr level, generally preferring older ages. This suggests that the systematic errors are comparable to measurement errors. All ages agree well with our 27 ± 3 Myr age from the LDB (Section 3.3.2).

3.3.5 Age from rotation

The rotation sequence can be used to constrain the age of a population (e.g., Tofflemire et al., 2021; Andrews et al., 2022; Newton et al., 2022; Messina et al., 2022). For < 100 Myr associations, this is more challenging because many late-type stars are still spinning up as they contract onto the main sequence and Sun-like or warmer stars have not yet moved onto the slow-rotating sequence (Rebull et al., 2018). However, the *spread* in rotation periods within a group is still a useful proxy for age. For example, the period spread in Upper Sco, which is ~ 10 Myr old, is much greater than for 40–60 Myr associations like Tuc-Hor and μ Tau (Gagné et al., 2020) because the rotation spread at 10 Myr is driven mostly by initial rotation rather than sculpting effects.

We show the rotation distribution of candidate members of MELANGE-4 with Quality 0 or 1 periods alongside other young populations in Figure 3.8. As expected, low-mass members are rotating slower than slightly older stars as they are still spinning up while contracting towards the main sequence. Similarly, the higher-mass members contain a mix of rapidly-rotating stars and those that have started to move to the slow-rotating sequence. The overall rotation distribution is consistent with a 20-40 Myr population.

3.4 Directly Imaged Planets

Along with the newly-identified planet host HD 109833 (discussed in Sections 3.5 & 3.6), three other candidate members of MELANGE-4 host four planetary-mass objects previously identified through direct-imaging surveys. These systems represent a non-trivial fraction of all the directly imaged planetary-mass companions (Currie et al., 2022), so a change in their age (and hence derived masses) could impact population-level statistics.

To update the masses of the directly imaged planets, we analyze the reported luminosity or absolute magnitude in the original papers and compare them to the weak-non-equilibrium ATMO2020 models of Phillips et al. (2020) using linear interpolation. We first verify that

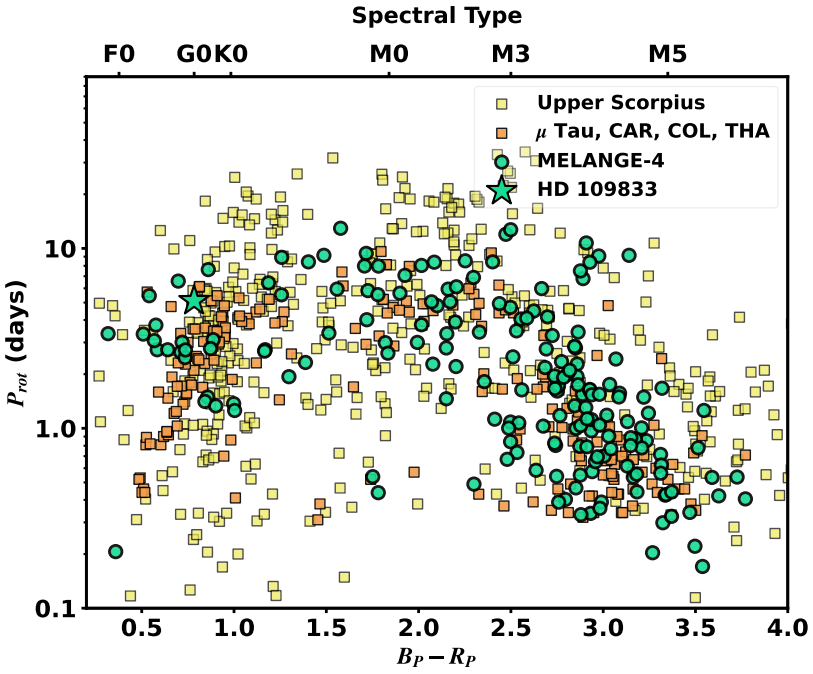

Figure 3.8 Rotation periods of candidate members of MELANGE-4 as a function of *Gaia* $B_P - R_P$ color. We compare the color-period sequence of candidate members to the younger ($\sim$ 10 Myr) population of Upper Scorpius (Rebull et al., 2018) and older (45–60 Myr) populations of Carina (CAR), Columba (COL), Tucana-Horologium (THA), and μ Tau (Gagné et al., 2020). As expected, the MELANGE-4 sequence shows more coherence than the sequence of the younger Upper Scorpius. The low-mass candidates rotate slower than those in the 45–60 Myr populations, indicating a younger population that will spin up as they contract onto the main sequence. The high-mass candidates are a mix of still rapidly-rotating stars and stars that have begun to spin down.

when using the originally asserted ages, we recover consistent masses, so any difference is primarily a result of the revised (older) age.

3.4.1 TYC 8998-760-1 (YSES 1)

TYC 8998-760-1 is a young K-dwarf type star with two directly imaged, wide companions from the Young Suns Exoplanet Survey (YSES) direct-imaging survey (Bohn et al., 2020a,b). The star has been classified as a $\simeq$ 16 Myr-old member of LCC (e.g., Pecaut & Mamajek, 2016). However, using our updated `BANYAN` Σ parameters we find that it is a high-probability

candidate member of MELANGE-4. The star's position, proper motions, and velocity are near the center of MELANGE-4, with a BANYAN Σ membership probability of 99.1%.

Assuming an age of 16.7 ± 1.4 Myr, Bohn et al. (2020a,b) measured masses of $14 \pm 3 M_{Jup}$ and $6 \pm 1 M_{Jup}$ for planets YSES-1 b and YSES-1 c, respectively. Using the age of MELANGE-4 (27 ± 3 Myr, see Section 3.3), we estimate masses of $21.8 \pm 3 M_{Jup}$, and $7.2 \pm 0.7 M_{Jup}$. As expected, the new masses are much larger than the earlier values, although still ($< 3\sigma$) consistent due to large uncertainties on the nearly vertical evolution of late-type pre-MS stars and brown dwarfs.

3.4.2 TYC 8984-2245-1 (YSES 2)

Like TYC 8998-760-1, TYC 8984-2245-1 is a young K-dwarf with a directly imaged companion observed by the YSES survey (Bohn et al., 2021). Several surveys of LCC have previously included TYC 8984-2245-1 as a member (e.g., Preibisch & Mamajek, 2008; Gagné et al., 2018). However, using the *Gaia* DR3 RV of 12.93 km s^{-1}, we find that it is a better match for MELANGE-4, with a kinematic membership probability of 94.8%.

Re-estimating the mass of YSES-2 b using the H and K magnitudes gives a new mass of $8.4 \pm 1.5 M_{Jup}$. Again, this is a higher mass but still consistent with the prior estimate of $6.3^{+1.3}_{-0.9} M_{Jup}$ (Bohn et al., 2021).

3.4.3 HD 95086

HD 95086 is an pre-MS star of spectral class A8, with both a directly imaged planet and an imaged debris disk (Rameau et al., 2013; Moór et al., 2013). De Zeeuw et al. (1999) and Rizzuto et al. (2011) both consider it to be a member of the LCC population, but Booth et al. (2021) argue that HD 95086 is instead a member of Carina, simultaneously proposing a younger (13 Myr) age for Carina.

The RV of HD 95086 has been measured multiple times by different sources; all of them strongly favor membership in MELANGE-4. Madsen et al. (2002) estimate an astrometric

RV of 10.1 ± 1.2 km s^{-1}, which gives a `BANYAN` Σ membership probability of 98.7% for MELANGE-4, a 1.3% probability of being a field star, and $< 1e-4$% for any of the LCC groups or Carina. Moór et al. (2013) measure $RV = 17 \pm 2$ km s^{-1}, with which the probability of membership in MELANGE-4 increases to 99.1%, with a probability of 0.66% for Carina and $< 1e-4$% for all of the LCC groups. The *Gaia* DR3 velocity is similar, $RV = 18.04 \pm 0.16$ km s^{-1}, which gives a membership probability of 98.9% for MELANGE-4, 0.77% for membership in Carina, and 0.30% for field.

Using the previously assumed age of 17 ± 2 Myr, de Rosa et al. (2016) derive a mass of $4.4 \pm 0.8 M_{Jup}$, placing HD 95086 b among the least massive planets yet detected with direct imaging. Using the K-band luminosity and the new, older age, we estimate a higher mass of $7.2 \pm 0.7 M_{Jup}$. This shows more tension with the discovery value than for the other three planets, but the new value is still marginally consistent with the original (2.6σ).

3.5 Parameters of TOI-1097

We summarize constraints on the candidate-planet host star in Table 3.5, the details of which we provide in this section.

Table 3.5. Properties of the host star HD 109833.

Parameter	Value	Source
	Identifiers	
HD	109833	
HIP	61723	*Hipparcos*
TOI	1097	Guerrero et al. (2021)
Gaia	5838450865699668736	*Gaia* DR3
TIC	360630575	Stassun et al. (2018)
2MASS	J12390642-7434263	2MASS
	Astrometry	
α	189.775832	*Gaia* DR3
δ	-74.574021	*Gaia* DR3
μ_α (mas yr^{-1})	-50.489 ± 0.012	*Gaia* DR3
μ_δ (mas yr^{-1})	-6.764 ± 0.014	*Gaia* DR3
π (mas)	12.5686 ± 0.0118	*Gaia* DR3
	Photometry	
G_{Gaia} (mag)	9.145 ± 0.003	*Gaia* DR3
BP_{Gaia} (mag)	9.451 ± 0.006	*Gaia* DR3
RP_{Gaia} (mag)	8.668 ± 0.004	*Gaia* DR3
B_T (mag)	10.082 ± 0.027	Tycho-2
V_T (mag)	9.380 ± 0.020	Tycho-2
J (mag)	8.144 ± 0.023	2MASS
H (mag)	7.890 ± 0.038	2MASS
Ks (mag)	7.820 ± 0.026	2MASS
W1 (mag)	7.772 ± 0.028	ALLWISE
W2 (mag)	7.814 ± 0.020	ALLWISE
W3 (mag)	7.787 ± 0.018	ALLWISE
	Physical Properties	
$P_{\rm rot}$ (days)	5.111 ± 0.51	This work
$v \sin i_*$(km s^{-1})	10.5 ± 0.2	This work
i_* ($^\circ$)	> 84	This work
$F_{\rm bol}$ (erg cm^{-2} s^{-1})	$(6 \pm 0.4) \times 10^{-9}$	This work
$T_{\rm eff}$ (K)	5881 ± 50	This work
log g (dex)	4.45 ± 0.10	This work
$M_\star$ ($M_\odot$)	1.08 ± 0.05	This work
$R_\star$ ($R_\odot$)	1.00 ± 0.04	This work
$L_\star$ ($L_\odot$)	1.18 ± 0.08	This work
[M/H]	-0.07 ± 0.08	This work
$\rho_\star$ ($\rho_\odot$)	1.08 ± 0.17	This work
Age (Myr)	27 ± 3	This work

3.5.1 Fit to the spectral energy distribution

To determine $T_{\rm eff}$, R_*, and L_* of HD 109833, we fit the spectral energy distribution (SED) following the methodology from Mann et al. (2016a). To summarize, we compare the observed photometry to a grid of optical and NIR spectra of nearby unreddened stars. Most spectra are drawn from Rayner et al. (2009), supplemented by Hubble's Next Generation Spectral Library (NGSL; Heap & Lindler, 2016). To fill in gaps in the spectra, we use BT-SETTL CIFIST atmospheric models (Baraffe et al., 2015), fitting to the template spectrum as outlined in Gaidos & Mann (2014). This also provides an estimate of $T_{\rm eff}$. We integrate the resulting full SED to determine the bolometric flux ($F_{\rm bol}$), which combined with the *Gaia* DR3 parallax, gives us the total luminosity (L_*). We then use the Stefan-Boltzmann relation to calculate R_* from $T_{\rm eff}$ and L_*.

For our fit, we use photometry from Tycho-2 (Høg et al., 2000), the Two Micron All-Sky Survey (2MASS; Skrutskie et al., 2006), the Wide-field Infrared Survey Explorer (WISE; Wright et al., 2010), and *Gaia* DR3 (Gaia Collaboration et al., 2021). We exclude $W3$ and $W4$ photometry in our fit because the star's young age allows the possibility of a cool debris disk. To account for variability in the star, we add 0.02 mags in quadrature to the errors of all optical photometry. In total, the fit includes six free parameters: the choice of template, A_V, three parameters that describe the atmospheric model selection ($\log\ g$, $T_{\rm eff}$, and $[M/H]$), and a scale factor between the model and the photometry (S).

The resulting fit gives $T_{\rm eff}$=5950 $\pm$ 90 K, $F_{\rm bol}$=(6.0 $\pm$ 0.4) $\times$ 10^{-9} (erg cm^{-2} s^{-1}), L_* = 1.18 $\pm$ 0.08$L_\odot$, R_* = 1.00 $\pm$ 0.04$R_\odot$, and a spectral type of G1V– G3V. The best-fit model predicts a $W3$ that is lower than the observed value by 10–20%, which suggests the presence of a debris disk. However, the excess is below significance for some templates, and no significant excess is seen in the less precise $W4$ point.

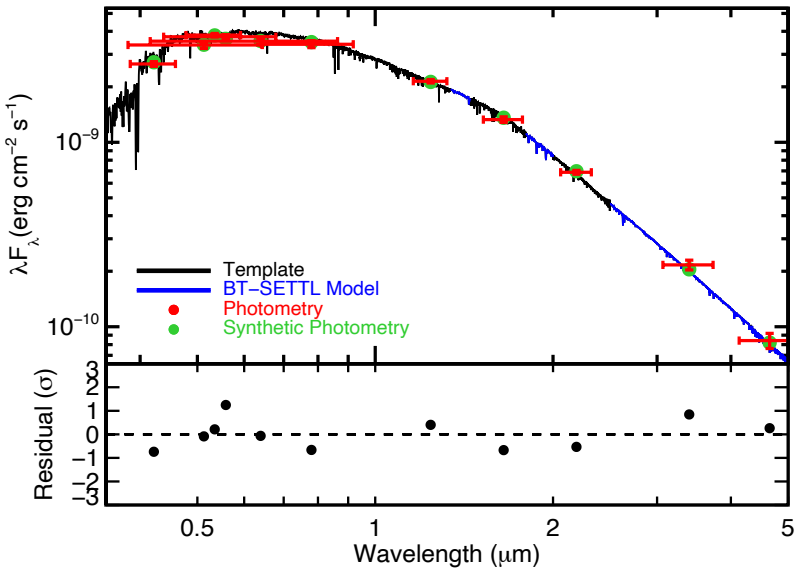

Figure 3.9 Observed HD 109833 photometry compared to the best-fit template spectrum (G1V; black) and synthetic photometry (red). Errors on observed photometry are shown as vertical errors, while horizontal errors indicate the approximate width of the filter. BT-SETTL models (blue) were used to fill in regions of high telluric absorption or beyond the template range. The bottom panel shows the photometric residual in units of standard deviations.

3.5.2 Fit to the high-resolution spectra

In addition to the SED fit described above, we derive the atmospheric parameters from both the CHIRON and HARPS spectra. These served as an independent test of $T_{\rm eff}$, while also constraining the metallicity, log g, and rotational broadening ($v \sin i_*$).

We derive spectral parameters ($T_{\rm eff}$, $\log g$, $v \sin i_*$ and [M/H]) from the CHIRON spectra of HD 109833 using the Spectral Parameter Classification (SPC) tool (Buchhave et al., 2012). SPC cross-correlates the observed spectrum against a grid of Kurucz atmospheric models (Kurucz, 1993). Four parameters are allowed to vary: $T_{\rm eff}$, $log\ g$, bulk metallicity ([M/H]), and $v \sin i_*$. We run each spectrum separately, then combine the results, yielding $T_{\rm eff}$= 5881 ± 45 K, log $g = 4.445 \pm 0.041$, [M/H]= -0.068 ± 0.053, and $v \sin i_\star = 10.5 \pm 0.2$ km s^{-1}. The assigned errors reflect the scatter between spectra, and do not include systematic errors. Based on comparison with benchmark stars (e.g., asteroseismic targets), we adopt error floors

of 50 K, 0.1 dex in log g, and 0.08 dex in [M/H]. Even with the error floors, the resulting $T_{\rm eff}$ estimate is more precise than those from the fitted SED.

We separately derive spectral parameters from the HARPS spectra using the methodology described by Sousa (2014) and Santos et al. (2013). We first measure the equivalent widths (EW) of 224 FeI and 35 FeII lines using the ARES v2 code[11] (Sousa et al., 2015). Then we use these EWs together with a grid of Kurucz model atmospheres (Kurucz, 1993) and the radiative transfer code MOOG (Sneden, 1973) to determine the parameters under the assumption of ionization and excitation equilibrium. The abundances of Mg and Si are also derived using the same tools and models as detailed by Adibekyan et al. (2012, 2015). Although the EWs of the spectral lines are automatically measured with ARES, we visually inspected each of the EWs measurements as only three lines are available for the Mg abundance determination. This analysis gives $T_{\rm eff}$= 5975 ± 70 K, log $g = 4.58 \pm 0.11$, [Fe/H] $= 0.08 \pm 0.05$, [Mg/H] $= 0.02 \pm 0.06$, and [Si/H] $= 0.05 \pm 0.05$.

The projected rotational velocity ($v \sin i_*$= 9.9 ± 0.8 km s^{-1}) is derived from the HARPS spectra by performing spectral synthesis with MOOG on 36 isolated iron lines and by fixing all the stellar parameters, macroturbulent velocity, and limb-darkening coefficient (Costa Silva et al., 2020). The limb-darkening coefficient (0.58) is determined using the stellar parameters as described by Espinoza & Jordán (2015) assuming a linear limb darkening law. The macroturbulent velocity (3.6km s^{-1}) is determined using the temperature and gravity-dependent empirical formula from Doyle et al. (2014).

Despite using different methods and data, the two sets of results above are all consistent within 2σ, and both are consistent with our SED analysis. We use the CHIRON/SPC fit for $T_{\rm eff}$ and $v \sin i_*$, and the abundances from the HARPS/MOOG analysis. Using any set, or the average of the three, does not significantly change any results or conclusions of this chapter.

[11] `http://www.astro.up.pt/~sousasag/ares`

3.5.3 Mass from stellar isochrones

To determine the stellar mass (M_*) we compare the observed photometry (from *Gaia* G, B_P, R_P; 2MASS J, H, K; and Tycho B_T, V_T) to predictions from the DSEP magnetic models (Feiden, 2016). The DSEP magnetic model covers ages from 1 Myr to 10 Gyr and masses between 0.09 $M_\odot$ and 2.45 $M_\odot$. To explore systematics between models, we also fit using the PARSEC (v1.2S) models (Bressan et al., 2012). We compare the models using an MCMC framework with `emcee`, simultaneously fitting for four parameters: age, M_*, A_V, and a factor describing the underestimation of the errors on the measured photometry (f). For both grids, we assume Solar metallicity.

To alleviate the computational cost of bilinearly interpolating the model grid at every step, we pre-interpolate the grid using the `isochrones` package (Morton, 2015) to give it tighter spacing in age and mass (0.1 Myr and 0.01 $M_\odot$) than expected errors. Grid resampling also lets us enforce uniform sampling in age. During each sampling step, the procedure is as follows: first, we employ a hybrid interpolation method, which finds the nearest neighbor in age, then linearly interpolate in mass, to extract predicted photometry and stellar parameters (such as $T_{\rm eff}$ and R_*). Second, the predicted photometry is corrected according to the given A_V value, using a combination of `synphot` (Lim, 2020) and the extinction model from Cardelli et al. (1989). Lastly, we compare the corrected model photometry to the measured photometry in a Bayesian maximum-likelihood framework.

We place Gaussian priors of 27 ± 3 Myr on age and 5881 ± 50 K on $T_{\rm eff}$, following our analysis of the spectrum. All other fitted parameters evolve under uniform priors. The DSEP magnetic model produces age $= 34.5 \pm 1.7$ Myr and $M_* = 1.13 \pm 0.02$ $M_\odot$, while PARSEC gives age $= 30.9 \pm 0.8$ Myr and $M_* = 1.03 \pm 0.02$ $M_\odot$. The errors are statistical only, as evident by the $\simeq 3\sigma$ disagreement on M_* (0.10 ± 0.03 $M_\odot$) between the two methods. We adopt $M_* = 1.08 \pm 0.05$ $M_\odot$, which encompasses both values and more accurately reflects the systematic limits of the models (Tayar et al., 2022).

3.5.4 Stellar Inclination

We use the combination of $v \sin i_*$, $P_{\rm rot}$, and R_* to estimate the stellar inclination (i_*). Since the transiting planets are nearly edge-on ($i > 85°$; Section 3.6) this measures the alignment between the stellar spin and planetary orbit axes. Simplistically, the equatorial velocity (V) in $v \sin i_*$ can be derived using $V = 2\pi R_*/P_{\rm rot}$. In practice, however, this calculation requires additional corrections due to the effects of sky-projection and measurement uncertainties, which could cause the appearance of $v \sin i_* > V$. We followed the formalism from (Masuda & Winn, 2020). Using either $v \sin i_*$ determined in Section 3.5.2 gave an inclination consistent with edge-on. The CHIRON $v \sin i_*$ gave a limit of $i_* > 84°$ at 95% confidence, while the HARPS $v \sin i_*$ yielded $i_* > 66°$.

3.6 Parameters of TOI-1097 b and TOI-1097 c

3.6.1 Detection of the planetary signals

The first planet signal, TOI-1097.01, was originally detected from the joint search of sectors 11 and 12 as part of the Quick-Look Pipeline (QLP) search (Huang et al., 2020). The candidate passed initial vetting and triggered an alert on 2021 Oct 29.

To confirm the detection and search for additional planets, we use the Notch and LoCoR pipelines described by Rizzuto et al. (2017)[12]. To briefly summarize, the Notch filter fits a window of the light curve as a combination of an outlier-robust second-order polynomial and a trapezoidal notch. The window is shifted along the light curve until the variability is detrended (flattened) while preserving the planet signal. At each data point, Notch calculates the improvement from adding the trapezoidal notch based on the change in the Bayesian Information Criterion (BIC) compared to modeling just a polynomial.

After running Notch, we perform a box-least-squares search on the BIC values and recovered both the initial 9.2 day planet candidate from *TESS* and an additional signal at

[12]`https://github.com/arizzuto/Notch_and_LOCoR`

either 13.9 or 41 days (it was initially ambiguous). Additional short-cadence data from Sectors 38 and 39 made it clear that the shorter 13.9 day period was the correct one. This candidate was later recovered by a *TESS* Science Processing Operations Center (SPOC) pipeline joint search of sectors 38 and 39 (Jenkins, 2002b; Jenkins et al., 2010, 2020) and designated TOI-1097.02 on 2022 Mar 24 by the TESS Science Office.

There were no other significant detections from our Notch search, other than those near aliases of the planets and/or rotation period. The BIC is sensitive to single-transit detections (Rizzuto et al., 2020), but we did not identify any such signals that survived visual inspection.

3.6.2 MCMC fit of light curves

To determine the planet parameters, we compare a transit model to the *TESS* photometry using the `MISTTBORN` (MCMC Interface for Synthesis of Transits, Tomography, Binaries, and Others of a Relevant Nature) code[13]. `MISTTBORN` uses `BATMAN` (Kreidberg, 2015) to generate model light curves, `celerite` (Foreman-Mackey et al., 2017) to model the stellar variability, and `emcee` (Foreman-Mackey et al., 2013) to explore the parameter space. More details on the code are provided in Mann et al. (2016b) and Johnson et al. (2018).

The standard implementation of `MISTTBORN` fits four parameters for each transiting planet: time of periastron (T_0), orbital period of the planet (P), planet-to-star radius ratio ($R_p/R_\star$), and impact parameter (b). Three additional parameters specific to the host star are also fit: stellar density ($\rho_\star$) and two limb-darkening parameters (q_1, q_2) using the triangular sampling prescription from Kipping (2013).

Stellar variability from the star was far stronger than the transit signal over all *TESS* data. We fit the variations using the Gaussian Process (GP) feature within `MISTTBORN`. We initially adopted the GP kernel based on a mixture of two simple harmonic oscillators but found that the parameters associated with the second oscillator were unconstrained and never fully converged. Instead, we adopt a single-term simple harmonic oscillator, based on

[13] `https://github.com/captain-exoplanet/misttborn`

the model used by Foreman-Mackey et al. (2017), which includes three GP terms: the period ($\ln(P_{GP})$), amplitude ($\ln \mathrm{Amp}$), and the decay timescale for the variability (quality factor, $\ln Q$).

Although eccentricities of young planets are expected to be near zero due to gravitational interactions and drag from the circumstellar disk (Tanaka & Ward, 2004), this young regime has few observational constraints. So, we run two fits, one with eccentricity locked at zero and a uniform prior on $\rho_\star$, and a second fitting two parameters describing eccentricity and argument of periastron ($\sqrt{e} * \cos(\omega)$, and $\sqrt{e} * \sin(\omega)$) with a uniform prior and assuming a Gaussian prior for $\rho_\star$ drawn from Section 3.5.

We apply Gaussian priors on the limb-darkening coefficients based on the values from the `LDTK` toolkit (Parviainen & Aigrain, 2015), with errors accounting for the difference between these two estimates (which differ by 0.04–0.08).

After an initial fit, we found a few walkers wandered off the transit signal, adjusting the GP signal to partially fit the transit. To prevent this, we place weak Gaussian priors on T_0, P, and $\ln(P_{GP})$ around the initially estimated values from a least-squares fit, and with widths of 0.1 days, 0.1 days, and 0.1 dex (1 day), respectively. The width of these priors was much larger than the final uncertainties and had a negligible effect on the result (other than preventing the wandering walkers). All other parameters evolve under uniform priors with physically motivated limits.

For the first fit (e locked at 0), we run the MCMC using 50 walkers for 100,000 steps including a burn-in of 20,000 steps. This setup is sufficient for convergence based on the autocorrelation time. For the second fit, which has a lower acceptance fraction, we use 200 walkers and 100,000 steps (the same burn-in).

Both of the fits were broadly consistent, producing consistent q_1, q_2, and GP fit for the star, T_0, P, and R_P/R_* for both planets, and impact parameter for the outer planet. The impact parameter of the inner planet is higher when allowing non-zero eccentricities, but consistent within the uncertainties. The GP fit found a stellar rotation period of $P_{GP} =$

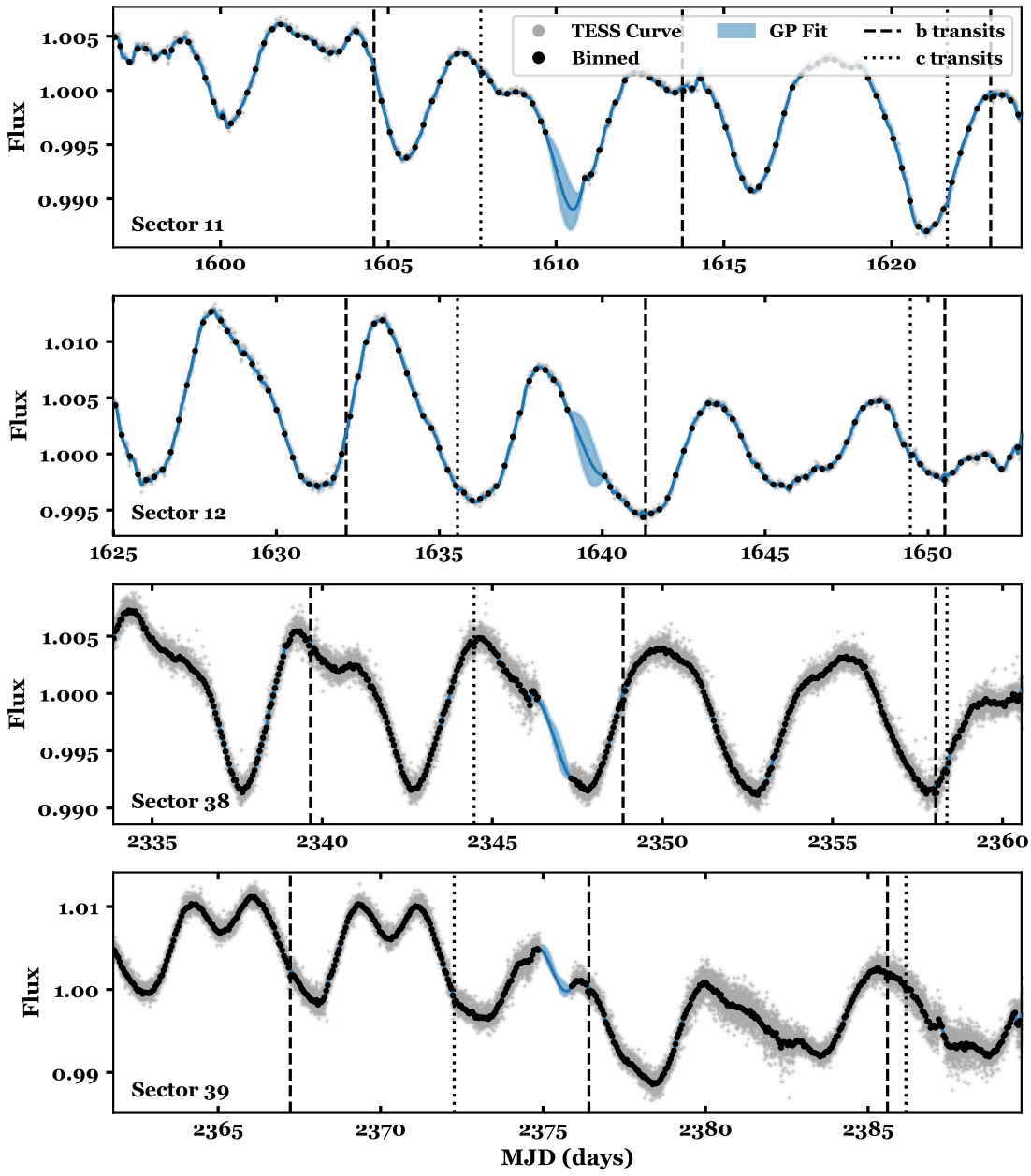

Figure 3.10 *TESS* light curves of HD 109833 for Sectors (from top to bottom) 11, 12, 38, and 39. Data for each sector is shown as gray dots and binned values as black dots. The blue line indicates the model GP fit to the data with uncertainties (shaded region). The times of the transits are marked with dashed and dotted vertical lines for planets b and c, respectively.

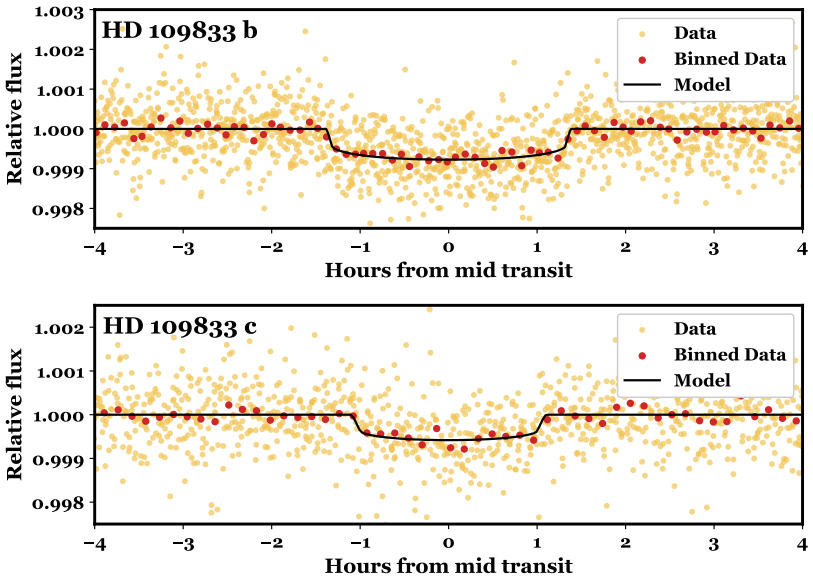

Figure 3.11 Phase-folded transits of HD 109833 b and c. The data are shown in yellow, with the 20 s cadence data from Sectors 38 and 39 binned to 2 m. Red points show all data binned together, and the black line shows the `batman` model using the results from the $e = 0$ `MISTTBORN` run.

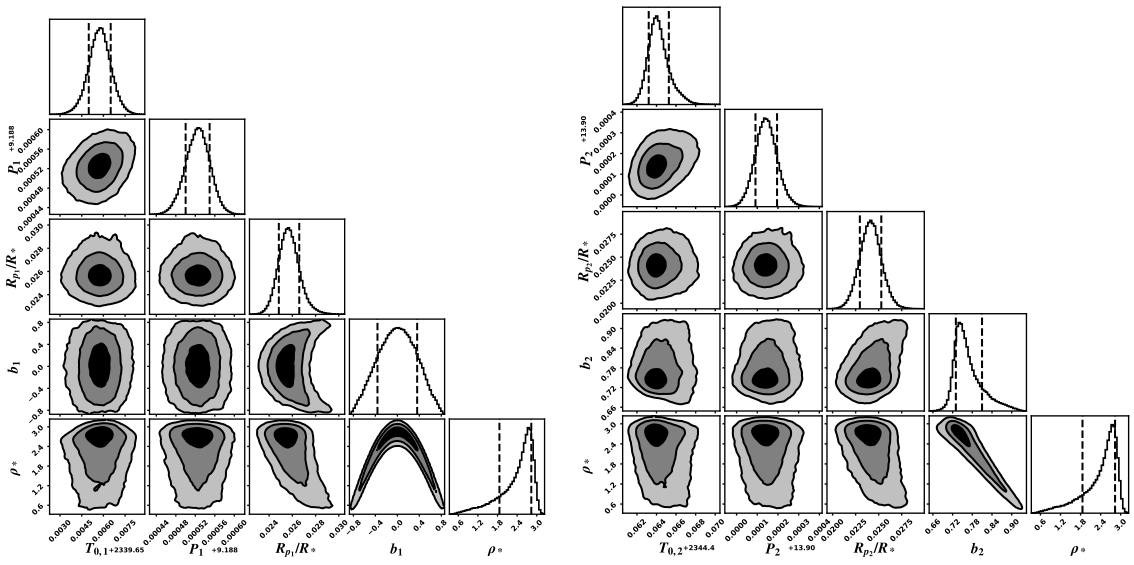

Figure 3.12 Corner plots of the `MISTTBORN` results for TOI-1097 b (left) and TOI-1097 c (right), with eccentricity locked to $e = 0$. Posterior distributions are shown as 2-dimensional contour plots, with levels corresponding to 1, 2, and 3σ, and as histograms with the $16th$ and $84th$ percentiles marked with dashed lines. Distributions are mostly Gaussian, with the exception of ρ_*, which has a long tail towards a less-massive stellar host. The distribution of ρ_* is shown on both plots, but only a single value is explored in the fit. .

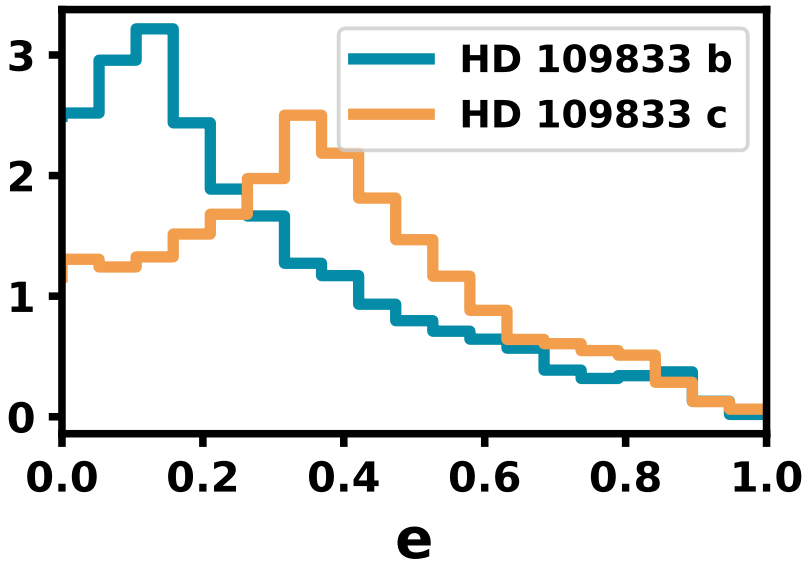

Figure 3.13 `MISTBORN` posterior eccentricity distribution for HD 109833 b (blue) and c (orange). A uniform prior on e and Gaussian prior on ρ_*, based on our stellar parameters fit, were used. Both planets are consistent with zero eccentricity.

5.64 ± 1.08 days, consistent with the rotation period found using a Lomb-Scargle periodigram analysis, $P_{rot} = 5.11 \pm 0.51$ days (see Section 3.1.2).

The results are shown as corner plots in Figure 3.12. The eccentric fit cannot rule out a zero eccentricity for either planet but does suggest a potentially eccentric orbit, especially for the outer planet, which has a best-fit eccentricity $e_c = 0.3^{+0.21}_{-0.19}$. The posterior distribution of eccentricity for each planet is shown in Figure 3.13.

3.6.3 Statistical Validation

For our false positive analysis, we first calculate the magnitude limit (Δm) of a potential blended source (bound or background) that could reproduce the transit signal, using the source brightness constraints described by Seager & Mallén-Ornelas (2003) and Vanderburg et al. (2019). This depends on the ingress or egress duration compared to the transit duration and reflects the true radius ratio, independent of contaminating flux:

Table 3.6. Parameters of HD 109833 b and c

	HD 109833	
Parameter	e=0	e float (preferred)
	Measured Parameters	
$\rho_\star$ ($\rho_\odot$)	$2.544^{+0.287}_{-0.714}$	$1.1027^{+0.1359}_{-0.1415}$
$q_{1,1}$	$0.303^{+0.101}_{-0.094}$	$0.321^{+0.141}_{-0.115}$
$q_{2,1}$	$0.364^{+0.077}_{-0.084}$	$0.325^{+0.109}_{-0.142}$
$\ln(P_{GP})$	$1.730^{+0.083}_{-0.081}$	$1.729^{+0.092}_{-0.081}$
$\ln(Amp)$	$-9.525^{+0.177}_{-0.164}$	$-9.531^{+0.183}_{-0.170}$
$\ln(Q)$	$0.618^{+0.035}_{-0.026}$	$0.618^{+0.036}_{-0.028}$
	HD 109833 b	
Parameter	e=0	e float (preferred)
	Measured Parameters	
T_0 (BJD-2454833)	$1604.57376^{+0.00074}_{-0.00076}$	$1604.57374^{+0.00091}_{-0.00097}$
P (days)	$9.188525 \pm 2.5 \times 10^{-5}$	$9.188526 \pm 2.6 \times 10^{-5}$
$R_P/R_\star$	$0.02569^{+0.00091}_{-0.00085}$	$0.0265^{+0.0014}_{-0.0012}$
b	$0.25^{+0.25}_{-0.18}$	$0.61^{+0.15}_{-0.33}$
$\sqrt{e}\sin\omega$	–	$0.02^{+0.23}_{-0.25}$
$\sqrt{e}\cos\omega$	–	$-0.03^{+0.51}_{-0.46}$
	Derived Parameters	
$a/R_\star$	$25.2^{+0.9}_{-3.0}$	$19.9^{+1.9}_{-2.1}$
i (°)	$89.4^{+0.4}_{-0.7}$	$88.13^{+1.0}_{-0.55}$
e	–	$0.18^{+0.24}_{-0.12}$
R_P ($R_\oplus$)	$2.802^{+0.099}_{-0.093}$	$2.888^{+0.152}_{-0.127}$
	HD 109833 c	
Parameter	e=0	e float (preferred)
	Measured Parameters	
T_0 (BJD-2454833)	$1607.75659^{+0.0012}_{-0.00092}$	$1607.7567^{+0.0015}_{-0.0011}$
P (days)	$13.900142 \pm 5.3 \times 10^{-5}$	$13.900148 \pm 5.7 \times 10^{-5}$
$R_P/R_\star$	$0.0241^{+0.0012}_{-0.0012}$	$0.0237^{+0.0018}_{-0.0016}$
b	$0.757^{+0.055}_{-0.027}$	$0.73^{+0.14}_{-0.32}$
$\sqrt{e}\sin\omega$	–	$0.2^{+0.24}_{-0.31}$
$\sqrt{e}\cos\omega$	–	$-0.0^{+0.54}_{-0.56}$
	Derived Parameters	
$a/R_\star$	$33.2^{+1.2}_{-3.5}$	$29.4^{+4.5}_{-4.3}$
i (°)	$88.696^{+0.085}_{-0.3}$	$88.24^{+0.73}_{-0.34}$
e	–	$0.3^{+0.21}_{-0.19}$
R_P ($R_\oplus$)	$2.63^{+0.128}_{-0.125}$	$2.59^{+0.196}_{-0.175}$

Note. — Results of the `MISTBORN` MCMC fitting of the planet transits.

$$\Delta m \leq 2.5 \log_{10}(\frac{T_{12}^2}{T_{13}^2 \delta})$$

Here, δ is the transit depth, T_{12} is the ingress/egress duration and T_{13} is the time between the first and third contact. We calculate Δm for the posterior samples for our floating eccentricity transit fit and take the 99.7% confidence limit. We find $\Delta m < 3.5$ and < 5.3 for HD 109833 b and c, respectively.

Based on these magnitude limits, only two stars detected by *Gaia* (including HD 109833) could reproduce the transits of HD 109833 b, and three stars could reproduce HD 109833 c (see Figure 3.14). By selectively resizing the aperture, we rule out all stars other than HD 109833 as the source of the planetary signals. We also check this using the `tpfplotter` tool from Aller et al. (2020), and find four faint stars within the aperture, all with $\Delta T > 5$.

Separately, the centroid offsets from the SPOC data validation (Twicken et al., 2018; Li et al., 2019) for Sectors 38-39 exclude all TICv8.2 objects capable of producing the observed transit depths other than the target star. As with the transit duration and depth constraints above, this confirms that the only remaining false-positive scenarios involve objects unresolved with HD 109833.

To handle unresolved sources, we use a combination of Multi Observational Limits on Unseen Stellar Companions (MOLUSC; Wood et al., 2021) and a tool for vetting and validating TESS Objects of Interest (Triceratops; Giacalone et al., 2021). `MOLUSC` provides limits on the range of possible companions allowed by the existing data, while `triceratops` combines the companion limits with information about the light curve to compute probabilities of given false-positive (FP) scenarios.

`MOLUSC` generates simulated companions and compares them to RV measurements, contrast imaging, and *Gaia* RUWE and imaging constraints. We test two different scenarios, one of a transiting stellar companion, for which the cosine of stellar inclination, $cos(i)$, is

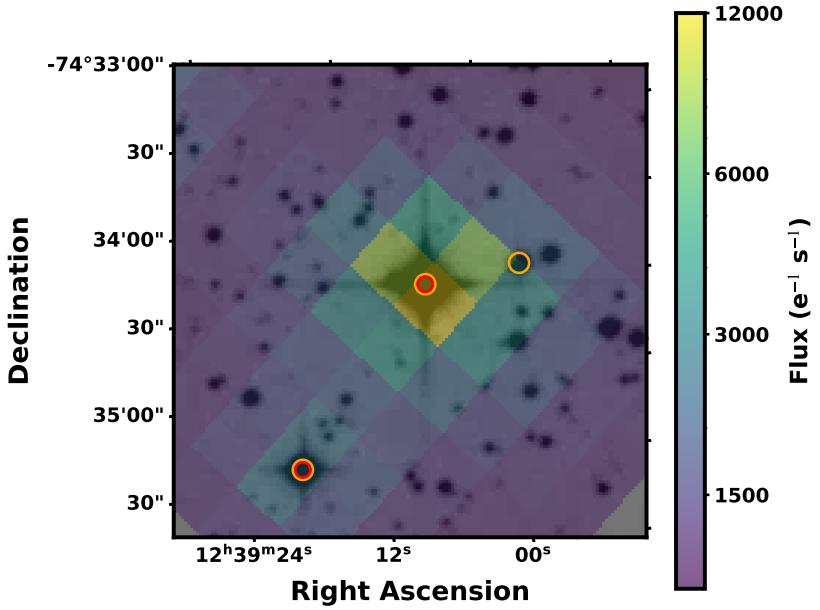

Figure 3.14 *TESS* Sector 38 image of HD 109833 colored by flux (see colorbar) overplotted on a DSS image (grayscale). Red circles indicate the two stars that could reproduce the transit signal for planet b, while orange indicates those that could reproduce c. The bright central star is HD 109833.

locked to only transiting companions, and one of any stellar companion, for which $cos(i)$ was drawn from a uniform distribution. In the second scenario, we assume the transits are caused by planetary-mass objects, but there is an additional stellar companion in the system. For both scenarios we generate 5,000,000 companions, with orbital parameters drawn from realistic binary distributions (see Wood et al. (2021) for details). Across both scenarios, 91.3% of generated companions were ruled out. In the transiting scenario, we found 3σ detection limits of $\sim$ 0.4–0.7M_{Jup} at periods of 9–13 days. This alone rules out an eclipsing stellar companion (orbiting HD 109833) as the cause of the transit signals. As the planets are not detected in any of the included datasets, the mass limits do not include the planets. The non-transiting companion scenario, while allowing the possibility of a stellar companion at moderate periods, rules out nearly all companions with $M_{comp} > 0.6$ $M_\odot$ or $P < 100$ days.

To calculate the probability that each signal is due to a planet, we run `triceratops` using all four sectors of *TESS* data and the output binaries generated from `MOLUSC`. Including

the `MOLUSC` output effectively limited the possible FP scenarios to those consistent with the observational limits. Of the 18 different scenarios considered by Giacalone et al. (2021), three are considered "true positives", i.e., the transiting planet, unresolved binary with a transiting planet around the primary, and unresolved background star with a transiting planet around the primary. By default, `triceratops` considers signals that come from a bound companion as false positives, even if the signal is still a transiting planet. We consider cases including a planet and a bound companion as true positives, as the signal was still from a young planet even if the radii are likely significantly underestimated.

For each planet we run `triceratops` 20 times and find the mean and standard deviation of the FP pronability (FPP). For HD 109833 b, we find $FPP < 0.0003(0.03\%)$, with an additional $\simeq 1\%$ probability that the planet orbits a bound companion. If HD 109833 b is orbiting a secondary companion with the predicted mass of $\sim 0.8 M_{sun}$, it would still have a radius consistent with a planet.

For HD 109833 c, `triceratops` yielded a higher FPP of $9.2 \pm 2.5\%$. Multi-planet systems are less likely to be false positives (e.g., Lissauer et al., 2012). Guerrero et al. (2021) recalculated this "multiplicity boost" for TOIs, i.e., the multiplicative factor that reflects the *a priori* probability that a candidate in a multi-transiting system is a true positive. They estimate this to be $\simeq$50 for planets $R_p < 6 R_\oplus$. Even the more conservative factor of 20 for all TOIs is still sufficient to bring HD 109833 c below the 1% required for validation.

CHAPTER 4: THE CARINA-COLUMBA COMPLEX

The Carina association is a nearby young association. Discovered by Torres et al. (2008), it was originally considered part of the GAYA complex, which included two additional nearby associations, Tucana-Horologium and Columba. However, the relationship between these groups is uncertain. Later research found that Carina and Columba form a complex, but are independent from Tucana-Horologium. Gagné et al. (2021) used expanded kinematic information from *Gaia* to search for dispersed connections between populations, finding that Carina and Columba are connected through the Theia 92 and 113 groups (Kounkel et al., 2019) to Platais 8 (Platais et al., 1998).

The relationships between these groups is further muddied by uncertainty in their ages. The three groups originally thought to form the GAYA complex were estimated to be about 40 Myr old. The age of Tucana-Horologium, the largest and best studied of the three, was confirmed to be 40 Myr by Kraus et al. (2014). However, the ages of Carina and Columba are less certain. The age of Carina has been measured several times using a variety of membership lists and methods, resulting in estimates of 13 Myr (isochrone, Booth et al., 2021), $\sim$ 21 Myr (lithium sequence, Schneider et al., 2019), $>$ 28 Myr (kinematic, Miret-Roig et al., 2018), and 45^{+11}_{-7} Myr (isochrone, Bell et al., 2015). This range covers a nearly 400% variation.

A tighter age constraint on the Carina association will help to determine the relationship between the associations, but it can also provide constraints on the formation and evolution of planets. Members of Carina include debris (Moór et al., 2016) and protoplanetary disks Silverberg et al. (2016); Murphy et al. (2018), dippers (Gaidos et al., 2022), and have been suggested as an origin of the interstellar object Oumuamua (Hsieh et al., 2021). As one of

the closest known stellar associations, with a mean distance of 75 pc, Carina also provides a useful observational target.

In this chapter we apply the Lithium Depletion Boundary (LDB) method, in combination with a Gaussian Mixture Model isochrone fit and a comparison of the Li sequence to similar benchmark associations, to measure the age of the Carina association. Li measurements of two of the potential related associations, Theia 92 and Theia 113, are used to check if their ages are similar to that of Carina.

In Section 4.1 we describe our selection of members of Carina, Theia 92, and Theia 113. Our observational program is described in Section 4.2, and in Section 4.3 we determine the age of the association.

4.1 Membership Selection

4.1.1 Carina

To select the members of Carina we use the `BANYAN` Σ Bayesian tool for determining membership probabilities. `BANYAN` Σ uses kinematic models of nearby young associations to calculate the probability of a given star's membership within each association or the field. We use the kinematic models defined by Gagné et al. (2018) for most of the associations, but due to the proximity of Carina to Lower-Centaurus Crux (LCC), and MELANGE-4 (Wood et al., 2023), we use an updated model for those groups. The new model of LCC, incorporating its sub-populations, and the model of MELANGE-4 are described by Wood et al. (2023).

To construct the input sample for `BANYAN` Σ, we select from *Gaia* DR3 all stars within 100 pc of HD 49855, a high-probability member of Carina (Gagné et al., 2018). This sample comprised 542, 642 stars. We used this selected sample rather than the full *Gaia* DR3 200 pc sample to decrease the computation time and memory demands from the `BANYAN` Σ run, and to ensure that we included all stars near the Carina association. We used the *Gaia* DR3 RA, Dec, parallax, proper motions, and when available, radial velocity.

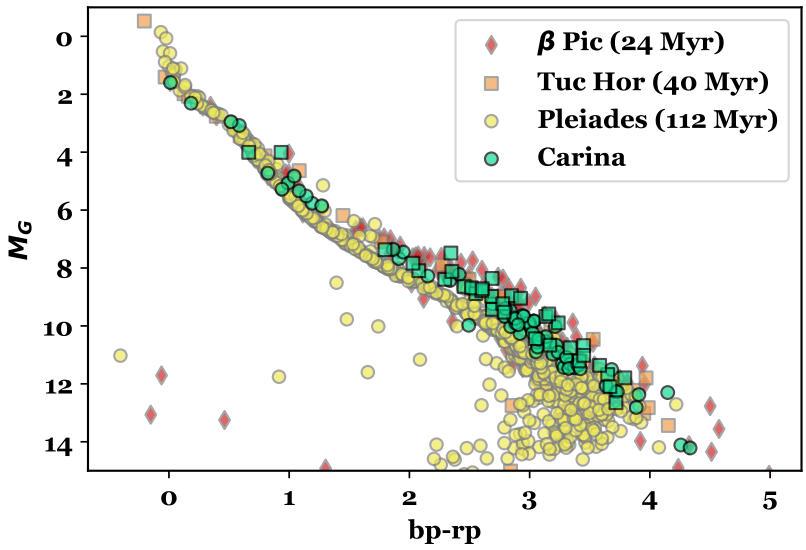

Figure 4.1 CMD of Carina members, overplotted with members of three benchmark associations, β Pictoris (21 Myr), Tuc-Hor (40Myr), and Pleiades (115 Myr). Membership lists for benchmark associations are generated using `BANYAN` Σ with the same parameters as described in Section 4.1. Only high probability members ($P_{BANYAN} > 95\%$) with $RUWE < 1.2$ are shown for benchmark associations.

From the results of `BANYAN` Σ, we take stars which have membership probability $P > 50\%$ and for which Carina is the best hypothesis (BESTHYP = CAR), yielding 129 candidate members.

As `BANYAN` Σ only uses kinematic indicators of membership in determining the probability, it is possible that older co-moving interlopers are included in this sample. To remove them we use the empirical definition of the Main-Sequence (MS) given by Pecaut et al. (2012). We remove candidates which have $Bp - Rp > 1$, $G - Rp > 0.5$, and are fainter than the MS.

We also remove potential binaries, as their inclusion could bias the measurement of age. We do so using the *Gaia* Renormalized Unit Weight Error (RUWE), a measure of the astrometric model goodness-of-fit. A high RUWE is indicative of binarity (Sullivan & Kraus, 2021; Belokurov et al., 2020), so we remove those with $RUWE > 1.2$ from the membership list. These cuts leave a membership list of 99 probable Carina members, shown in Figure 4.1.

4.1.2 Theia Groups

None of the Theia groups have kinematic definitions in `BANYAN` Σ, so their memberships were obtained from Kounkel & Covey (2019). This membership list may miss some members and include some interlopers (see Zucker et al., 2022a), but we deem it sufficiently clean for our purposes (Barber & Mann, 2023). Theia 113 has 183 candidate members, for which we obtain *Gaia* kinematic and photometric information and 2MASS magntiudes (see Section 4.2.3).

4.2 Observations

4.2.1 SOAR/Goodman

To obtain the medium-resolution optical spectra necessary for measuring the Li 6708 Å line in low-mass association members, we use the Goodman High Throughput Spectrograph, observing a total of 19 candidate members of Carina. Observations were taken under mostly photometric conditions over five nights from 2020 Feb 6 through 2020 Feb 20.

These 19 stars were selected from the sample of candidate association members to map the LDB. We use an age estimate of 45 Myr (Bell et al., 2015) to predict the magnitude of the LDB. Comparing this age to BHAC 15 stellar evolutionary models (Baraffe et al., 2015), we calculate the expected 2MASS K_S magnitude of 99% Li depletion. Stars with $\Delta K_S < 1$ of this predicted boundary are selected for observation. We updated the observing list as needed as we took more data and revised and tightened the age estimate. Stars were prioritized for observing based on their *Gaia* RP magnitude and location on sky. We omitted stars with *Gaia* $RUWE > 1.2$, as they are more likely to be binaries, which can contaminate the age result.

To measure the EW of the Li 6708 Å line, we used Goodman's red camera, 1200 l/mm grating, and the M5 mode, providing a wavelength coverage of 6300–7400 Å. We varied the slit width used between the 0.45″ slit and the 0.6″ slit depending on the target magnitude

and the atmospheric seeing. This setup should give a resolving power of R = 4500–5800, although in practice the true resolution is lower and varies with exposure time (see below). For each target, we take five spectra with exposure times varying from 10 to 300 s each.

To reduce the spectra we perform standard bias subtraction, flat-fielding, and optimal extraction of the target spectrum. Issues with the mount model and flexure compensation system cause large wavelength shifts during and between exposures, with shifts up to 5–10 pixels between subsequent exposures. Following Wood et al. (2023), we correct this effect using simultaneous skyline spectra and Ne arc spectra taken prior to each image. We use a fourth-order polynomial wavelength solution derived from the Ne arc and corrected with a linear factor based on the simultaneous skyline spectra to wavelength calibrate each individual exposure, which we then stack using a weighted mean. Each star is then corrected to its rest wavelength using radial-velocity standards taken with the same setup. While the resulting spectra were useful for determining spectral type and measuring EW(Li), we found that measured RVs had $\sigma_{\rm rv} \simeq 5 - 10$ km s^{-1}, based on spectra of RV standard stars. Therefore, we do not use these spectra to measure RV for membership confirmation.

4.2.2 LCO/NRES

To supplement our measurements of Li in low-mass association members we also obtain spectra of 3 higher-mass stars using the Network of Robotic Echelle Spectrographs (NRES) (Siverd et al., 2018) at the Las Cumbres Observatory. Observations were taken between 2022 Aug 22 and 2022 Sept 9.

The NRES spectra cover a wavelength range of 380–860 nm with high resolution ($R \sim 53,000$). The data are reduced using the LCO NRES pipeline `BANZAI-NRES`[1]. Radial velocities are extracted through cross-correlation of the spectra with PHOENIX model atmospheres (Husser et al., 2013). We measure the EW of the Li 6708 Åabsorbtion line, used

[1] `https://github.com/LCOGT/banzai-nres`

Table 4.1 Observations of Carina candidate members.

Object	ObsDate YYYYMMDD	Telescope	EW(Li) mA mÅ	M_{K_s} mag
TIC 238236508	Goodman/SOAR	20200206	529.5	7.18
TIC 350559457	Goodman/SOAR	20200206	203.9	7.25
TIC 167890419	Goodman/SOAR	20200305	646.9	7.22
TIC 341935294	Goodman/SOAR	20200305	702.6	7.60
TIC 167815117	Goodman/SOAR	20220218	618.0	7.15
TIC 308085979	Goodman/SOAR	20220218	< 10	6.92
TIC 308186410	Goodman/SOAR	20220218	226.4	6.87
TIC 349195685	Goodman/SOAR	20220218	< 10	6.60
TIC 355794672	Goodman/SOAR	20220218	627.0	6.99
TIC 384950919	Goodman/SOAR	20220218	32.3	4.73
Gaia 5258513835596515328	Goodman/SOAR	20220218	0.0	6.05
TIC 302959739	Goodman/SOAR	20220219	377.6	6.87
TIC 355373774	Goodman/SOAR	20220219	490.6	6.90
TIC 452522881	Goodman/SOAR	20220219	< 10	6.54
TIC 238714485	Goodman/SOAR	20220220	632.6	7.09
TIC 460371874	Goodman/SOAR	20220220	0.0	5.8
Gaia 5302978704290910592	Goodman/SOAR	20220220	490.0 ± 30.6	7.1
HD 42270	NRES/LCO	20220905	229.9 ± 11.3	3.096
HD 21024 (iot Hyi)	NRES/LCO	20220822	0.0 ± 6.3	2.144
HD 44627	NRES/LCO	20220909	183.2 ± 13.6	3.480

in Section 4.3.3 to determine the age of the association. Observations and resulting Li measurements are listed in Table 4.1.

4.2.3 Archival

We obtain archival astrometry, photometry, velocities and the *Gaia* renormalized unit weight error (RUWE) for association members from *Gaia* DR3 (Gaia Collaboration et al., 2022).

We also obtain the J, H, and K_S magnitudes for all applicable members from 2MASS (Skrutskie et al., 2006).

Table 4.2 Observations of Theia 92 and Theia 113 candidate members.

Object	ObsDate YYYYMMDD	EW(Li) mA mÅ	M_{K_s} mag	Population
Gaia 5277938907510375168	20221213	324.8 ± 42.2	7.22	Theia 92 Pop 1
Gaia 5290199492952302720	20220419	0.0 ± 0.0	7.12	Theia 92 Pop 1
Gaia 5291690911754950272	20220405	187.0 ± 0.0	6.81	Theia 92 Pop 1
Gaia 5296320302384050176	20221213	206.8 ± 29.4	7.18	Theia 92 Pop 1
Gaia 5296484473215369472	20221213	0.0 ± 0.0	7.33	Theia 92 Pop 1
Gaia 5303193487017684352	20220408	295.0 ± 0.0	6.77	Theia 92 Pop 1
Gaia 5303331544444159104	20230108	465.9 ± 23.6	7.03	Theia 92 Pop 1
Gaia 5304872166403179520	20220411	0.0 ± 0.0	6.92	Theia 92 Pop 1
Gaia 5305011941814755328	20220411	0.0 ± 0.0	6.78	Theia 92 Pop 1
Gaia 5317907667010627840	20230108	515.7 ± 40.0	7.23	Theia 92 Pop 1
Gaia 5324513356772906880	20230108	584.5 ± 29.3	7.12	Theia 92 Pop 1
Gaia 5209201563706924288	20220419	< 10	7.04	Theia 92 Pop 2
Gaia 5215182391566488448	20220408	< 10	6.56	Theia 92 Pop 2
Gaia 5234867944690161024	20220419	< 10	7.20	Theia 92 Pop 2
Gaia 5238398270373156992	20220419	< 10	7.03	Theia 92 Pop 2
Gaia 5238609720201092736	20220408	< 10	6.76	Theia 92 Pop 2
Gaia 5338163866701296512	20220411	< 10	6.84	Theia 92 Pop 2
Gaia 5250317045125172864	20230314	< 10	7.40	Theia 113
Gaia 5285443280524870656	20230226	684.5 ± 27.0	7.22	Theia 113
Gaia 5286978645433636480	20230226	436.1 ± 39.5	7.15	Theia 113
Gaia 5294658424917969664	20230201	97.8 ± 59.5	7.13	Theia 113
Gaia 5302275326082224512	20230201	< 10	6.88	Theia 113
Gaia 5483922171768774656	20230314	68.8 ± 34.9	7.08	Theia 113
Gaia 5484101220364730240	20230314	< 10	6.99	Theia 113
Gaia 5484101220364730240	20230201	< 10	6.99	Theia 113
Gaia 5495275694476824320	20230201	< 10	6.71	Theia 113

Note. — All observations were made using Goodman HTS on SOAR 4.1m telescope.

4.3 Revised age of Carina

4.3.1 Isochrone

We first estimate the age of Carina by comparing *Gaia* photometry of stars in our updated membership list to two sets of isochrones: PARSECv1.2 (Bressan et al., 2012) and the Dartmouth Stellar Evolution Program (DSEP, Dotter et al., 2008) with magnetic enhancement Feiden (2016). Both model grids have been shown to perform well on 10–150 Myr associations like Carina (e.g., Gillen et al., 2017; Mann et al., 2022; Wood et al., 2023).

For this comparison, we use a mixture model following Mann et al. (2022). To briefly summarize, the likelihood is formed from the mixture of two models (Hogg et al., 2010). The first model represents the single-star sequence of true members, and is described by two parameters: age (τ) and reddening ($E(B-V)$). The second model captures the outliers, which may include binaries, non-members, or stars with problematic photometry or parallaxes. The second model is described with two parameters: the offset from the first model (Y_B) and the variance around that offset (V_B). An additional free parameter describes the amplitude of the second model (P_B), and serves as an estimate for the fraction of stars in the outlier population. More details, including the likelihood function, can be found in the appendix of Mann et al. (2022).

We wrap the likelihood in a Monte Carlo Markov Chain (MCMC) framework using `emcee` (Foreman-Mackey et al., 2013). The MCMC is run for 10,000 steps after an initial burn-in of 1,000 steps, which far exceeded 50 times the autocorrelation time generally required for convergence. All parameters evolve under uniform priors with only physical limitations. Extinction is allowed to go negative to avoid Lucy-Sweeney bias (Lucy & Ricco, 1979) and because we expect such nearby stars to have minimal reddening. To ensure uniform sampling in age, we re-sample the underlying model isochrones to increments of 0.1 Myr using the `isochrones` package (Morton, 2015). We assume Solar metallicity, which is generally the case.

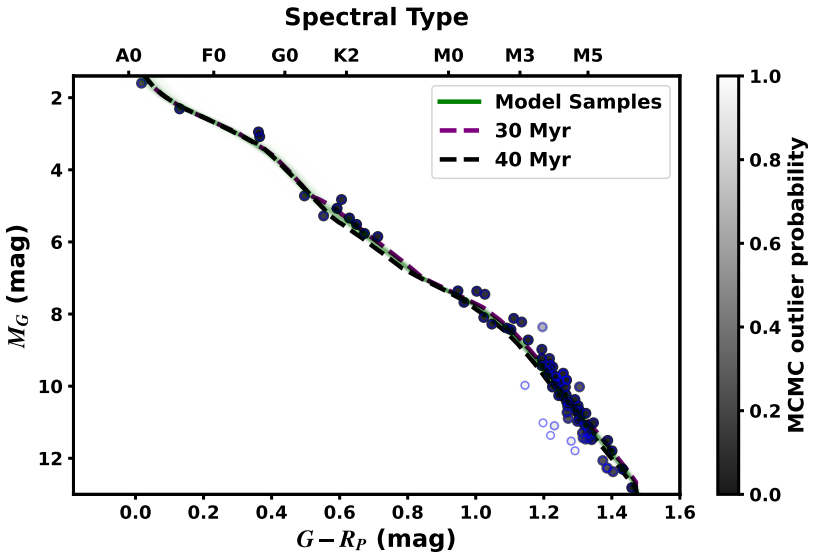

Figure 4.2 Comparison of Carina members (blue circles) with PARSECv1.2 stellar evolutionary models. The green lines are 200 random samples from our MCMC analysis, and the two dashed lines are the 30 and 40 Myr isochrones for comparison. Points are shaded based on the probability that they are part of the main population or the outlier population.

We show the *Gaia* CMD and model fit in Figure 4.2. The final fit yields an age of $\tau = 34 \pm 3$ Myr when using the PARSEC models, and $\tau = 38 \pm 3$ Myr when using the DSEP magnetic models. Different input assumptions, such as locking $E(B-V)$ to zero or allowing for non-Solar metallicity ($-0.3 <$[M/H]< 0.3), or changing the assumed solar abundance scale, shifts the resulting age at the $\simeq$3 Myr level, similar to the reported errors and and the difference between the result of the two model grids.

4.3.2 Lithium Depletion Boundary

We use the EW(Li) measurements obtained above to determine the association age in two ways: the LDB method, and by comparing the full Li sequence to benchmark associations.

Identifying the LDB requires defining the threshold between Li-rich and Li-poor stars (e.g., Binks & Jeffries, 2014; Binks et al., 2021). We use $EW(Li) = 200$ mÅ as the threshold, following Binks & Jeffries (2014). With this threshold 12 of the observed stars are Li-rich (see Table 4.1 for Li measurements). The boundaries of the LDB are defined by the faintest

Table 4.3 LDB results for Carina

Model	Lower Bound	Upper Bound
BHAC15	36 Myr	37 Myr
DSEP (GS98)	38 Myr	39 Myr
DSEP Mag (GS98)	41 Myr	42 Myr
DSEP Mag (AGSS09)	44 Myr	45 Myr
SPOT (17%)	42 Myr	42 Myr
SPOT (34%)	45 Myr	47 Myr

.

Note. — Upper and lower age bounds given by each of the models used. The upper bound corresponds to the age given an LDB at the magnitude of the faintest observed star without Li, and the lower bound corresponds to the age given an LDB at the magnitude of the brightest observed stars with Li.

Li-poor and brightest Li-rich stars, so we find that the LDB is $6.87 < M_{K_s} < 6.92$, shown in Figure 4.3.

By comparing this magnitude range to stellar evolutionary models we determine the age of the association. We use several different models with varying treatment of convection, magnetic fields, and spots. For standard models we use the BHAC15 (Baraffe et al., 2015) and DSEP (Dotter et al., 2008) models. To include magnetic fields we use the Dotter models with magnetic enhancement (Feiden, 2016), and SPOT models with 17% and 34% spot coverage (Somers et al., 2020). For each model the magnitude corresponding to 99% Li depletion is calculated at each age provided. We then linearly interpolate the resulting relationship between LDB magnitude and age to find the predicted age for the observed LDB. We repeat this interpolation using the top and bottom edges of the LDB to determine lower and upper age limits, with each model, shown in Table 4.3. An overall age estimate is calculated by averaging the estimates, resulting in an age of 41.5 ± 3.2 Myr.

A higher threshold of $EW(Li) > 300$ mÅ(as in Binks et al. (2021)) results in 3 of the Li-rich stars becoming Li-poor, for a total of 9 Li-rich stars. This changes the LDB bounds to be $6.87 < M_{K_s} < 7.25$, resulting in a slightly older age of 45.3 ± 5.7 Myr, which is still within the 2σ uncertainty bounds.

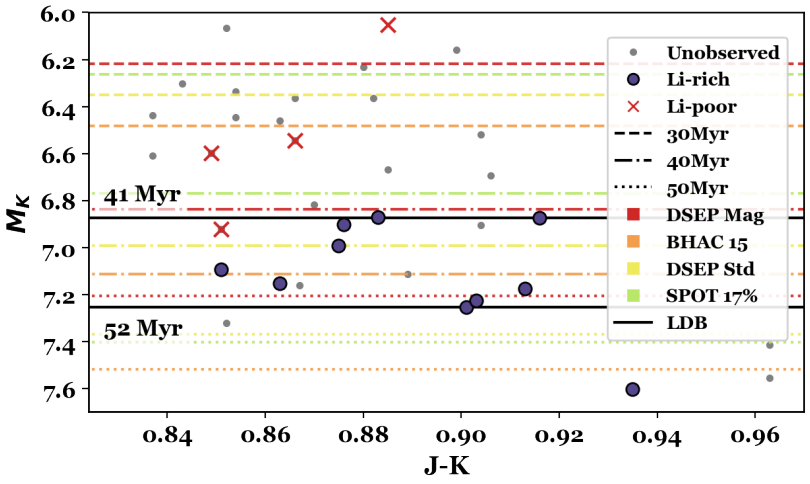

Figure 4.3 The lithium depletion boundary of Carina. Lithium-rich stars ($EW(Li) > 200$ mÅ) are shown as dots, and lithium-poor ($EW(Li) < 200$mÅ) ones as red x's. Black horizontal lines are drawn through the brightest Lithium-rich star and the faintest Lithium-poor one, and labeled with the corresponding age using the DSEP magnetic model. The magnitudes of 99% Lithium depletion at 30, 40 and 50 Myr for each model are shown as colored lines, where the color indicates the model and the line style the age.

4.3.3 Lithium Sequence

The Li sequence is an alternative method which utilizes Li measurements across a larger range of stellar masses. By comparing Li abundance as a function of color to either evolutionary modes or benchmark associations, an age can be determined (Soderblom et al., 2014). When comparing to evolutionary models the dependence on initial Li abundance and greater reliance on factors such as convective overshoot make this method less robust to changes in model and less consistent than LDB. Using empirical comparison, the resulting age is only as model dependent as the age measurements of the benchmark association it is based on.

To construct the Li sequence of Carina we use our Li measurements of low- and moderate-mass stars (see Table 4.1), supplemented with additional measurements from Riedel et al. (2017) and Schneider et al. (2019). We obtain 13 measurements from Riedel et al. (2017), and 3 from Schneider et al. (2019), listed in Table 4.4. Of the 13 taken from Riedel et al. (2017), eight were considered Carina members by them, while the remaining were either

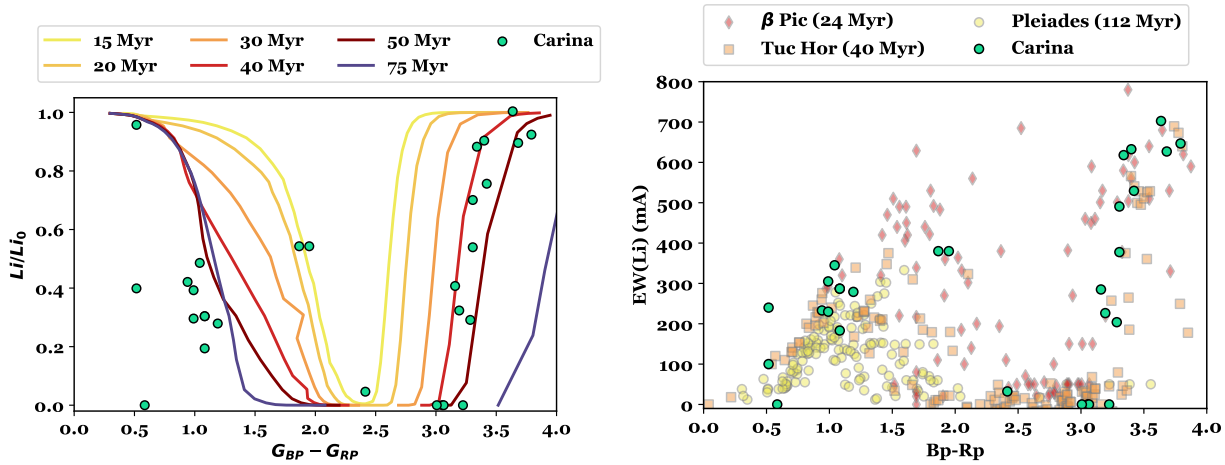

Figure 4.4 Lithium measurements of Carina. Left) Fraction of initial Li abundance as a function of *Gaia* BP−RP, overplotted with DSEP magnetic isochrones (Feiden, 2016). Equivalent widths of association members were converted to Li/Li_0 using the curve of growth from Zapatero Osorio et al. (2002) for $T_{\rm eff} < 4000K$ and from Soderblom & Mayor (1993) for $T_{\rm eff} > 4000K$. Right) Lithium equivalent widths for observed Carina members are shown as teal dots plotted on top of the observed Li Sequences of the Beta Pictoris Moving Group (24 Myr, red; Binks & Jeffries, 2014), Tucana-Horologium Young Association (40 Myr, orange, Kraus et al., 2014), and the Pleiades (115 Myr, yellow, Bouvier et al., 2018).

members of other nearby young associations (TW Hya and Tuc-Hor) or were not assigned membership in any association. We find that all have $P_{BANYAN} > 60\%$.

The Li sequence of Carina lies very near that of the 40-Myr-old Tuc-Hor association, shown in the right panel of Figure 4.4. The association has less Li at $B_P - R_P \simeq 3.0$ than the β Pic moving group ($24\,Myr$), and does not transition to Li-rich stars until $B_P - R_P \simeq 3.25$. This supports the LDB age of 41 ± 3 Myr.

4.4 Theia Groups

The Theia groups were discovered using an unsupervised machine-learning clustering algorithm in a galactic latitude and longitude coordinate frame (Kounkel & Covey, 2019). Two of these groups, Theia 92 and Theia 113, were later proposed to be part of the Carina-Columba complex.

Table 4.4 Literature Li measurements for Carina members.

Object	Gaia DR3	EW[Li] (mÅ)	Source
HD 49855	5265670762922792960	233.0	Riedel et al. (2017)
TWA 21	5356713413789909632	369.0	Riedel et al. (2017)
HD 42270	4621305817457618176	305.0	Riedel et al. (2017)
AB Pic*	5495052596695570816	287.0	Riedel et al. (2017)
AB Pic B*	5495052596695570816	287.0	Riedel et al. (2017)
HD 37402	4759444786175885824	110.0	Riedel et al. (2017)
2MASS J04082685-7844471	4625883599760005760	7.5	Riedel et al. (2017)
HD 55279	5208216951043609216	279.0	Riedel et al. (2017)
V0479 Car	5299141546145254528	345.0	Riedel et al. (2017)
2MASS J02564708-6343027	4721078629298085760	9.2	Riedel et al. (2017)
HD 269620	4658442922197295232	226.0	Riedel et al. (2017)
HD 83096*	5217846851839896704	100.0	Riedel et al. (2017)
HIP 46720B*	5217846851839896704	240.0	Riedel et al. (2017)
2MASS J07065772-5353463	5491506843495850240	380.0	Schneider et al. (2019)
2MASS J09032434-6348330	5297100607744079872	380.0	Schneider et al. (2019)
2MASS J09180165-5452332	5310606291358320512	285.0	Schneider et al. (2019)

Note. — *Unresolved Binary in *Gaia*.

To test this relationship we aimed to measure LDB ages for Theia 113 and Theia 92 and compare them to my measured age for Carina as well as the other nearby groups. Unfortunately, due to lost telescope time, not enough data has been collected for a final age determination. However, our preliminary analysis of Theia 92 and Theia 113 finds that Theia 92 is composed of two separate populations and suggests that the groups have a similar age to Carina.

4.4.1 Structure of Theia 92

Containing over a thousand candidate members, Theia 92 is one of the largest populations identified in Kounkel & Covey (2019). They identified Theia 92 with the previously known open cluster, IC 2602. A later paper identified Theia 92 as a mixed population, parts of which are identified with IC 2602, and parts with the Carina-Columba complex (Gagné et al., 2021).

We find that Theia 92 can be divided into two populations, which, using galactic Cartesian coordinates are split at $X \simeq 30$ pc (see Figure 4.5). We refer to these as Theia 92 Population 1 (Pop 1) and Theia 92 Population 2 (Pop 2), where Pop 1 includes all members with $X < 30$ pc, and Pop 2 those with $X > 30$ pc.

Pop 2 contains the Thiea 92 members that correspond to IC 2602 and an extended set of stars which have not previously been identified as members of IC 2602 (e.g., Nisak et al., 2022) (see Figure 4.6).

The two populations comprising Theia 92 may be part of separate associations or complexes, which were grouped together by the clustering algorithm due to their proximity, or they may be more closely related and form a larger complex. Gagné et al. (2021) claim that IC 2602 and Carina (and its related groups) are part of separate complexes, where IC 2602 is combined with part of Theia 92, and Tucana-Horologium and the Carina-Columba complex is joined through Theia 113, 208 and part of Theia 92 to the Platais 8 association. Alternatively, Kerr et al. (2021) places IC 2602 and Platais 8 as part of the larger structure

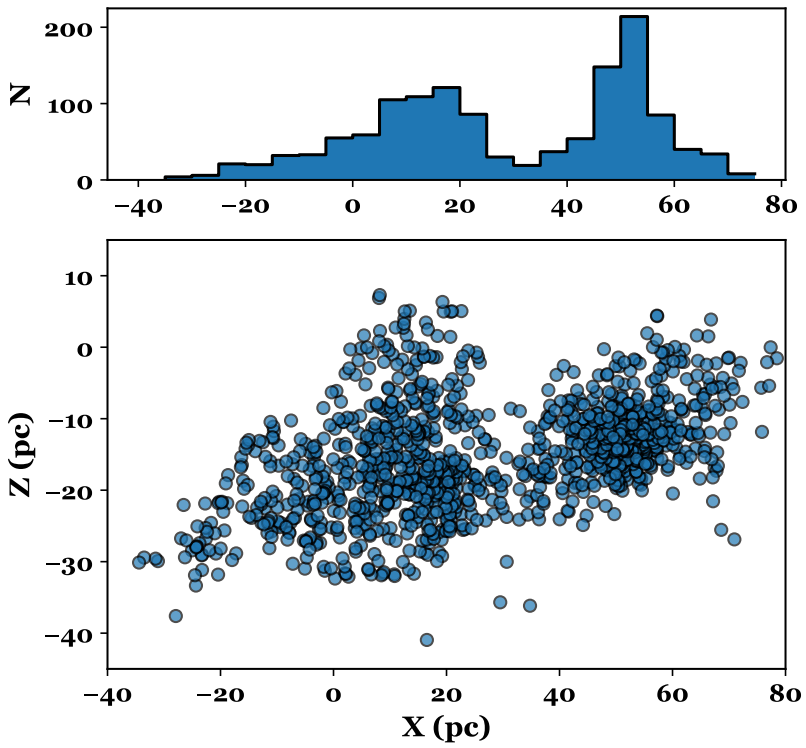

Figure 4.5 Positions of Theia 92 members in galactic coordinates X and Z. Top panel shows a histogram of members in X, showing the bimodal distribution, which suggests that Theia 92 is two populations.

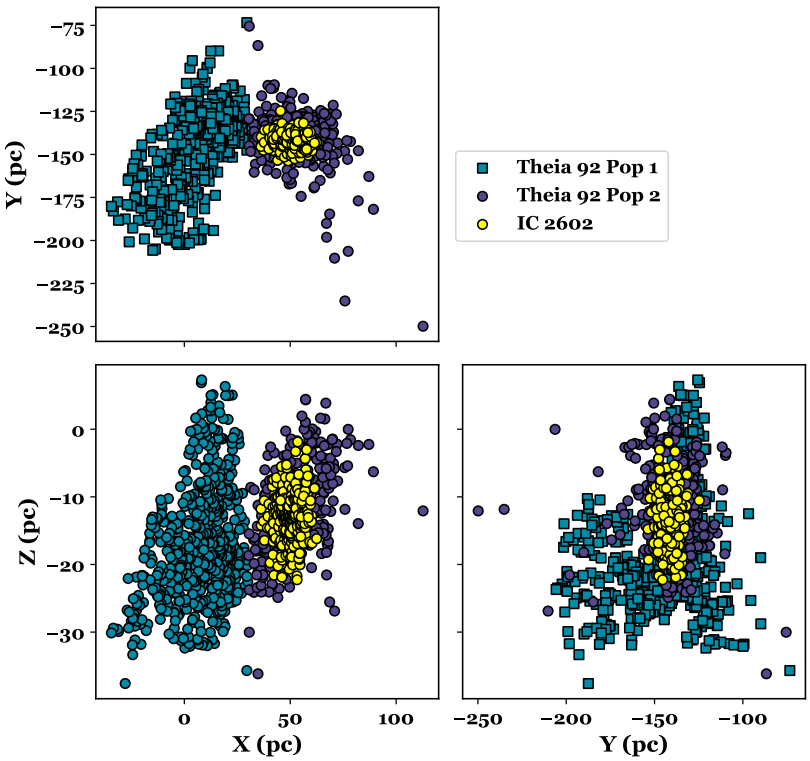

Figure 4.6 Comparison of Theia 92 and IC 2602 membership. Positions of Theia 92 and IC 2602 members are shown in galactic coordinates X, Y and Z. IC 2602 and Theia 92 Population 2 are the same.

of Sco-Cen. Thus, if the two populations are related it creates a connection between many of the associations in that area, including Platais 8, IC 2602, Tuc-Hor and Carina-Columba. By measuring the ages of each of these possibly related associations, we hope to determine if they share a common age, and thus are likely related.

4.4.2 Age

To measure the ages of the Theia 92 populations and Theia 113 we use Li measurements obtained using the Goodman HTS on SOAR (See Section 4.2). Observed members and Li measurements are listed in Table 4.2.

We compare the Li sequences of each of the populations, shown in Figure 4.7, to that of Carina and other benchmark associations to empirically check if they have similar ages. We find that the Li sequences of Theia 92 Pop 1 and Theia 113 are very similar to that of Carina,

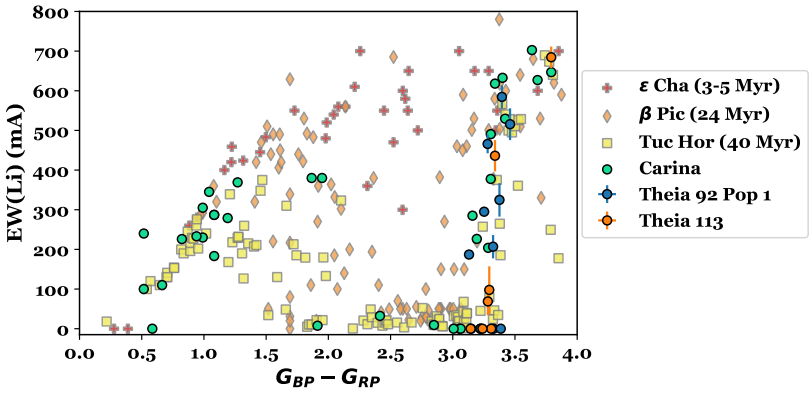

Figure 4.7 Lithium measurements of Theia 92 and 113 members are shown plotted on top of the observed Li Sequences of Carina (this work), Beta Pictoris Moving Group ($21 Myr$, red) Binks & Jeffries (2014), Tucana-Horologium Young Association ($40 Myr$, orange) (Kraus et al., 2014), and the Pleiades ($115 Myr$, yellow) (Bouvier et al., 2018).

with a transition from Li-poor to Li-rich stars at $G_{BP} - G_{RP} \simeq 3.25$. This suggests that they are the same age and may be related. However we refrain from estimating a precise LDB age for those groups at this time, as more observations are needed to map the boundary, and to determine the cause of several stars in Theia 92 Pop 1 with lower than expected Li abundances.

Theia 92 Pop 2 presents a more difficult case, as although we have observed candidate members with magnitudes up to $K_S = 7.2$, none of the yet observed candidates show Li absorption. Dobbie et al. (2010) measured a LDB for IC 2602, finding that the LDB lay between apparent magnitude $13.13 < K_S < 13.34$. This is significantly fainter than our identified LDB for Carina, which is at apparent $11.3 < K_S < 11.5$. Our lack of Li detections at magnitudes which are Li-rich in Carina and Theia 92 Pop 1, combined with the findings of Dobbie et al. (2010) suggest that Theia 92 Pop 2 may be older than the other groups and not a part of the complex.

CHAPTER 5: CONCLUSION

5.1 Summary

In this dissertation I have presented my work measuring the ages of several nearby, young, planet hosting associations. This final chapter summarizes the results of my work and discusses the future outlook of association age determinations.

5.1.1 Musca

TOI-1227 is an $\simeq$11 Myr giant planet (0.85 R_{Jup}) orbiting a low-mass M star (0.17 $M_\odot$) in the LCC region of the Sco-Cen OB association. Recent work on LCC has identified substructures, i.e., smaller populations, each with slightly different Galactic motion, position, and age. TOI-1227 was flagged as a member of the A0 group by Goldman et al. (2018) and LCC-B by Kerr et al. (2021), which are effectively the same group. Because of the contradictory and easily forgotten naming conventions, we denote this group Musca after the constellation containing most of the members.

As part of our effort to better measure the age of TOI-1227, we used rotation, lithium, and stellar evolution models to determine an age of 11$\pm$2 Myr for Musca, and hence TOI-1227. The young age placed the system as one of only two systems with transiting planets younger than 15 Myr (K2-33 b; Mann et al., 2016a; David et al., 2016), and one of only eleven transiting planets younger than 100 Myr (V1298 Tau, DS Tuc, AU Mic, TOI 837, HIP 67522, and TOI 942 David et al., 2019; Newton et al., 2019; Benatti et al., 2019; Plavchan et al., 2020; Rizzuto et al., 2020; Bouma et al., 2020; Zhou et al., 2020; Carleo et al., 2021). Even including radial velocity detections only adds a few additional planets (Johns-Krull et al.,

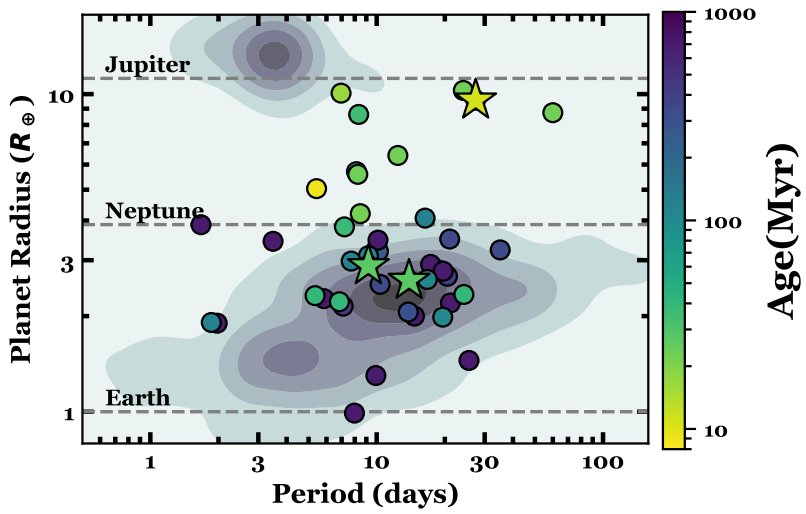

Figure 5.1 Radius-Period distribution of known exoplanets. Planets with ages $< 700 Myr$ are shown as individual points, with the older population of stars shown as a density plot. Young planets are more likely to occur in the radius gap between Neptune- and Jupiter- sized planets, indicating that planets may form in that gap and then shrink. Planets discussed in this work - TOI-1227 b, HD 109833 b & HD 109833 c, are shown as stars. Adapted from Wood et al. (2023) under CC 4.0 license.

2016; Yu et al., 2017; Donati et al., 2016), some of which are still considered candidates (Donati et al., 2020; Damasso et al., 2020).

Like K2-33 b, TOI-1227 is inflated, with a radius much larger than known transiting planets orbiting similar-mass stars (Figure 5.1). TOI-1227's radius is closer to Jupiter than to the more common 1–3 $R_\oplus$ planets seen around mid-to-late M dwarfs (Berta et al., 2013; Hardegree-Ullman et al., 2019). Such a large planet would be obvious in surveys of older M dwarfs, given that the equivalent mature M dwarfs are both less variable and a factor of a few smaller than their pre-main-sequence counterparts. Thus, TOI-1227 is evidence of significant size evolution, especially when combined with similar earlier discoveries.

Interestingly, evolutionary models favor a final radius for TOI-1227 of $>3\,R_\oplus$, which would still be abnormally large (Figure 5.1) for the host star's mass. However, that discrepancy is easier to explain as observational bias (see Mann et al., 2022). Furthermore, the evolutionary tracks are poorly constrained by the existing young planet population, especially

given that AU Mic b is the only <50 Myr planet with both mass and radius measurements (Klein et al., 2021; Cale et al., 2021). The lack of masses remains a significant challenge for these kinds of comparisons (Owen, 2020). TOI-1227 is too faint for radial velocity follow-up in the optical, but might be within the reach of high-precision NIR monitoring. Our IGRINS monitoring achieved 40–50 $\mathrm{m\,s^{-1}}$ precision, which is below the level from the stellar jitter. More dedicated monitoring and careful fitting of stellar and planetary signals should be able to detect a planet below $\simeq 40\,M_\oplus$.

A less challenging follow-up would be spin-orbit alignment through Rossiter-Mclaughlin, where the signal is expected to be $>200\,\mathrm{m\,s^{-1}}$ and the transit timescale ($\simeq$5 h) is much shorter than the rotational jitter (1.65 days). Recent measurements of stellar obliquity in young planetary systems have found that they are generally aligned with their host stars (e.g., Rodriguez et al., 2019; Zhou et al., 2020; Wirth et al., 2021), suggesting that these planets formed in situ or migrated through their protoplanetary disk. However, the number of misaligned systems even around older stars is $\lesssim$10% (varying with spectral type and planet mass; Fabrycky & Winn, 2009; Morton et al., 2016; Campante et al., 2016). We likely need a larger sample of obliquity measurements in young systems for a significant statistical comparison.

Follow-up and characterization of TOI-1227 highlight the difficulties of characterizing and validating such young planets. We initially mischaracterized both the host star and planet, and ground-based transits yielded contradictory results. The host star (TOI-1227) was initially thought to be part of the $\simeq$5 Myr ϵ Cha cluster, based on the `BANYAN` code. At that age, the stellar host would be even larger, yielding an even larger radius for the planet and creating a more complex set of false-positive scenarios (e.g., the planet's radius would be more consistent with a young brown dwarf). Without *Gaia*, it is unlikely that Musca would have been recognized, and assigning TOI-1227 to a given population without a parallax would have been extremely challenging.

Similarly, the THYME team originally flagged TOI-1227 as a likely eclipsing binary based on its V-shaped transit and large depth. Only with the HRS/SALT spectra and a consistent transit depth from Goodman/SOAR did we pursue further follow-up. This motivated both spectroscopic monitoring with IGRINS and the suite of multi-band transit photometry observed over $\simeq$1.5 years to better characterize the planet. While the majority of the transit photometry painted a clear picture that the signal was from a planet, a single transit showed an inconsistent transit depth, suggesting a false positive. We argued in (Mann et al., 2022) that regular flaring, the planet occulting spots, or simply low-precision photometry, could easily explain the unusual transit. Spots could also explain why our other g' transits were deeper than the i' and z_s data; if the transit chord has fewer spots than the rest of the stellar surface, the bluest transits appear deeper (this was seen in K2-25; Thao et al., 2020).

While the case for TOI-1227 as a planet is strong, the initially confusing results raise concerns about the future follow-up of young planets. Radial velocity detection remains challenging. As with K2-25 b, the discovery transit for TOI-1227 was V-shaped, making it hard to classify on transit depth and shape alone. Transits from young planets are likely to depend on wavelength even if the planet is real given the presence of spots, and smaller planets are not as amenable to the large suite of ground-based follow-up used here. Earlier studies often used *Spitzer*, which provided the advantage of a wide wavelength range while operating in a regime where the effects of spots and flares are significantly smaller. With the end of *Spitzer*, we may need to focus on improving the NIR photometric precision from the ground. For now, we encourage caution when rejecting young planets based on metrics tuned for older systems.

5.1.2 MELANGE-4 and TOI-1097

In Chapter 3, we presented a new, 27 ± 3 Myr old association (MELANGE-4) on the outskirts of LCC. We initially identified the group from a population of pre-main-sequence M

dwarfs co-moving with a candidate transiting-planet host from *TESS* (TOI 1097). We gather a wide range of ground-based follow-up and archival data with the goals of 1) improving the list of likely members, 2) measuring the age and basic parameters of the association, 3) confirming that the group is distinct from known young populations (Carina and LCC), and 4) validating and characterizing the planetary system TOI 1097.

We first searched for candidate members using an iterative process, resulting in a list of 306 candidate members. A small number ($\lesssim 10$) of the candidates sit unusually high or low on the CMD (see Figure 3.2) or have low lithium levels for their spectral type (see Figure 3.6). Thus, the list is not totally clean, but is still sufficient to estimate the age and properties of the group.

MELANGE-4's rotation, CMD, and lithium levels are consistent with an age of 25–30 Myr. Rotation provides only a qualitative check on the age (and membership) due to the large spread in rotation periods at this age (Rebull et al., 2018). A fit to the CMD with stellar models offers a consistent and arguably more precise age (26±2 Myr), with an additional 2 Myr error based on differences between model grids and input assumptions. The most reliable age constraint comes from the lithium depletion, which provides an age of 27 ± 3 Myr that is almost entirely independent of model selection (see Table 3.4).

The association is kinematically close to LCC but is distinct in position, velocity, dispersion, and age. The LCC subpopulation which is closest in XYZ is most discrepant in velocity, and the group with the most similar velocity is furthest in XYZ. Additionally, all of the known LCC sub-groups are significantly younger, making a common origin extremely unlikely. The oldest age for an LCC subgroup found in Section 2.5 is 16.6 ± 1.1 Myr, inconsistent with our isochronal age (26 ± 2 Myr) and lithium-depletion age (27 ± 3 Myr) for MELANGE-4.

Of the other known moving groups in Gagné et al. (2018), the two closest in kinematics are Carina ($\Delta V \simeq 3.4$ km s^{-1}) and Columba ($\Delta V \simeq 4.1$ km s^{-1}). The cores of these groups are more than 30 pc from MELANGE-4 and are significantly older ($\simeq$45 Myr) than

MELANGE-4. A more complicated possibility is that MELANGE-4 is a mix of members from Carina, Columba, and LCC. However, if this were the case we would expect Li-rich low-mass stars to be preferentially closer to LCC and Li-poor ones close to Carina. We find instead that Li-rich PMS stars are spread throughout the association. We conclude that MELANGE-4 is distinct from any known young association.

We report the discovery of two transiting planets around the Sun-like star HD 109833, which we identify as a likely member of MELANGE-4. *TESS* first identified the first planet, while our Notch analysis (and later *TESS*) identified the second planet. Both planets are super-Earth sized, with radii of $2.9R_E$ and $2.6R_E$, and periods of 9.2 and 13.9 days, close to a 3 : 2 resonance. We validate object b as planetary in nature. Object c was a weaker detection and had an unusually short duration; `triceratops` gave a FPP of 10%. However, with the multiplicity boost, both planets meet the requirements for statistical validation.

Along with the newly discovered two-planet system around HD 109833 (Wood et al., 2023), three high-probability candidate members have directly-imaged planetary-mass companions, TYC 8998-760-1, HD 95086, and TYC 8984-2245-1 (Rameau et al., 2013; Bohn et al., 2020b, 2021). These systems were previously placed in LCC or the Carina moving group, with assumed younger ages. Our older age changes the masses and inferred properties of the planets.

HD 109833 is *not* an unambiguous member of MELANGE-4. This is especially surprising since the planet-host was the seed of our initial search that identified MELANGE-4. Most of our data favor membership. However HD 109833 has a lower CMD position than predicted for the age of MELANGE-4, and lies on the outskirts of the group in U and V velocity. As discussed in Section 3.3.4, this may be an issue with the models, as the onset of H burning at that spectral class produces a reduction in luminosity. While HD 109833 is clearly young (< 200 Myr), the lithium levels are lower than expected for this age (Gutiérrez Albarrán et al., 2020) and compared to similar stars in the same association (Figure 3.6). The rotation period matches expectations for members of MELANGE-4, but is also consistent with ages up to

200 Myr. The strongest evidence in favor of membership is the 99.8% BANYAN Σ membership probability. We conclude that HD 109833 is likely part of MELANGE-4, but we cannot reject the possibility that it is a young field star coincidentally moving with MELANGE-4.

An older age for HD 109833 does not significantly impact our inferred properties of the star or planet. A star of this $T_{\rm eff}$ exhibits minimal change in CMD properties between hitting the main-sequence ($\simeq$30 Myr) to the oldest ages consistent with Li and rotation (100–200 Myr), and our $T_{\rm eff}$ and R_* estimates did not make any assumptions about the age.

While the observed young-planet sample has grown dramatically in the last five years (e.g., Mann et al., 2016a; David et al., 2016; Newton et al., 2019; Benatti et al., 2019), there are still few planets younger than 200 Myr, and very few known multi-planet systems of that age, so this discovery radically expands our sample of young planetary systems. Interestingly, both planets have radii comparable to field-age stars, while most of the young ($<$ 100 Myr) transiting planets land in the sub-Saturn desert (4–10 $R_\oplus$; Figure 5.1). This is less compelling if we adopt the older (100–200 Myr) age, but most planets at that age still appear inflated compared to their older counterparts (e.g., Newton et al., 2022).

The small size of the planets may be caused by photoevaporation of their atmospheres by high-energy radiation from the host star. However, comparison to the similar system V1298 Tau, a 23 Myr, multi-planet system in Group 29 (David et al., 2019), shows that this may be unlikely. Poppenhaeger et al. (2021) find the x-ray luminosity, L_X, of V1298 Tau to be $L_X = 10^{30.1}$ erg/s. The x-ray luminosity of HD 109833, calculated using the flux found by Freund et al. (2022), is comparatively lower, at $L_X = 10^{29.07}$ erg/s. If photoevaporation is the driving factor of the planets' sizes we would expect TOI-1097, being a similar age and having lower L_X, to have larger planets than V1298 Tau. However, V1298 Tau c and d, with periods of 8.25 and 12.40 days respectively, have sizes $R_{P,c} = 5.59 R_\oplus$, and $R_{P,d} = 6.41 R_\oplus$, about twice the size of HD 109833 b and c.

The orbital periods of the planets also fall near a 3:2 mean motion resonance, making this system one of only a few known young systems near resonance (e.g., Feinstein et al.,

2022). The mechanism responsible for resonant chains is still unknown, and establishing the timescale in which they form is critical for understanding this process.

As a new and nearby association with hundreds of candidate members, MELANGE-4 is an excellent subject for future observations and research. We do not expect that the membership presented here is either complete or contaminant-free, so additional studies on the membership and additional RV measurements are needed to better delineate the association members. Further observations of low-mass members to measure their Li abundance would improve the limits on the LDB age, which is currently limited by the small number of Li detections in the relevant mass range. New planet searches focusing on candidate members may find more ~ 30 Myr planets within the association, further increasing the sample of young planets, while future studies on the relationship between MELANGE-4 and the nearby young associations could improve understanding of the cloud-collapse and star-formation process.

The planet host, TOI-1097, is also a promising subject for follow-up given its proximity to Earth and bright magnitude ($G = 9.14$). Additional observations may help to solidify its membership in MELANGE-4, or reject it as a member. Further characterization of the planets, including mass measurements and better constraints on eccentricity, may be possible with a search for transit timing variations.

5.1.3 Carina-Columba Complex

We measured the age of the Carina association using new Li measurements and the LDB method. Using *Gaia* DR3 kinematic measurements and `BANYAN` Σ code with an updated list of associations, we created a new membership list of Carina, containing 99 stars. We obtained medium-resolution optical spectra of low-mass association members using the Goodman HTS on the 4m SOAR telescope and supplemented these with spectra of K-type members taken with NRES on LCO. From these spectra we measured EW(Li), located the LDB, and constructed a Li sequence of the association. Comparing the LDB and Li sequence to stellar

evolutionary models and benchmark associations reveals an age of 41 $\pm$ 3 Myr. Our age measurement is consistent with Bell et al. (2015).

It is much older than the age found by Booth et al. (2021). That age was largely based on the inclusion of a single high-mass star, HD 95086, in the membership of Carina. That star is actually a member of a newly-found association, MELANGE-4 (Wood et al., 2023).

Our measurement is about twice the age found by Schneider et al. (2019) using a compilation of Li measurements. They found that the Li sequence of Carina more closely resembled the Li sequence of β Pic ($\sim$ 21 Myr) than that of Tuc-Hor ($\sim$ 45 Myr). The differentiation between those two ages comes largely from three stars with spectral type M0 and $EW(Li)$ =350–400 mÅ, higher than expected for a 40 Myr old star of that spectral type. Two of those three stars are included in the membership list we use here. Our age is based on Li measurements in fully convective low-mass stars, a region which has less scatter than earlier spectral types. Our additional Li measurements in stars of type M3 and later make clear that the LDB for Carina, shown in Figures 4.3 and 4.4, is at a higher magnitude than that for β Pic. If Carina were the same age as β Pic, we would expect the three observed stars with $6.0 < M_{K_S} < 6.5$ to be Li-rich, and the partially depleted stars at $6.5 < M_{K_S} < 7.0$ not to be depleted at all. This discrepancy emphasizes the utility of the LDB method, which is less sensitive to changes in evolutionary model operates in a stellar regime with less scatter in Li abundances.

The age we find here is consistent with the age of the nearby Tuc-Hor association (Kraus et al., 2014), lending support to the theory that the three groups form a complex as suggested by earlier and more recent worrk (e.g., Kerr et al., 2021). Other potentially related groups include Theia 92, Theia 113 and Platais 8 (Gagné et al., 2021). Measuring ages for those other groups to determine if they have consistent ages is an important next step.

If these groups, or a subset of them, are related then this structure could be an older remnant of a Sco-Cen-like complex. Historically, older regions have been much harder to study because associations spread out as they age and galactic forces pull them apart. This

has prevented the identification and study of older complexes — the only two well-studied complexes are both less than 20 Myr old. If so this complex can reveal new insight into star formation and molecular cloud collapse mechanisms as well as to the stages of stellar and planetary evolution between 20–100 Myr.

5.2 Future Outlook

In this dissertation I have focused on measuring the ages of associations using the Lithium Depletion Boundary method. While LDB can provide highly accurate and precise ages, it requires significant observational resources and cannot be used to measure the ages of very young ($\lesssim$ 15 Myr) or older ($\gtrsim$ 200 Myr) associations.

Thus, to create a well-calibrated age scale for stellar associations it is necessary to combine multiple methods, applying the advantages of each. By systematically applying several age-measurement methods and comparing the results, we can determine how well age measurements produced by each agree across a range of stellar masses and properties. Doing so will allow future researchers to choose an age method which is most accurate at the estimated age of their association or the best stellar types to use within a specific dataset, thus improving the accuracy of future age measurements. Calibrating these methods will also improve their accuracy when applied to single field stars.

In the final section I outline future research combining five age-measurement methods to first fully map the age sequence of the Scorpius-Centaurus Association, and then to apply broadly to stellar associations within 200 pc of the Sun.

5.2.1 A Definitive Age Sequence for the Scorpius-Centaurus Complex

Containing the youngest transiting planet (K2-33 b; David et al., 2016; Mann et al., 2016a), the youngest hot Jupiter (HIP 67522 b; Rizzuto et al., 2020), hundreds of circumstellar disks (Luhman, 2018), and thousands of stars, the Scorpius-Centaurus complex is integral to our understanding of circumstellar disks, planet formation and migration. It has

also revolutionized our understanding of stellar associations, as recent research has discovered greater structure (Goldman et al., 2018; Kerr et al., 2021), larger age differentiation, and a more complex star-formation history (Pecaut & Mamajek, 2016) than previously thought possible. Given this region's importance to the study of planetary evolution and associations, it is necessary to gain a greater understanding of the structure, formation history, and age variation in Sco-Cen. By expanding on my prior work characterizing new and previously known populations around Sco-Cen (Chapters 2,3 Mann et al., 2022; Wood et al., 2023), and building new collaborations with other researchers I will characterize the sub-populations of Sco-Cen and robustly measure their ages. During this project I will develop and improve the methods needed to clarify the membership and determine the ages of stellar populations, which I will later apply to a large number of other association complexes.

Clarifying the extent and membership of subpopulations is an important first step, as mixing members between populations will pollute any measurements of their properties. Machine learning methods have been successfully used to locate populations and enumerate their members (e.g., Kounkel & Covey, 2019; Kerr et al., 2021), but these methods can miss important populations, such as MELANGE-4, which despite being on the outskirts of LCC had not been found by any survey of the region. Other methods of locating association members, such as `BANYAN` Σ (Malo et al., 2014; Gagné et al., 2018), include assumptions about the structure which may not be valid for all associations. The multi-variate Gaussian shape assumed by `BANYAN` Σ does not describe associations with non-traditional structures like Pisces-Eridanus or Phlegethon (Meingast et al., 2019; Ibata et al., 2018) and will not accurately identify their members. The solution which I proposed in (Wood et al., 2023) is to use an iterative membership search relying alternately on kinematic information and indicators of youth such as CMD position or rotation. By alternating between kinematic and age-based indicators of membership, the resulting list is balanced between inclusion of members (found through kinematic searches) and exclusion of interlopers (removed by age indicators). The outline of the method is:

1. Identify an initial membership list. For the subpopulations of Sco-Cen I will compile membership lists from literature searches (e.g., Pecaut & Mamajek, 2016; Luhman, 2018; Damiani et al., 2019; Kerr et al., 2021).

2. Apply cuts to the initial membership list using quality of data measures (e.g., Gaia RUWE), CMD position, and rotation.

3. Define the kinematic extent of the group for a 6D kinematic search. Wood et al. (2023) used `BANYAN` Σ for this step, but alterations may be needed for populations with non-Gaussian structure.

4. Reapply CMD cut to remove kinematic interlopers added back in by the kinematic search.

While this method was successful in distinguishing members of MELANGE-4 (27 ± 3 Myr) from those of LCC subpopulations (10–15 Myr), it will be more difficult to distinguish between subpopulations that are closer in age, as both kinematic and age-based indicators will be less likely to catch interlopers from neighboring subpopulations. This technique will therefore need to be improved and expanded on to account for such situations. By applying it to more populations I will gain greater insight and make the necessary improvements.

Once a membership list of each subpopulation has been established, I will measure its age using a combination of CMD fitting, LDB, empirical Li sequencing, gyrochronology, and kinematic traceback.

To reduce the effect of binary stars and interlopers on the CMD fitting age, I will use a Gaussian Mixture Model (GMM). A GMM fits the age of the association assuming that it is a mix of multiple populations. In Mann et al. (2022) we used a GMM to measure the age of the Musca association, assuming that the membership list was composed of a population of "true members" and a population of "outliers". True binary members were considered outliers to avoid age bias. I will improve this method to include three populations of stars: true single members, field interlopers, and true binary members —- expected to lie high

on the CMD and thus distinguishable from field interlopers. Doing so will produce a more complete membership list and more accurate measure of the contamination fraction.

After getting an initial age measurement using CMD fitting, I will locate the lithium depletion boundary by obtaining medium- to high-resolution optical spectra of low-mass association members. Extensive prior research on the Sco-Cen region will reduce the need for new observations, as many known members have existing archival spectra. I will calculate the Li abundance of each member by measuring the equivalent width of the 6708 Å Li line to identify the brightest Li-rich star and the faintest Li-poor star, which define the LDB. By comparing the magnitude of the LDB edges to stellar evolutionary models, I will convert the LDB into an age estimate. For this I will use a variety of evolutionary models, including standard models (Baraffe et al., 2015; Dotter et al., 2008), magnetic models (Feiden, 2016), and ones which allow for varying amounts of stellar spot coverage (Somers et al., 2020).

To supplement the LDB ages, or as an alternative method for populations < 15 Myr old, I will also empirically determine the age by comparison of the population Li sequence to those of benchmark associations and evolutionary models. As this looks at all spectral types, I will supplement the spectra of low mass members needed for LDB with those of G–K dwarfs. I expect that few new observations will be needed, as high-mass members of Sco-Cen in particular have abundant archival data available. Although this method cannot produce absolute age estimates, by comparing the Li sequence of each subpopulation against other Sco-Cen subpopulations and benchmark associations, I will establish an age sequence.

Next, I will find the rotation sequence of each population. Stellar rotation sequences are not well defined at such young ages, but it is possible that mixing between subpopulations in previous studies confounded the results and that by more vigorously dividing the region into its subpopulations, a more coherent picture of stellar rotation evolution at young ages will emerge. I will obtain rotation periods for members from a combination of literature values, (e.g., Rebull et al., 2022), and from established and new collaboration with researchers working on measuring stellar rotation from lightcurves.

Lastly, I will investigate the accuracy of kinematic traceback — an age-dating method which relies on estimating the time in the past when an association was least disperse. To do so, I will need very precise 6D kinematic information for a majority of stars within a population. Gaia DR3 will provide most of this, with nearly complete position and proper-motion measurements for stars within 200 pc, and a greatly expanded sample of RV measurements. Spectra taken for the Li analysis above will provide additional RVs. By marginalizing over RV using the technique from Angus et al. (2022), I will estimate 3D velocities for stars without Gaia RVs or spectra. I will use two different methods to perform the traceback, comparing the results between them and the other age-determination methods. First is GalPy, a galactic dynamics package used to model orbital motion through the galactic potential (Bovy, 2015; Kounkel et al., 2022a; Miret-Roig et al., 2018). A more sophisticated treatment is given by Chronostar, a Bayesian framework for kinematic age calculation (Crundall et al., 2019). Application of Chronostar to the β Pic and Tuc-Hor associations recovered ages which, while still younger than the accepted LDB ages, are much closer than any previous kinematic traceback method (Crundall et al., 2019) (see Figure 1.1 for a comparison). Chronostar is also able to determine membership, which I will compare against the membership lists that developed through my iterative method.

The final steps are to compare and combine the results from each method to determine a final age for each subpopulation, and to compare the ages of each subpopulation to determine the overall formation sequence of the complex. Of the five methods, four of them can be applied to a broad range of spectral classes, allowing the ages to be compared across the full mass range. I will be able to determine if any of the methods have systematic errors causing different spectral classes to produce different age estimates, and will be able to compare the results at different masses between methods. By comparing the scatter in each method I will also be able to determine if scatter in the results is present only for some methods, and thus likely to be caused by scatter in observable parameters or if it is present in all methods, and thus likely caused by actual age variation within the populations. For the final age

determination, the results from each of the methods will be combined, with attention to the uncertainty intrinsic to each method and model used. This will result in ages which are significantly more accurate than those produced by any single method, and which have uncertainties representing the true age uncertainty.

5.2.2 An Age Survey of all Young Association Complexes within 200 pc

While much effort has been expended studying very young (< 20 Myr) stellar complexes, like Sco-Cen, older stellar complexes have been historically neglected due to their high dispersion across the sky and the necessity of extremely precise kinematic information to determine their membership. It is possible that many such complexes exist, but have been identified only as their individual components. Recent research suggests that many larger associations may in fact be linked together by smaller, lesser-known groups, together forming huge complexes of nearly coeval groups (Gagné et al., 2021). Many associations have either recently been discovered (e.g., Kounkel & Covey, 2019) or have never been comprehensively studied, and lack clear age estimates which could tell us if they are coeval with other nearby associations. I will apply the four age-determination methods discussed above to nearby (< 200 pc) young association complexes in order to determine their ages and relationships to each other, and to calibrate age measurement methods on ages > 20 Myr.

Prior to measuring their ages, association complexes must be identified. Research identifying stellar associations has been ongoing for well over 50 years (e.g., Platais et al., 1998), and new methods and telescopes in the last decade have dramatically expanded this effort (e.g., Kounkel & Covey, 2019; Kerr et al., 2021), so that we now know of hundreds of associations near the Sun. Different studies have used a variety of methods to identify associations, often using different coordinate systems (i.e., RA/Dec, l/b, or X/Y/Z). Inconsistency in identification techniques and terminology means that a single population may have been identified by multiple studies at different times, and thus may have several names assigned to it. Combined with the tendency of researchers to use different names for what is known

to be the same association (e.g., Meingast-1 a.k.a. Pisces-Eridanus; Meingast et al., 2019; Curtis et al., 2019), it can be nearly impossible to keep track of all nearby associations. To reduce this confusion and establish a starting point for identifying association complexes, I will compile a catalog of nearby stellar associations and publish it online. By organizing a list of associations and recalculating the positions and extents of each in a consistent coordinate system (galactic X, Y, and Z), I will determine which populations have been doubly defined and which are neighboring.

Next, to identify candidate association complexes to study, I will locate neighboring associations with similar ages. This will include both previously suggested association complexes and new potential complexes. I will identify new potential complexes by fitting CMD uniformly on all associations within 200 pc. Neighboring groups with similar ages ($< 20\%$ difference), will be considered potential complexes and will be studied further. Once subjects for study have been identified, I will measure their ages using the age-determination techniques which I developed during the first project. In applying age-determination methods to this much larger sample of associations I will explore their use on a greatly expanded range of stellar properties, including age, metallicity, and formation history, and further calibrate them for use on a broader group of stars. Finally, I will use the measured ages to evaluate the candidate complexes and determine the relationship between the component associations.

BIBLIOGRAPHY

Adibekyan, V., Figueira, P., Santos, N. C., et al. 2015, Astronomy& Astrophysics, 583, A94, doi: 10.1051/0004-6361/201527120

Adibekyan, V. Z., Sousa, S. G., Santos, N. C., et al. 2012, Astronomy& Astrophysics, 545, A32, doi: 10.1051/0004-6361/201219401

Aller, A., Lillo-Box, J., Jones, D., Miranda, L. F., & Barceló Forteza, S. 2020, Astronomy& Astrophysics, 635, A128, doi: 10.1051/0004-6361/201937118

Andrews, J. J., Curtis, J. L., Chanamé, J., et al. 2022, The Astronomical Journal, 163, 275, doi: 10.3847/1538-3881/ac6952

Angus, R., Price-Whelan, A. M., Zinn, J. C., et al. 2022, The Astronomical Journal, 164, 25, doi: 10.3847/1538-3881/ac6fea

Asplund, M., Grevesse, N., Sauval, A. J., & Scott, P. 2009, Annual Review of Astronomy and Astrophysics, 47, 481, doi: 10.1146/annurev.astro.46.060407.145222

Baraffe, I., & Chabrier, G. 2010, Astronomy & Astrophysics, 521, A44, doi: 10.1051/0004-6361/201014979

Baraffe, I., Elbakyan, V. G., Vorobyov, E. I., & Chabrier, G. 2017, Astronomy & Astrophysics, 597, A19, doi: 10.1051/0004-6361/201629303

Baraffe, I., Homeier, D., Allard, F., & Chabrier, G. 2015, Astronomy & Astrophysics, 577, A42, doi: 10.1051/0004-6361/201425481

Barber, M. G., & Mann, A. W. 2023, Using Gaia excess uncertainty as a proxy for stellar variability and age, arXiv, doi: 10.48550/arXiv.2302.09084

Barber, M. G., Mann, A. W., Bush, J. L., et al. 2022, arXiv e-prints, arXiv:2206.08383

Barnes, S. A. 2003, The Astrophysical Journal, 586, 464, doi: 10.1086/367639

Barragán, O., Aigrain, S., Kubyshkina, D., et al. 2019, Monthly Notices of the Royal Astronomical Society, 490, 698, doi: 10.1093/mnras/stz2569

Bell, C. P. M., Mamajek, E. E., & Naylor, T. 2015, Monthly Notices of the Royal Astronomical Society, 454, 593, doi: 10.1093/mnras/stv1981

Belokurov, V., Penoyre, Z., Oh, S., et al. 2020, Monthly Notices of the Royal Astronomical Society, 496, 1922, doi: 10.1093/mnras/staa1522

Benatti, S., Nardiello, D., Malavolta, L., et al. 2019, arXiv:1904.01591 [astro-ph]. http://arxiv.org/abs/1904.01591

Berger, T. A., Huber, D., Gaidos, E., Saders, J. L. v., & Weiss, L. M. 2020, The Astronomical Journal, 160, 108, doi: 10.3847/1538-3881/aba18a

Berta, Z. K., Irwin, J., & Charbonneau, D. 2013, Astrophysical Journal, 775, 91, doi: 10.1088/0004-637X/775/2/91

Binks, A. S., & Jeffries, R. D. 2014, Monthly Notices of the Royal Astronomical Society: Letters, 438, L11, doi: 10.1093/mnrasl/slt141

Binks, A. S., Jeffries, R. D., Jackson, R. J., et al. 2021, Monthly Notices of the Royal Astronomical Society, 505, 1280, doi: 10.1093/mnras/stab1351

Binks, A. S., Jeffries, R. D., Sacco, G. G., et al. 2022, Monthly Notices of the Royal Astronomical Society, 513, 5727, doi: 10.1093/mnras/stac1245

Bochanski, J. J., West, A. A., Hawley, S. L., & Covey, K. R. 2007, The Astronomical Journal, 133, 531, doi: 10.1086/510240

Bohn, A. J., Kenworthy, M. A., Ginski, C., et al. 2020a, Monthly Notices of the Royal Astronomical Society, 492, 431, doi: 10.1093/mnras/stz3462

—. 2020b, The Astrophysical Journal, 898, L16, doi: 10.3847/2041-8213/aba27e

Bohn, A. J., Ginski, C., Kenworthy, M. A., et al. 2021, Astronomy & Astrophysics, 648, A73, doi: 10.1051/0004-6361/202140508

Bonfils, X., Delfosse, X., Udry, S., et al. 2013, Astronomy & Astrophysics, 549, A109, doi: 10.1051/0004-6361/201014704

Booth, M., del Burgo, C., & Hambaryan, V. V. 2021, Monthly Notices of the Royal Astronomical Society, 500, 5552, doi: 10.1093/mnras/staa3631

Bouma, L. G., Hartman, J. D., Brahm, R., et al. 2020, The Astronomical Journal, 160, 239, doi: 10.3847/1538-3881/abb9ab

Bouma, L. G., Kerr, R., Curtis, J. L., et al. 2022, arXiv e-prints, arXiv:2205.01112. https://arxiv.org/abs/2205.01112

Bouvier, J., Barrado, D., Moraux, E., et al. 2018, Astronomy & Astrophysics, 613, A63, doi: 10.1051/0004-6361/201731881

Bovy, J. 2015, The Astrophysical Journal Supplement Series, 216, 29, doi: 10.1088/0067-0049/216/2/29

Bressan, A., Marigo, P., Girardi, L., et al. 2012, Monthly Notices of the Royal Astronomical Society, 427, 127, doi: 10.1111/j.1365-2966.2012.21948.x

Buchhave, L. A., Latham, D. W., Johansen, A., et al. 2012, Nature, 486, 375, doi: 10.1038/nature11121

Burke, C. J., Pinsonneault, M. H., & Sills, A. 2004, The Astrophysical Journal, 604, 272, doi: 10.1086/381242

Cale, B., Reefe, M., Plavchan, P., et al. 2021, arXiv e-prints, arXiv:2109.13996. https://arxiv.org/abs/2109.13996

Campante, T. L., Lund, M. N., Kuszlewicz, J. S., et al. 2016, The Astrophysical Journal, 819, 85, doi: 10.3847/0004-637x/819/1/85

Cao, L., Pinsonneault, M. H., Hillenbrand, L. A., & Kuhn, M. A. 2022, The Astrophysical Journal, 924, 84, doi: 10.3847/1538-4357/ac307f

Cardelli, J. A., Clayton, G. C., & Mathis, J. S. 1989, The Astrophysical Journal, 345, 245, doi: 10.1086/167900

Carleo, I., Desidera, S., Nardiello, D., et al. 2021, Astronomy & Astrophysics, 645, A71, doi: 10.1051/0004-6361/202039042

Castelli, F., & Kurucz, R. L. 2004, ArXiv Astrophysics e-prints

Chabrier, G., Baraffe, I., & Plez, B. 1996, The Astrophysical Journal, 459, doi: 10.1086/309951

Clemens, J. C., Crain, J. A., & Anderson, R. 2004, in Society of Photo-Optical Instrumentation Engineers (SPIE) Conference Series, Vol. 5492, Ground-based Instrumentation for Astronomy, ed. A. F. M. Moorwood & M. Iye, 331–340, doi: 10.1117/12.550069

Costa Silva, A. R., Delgado Mena, E., & Tsantaki, M. 2020, Astronomy& Astrophysics, 634, A136, doi: 10.1051/0004-6361/201936523

Crundall, T. D., Ireland, M. J., Krumholz, M. R., et al. 2019, Monthly Notices of the Royal Astronomical Society, 489, 3625, doi: 10.1093/mnras/stz2376

Currie, T., Biller, B., Lagrange, A.-M., et al. 2022, arXiv e-prints, arXiv:2205.05696. https://arxiv.org/abs/2205.05696

Curtis, J. L., Agüeros, M. A., Mamajek, E. E., Wright, J. T., & Cummings, J. D. 2019, The Astronomical Journal, 158, 77, doi: 10.3847/1538-3881/ab2899

Curtis, J. L., Wolfgang, A., Wright, J. T., Brewer, J. M., & Johnson, J. A. 2013, The Astronomical Journal, 145, 134, doi: 10.1088/0004-6256/145/5/134

Curtis, J. L., Agüeros, M. A., Matt, S. P., et al. 2020, The Astrophysical Journal, 904, 40pp, doi: 10.3847/1538-4357/abbf58

da Silva, L., Torres, C. A. O., de La Reza, R., et al. 2009, Astronomy& Astrophysics, 508, 833, doi: 10.1051/0004-6361/200911736

Damasso, M., Lanza, A. F., Benatti, S., et al. 2020, Astronomy& Astrophysics, 642, A133, doi: 10.1051/0004-6361/202038864

Damiani, F., Prisinzano, L., Pillitteri, I., Micela, G., & Sciortino, S. 2019, Astronomy & Astrophysics, 623, A112, doi: 10.1051/0004-6361/201833994

David, T. J., Petigura, E. A., Luger, R., et al. 2019, Astrophysical Journal Letters, 885, L12, doi: 10.3847/2041-8213/ab4c99

David, T. J., Hillenbrand, L. A., Petigura, E. A., et al. 2016, Nature, 534, 658, doi: 10.1038/nature18293

Dawson, R. I., & Johnson, J. A. 2018, Annual Review of Astronomy and Astrophysics, 56, 175, doi: 10.1146/annurev-astro-081817-051853

de Rosa, R. J., Rameau, J., Patience, J., et al. 2016, The Astrophysical Journal, 824, 121, doi: 10.3847/0004-637X/824/2/121

de Zeeuw, P. T., Hoogerwerf, R., Bruijne, J. H. J. d., Brown, A. G. A., & Blaauw, A. 1999, The Astronomical Journal, 117, 354, doi: 10.1086/300682

Dickson-Vandervelde, D. A., Wilson, E. C., & Kastner, J. H. 2021, The Astronomical Journal, 161, 87, doi: 10.3847/1538-3881/abd0fd

Dobbie, P. D., Lodieu, N., & Sharp, R. G. 2010, Monthly Notices of the Royal Astronomical Society, 409, 1002, doi: 10.1111/j.1365-2966.2010.17355.x

Donati, J.-F., Semel, M., Carter, B. D., Rees, D. E., & Collier Cameron, A. 1997, MNRAS, 291, 658, doi: 10.1093/mnras/291.4.658

Donati, J. F., Moutou, C., Malo, L., et al. 2016, Nature, 534, 662, doi: 10.1038/nature18305

Donati, J. F., Bouvier, J., Alencar, S. H., et al. 2020, MNRAS, 491, 5660, doi: 10.1093/mnras/stz3368

Dotter, A., Chaboyer, B., Jevremović, D., et al. 2008, The Astrophysical Journal Supplement Series, 178, 89, doi: 10.1086/589654

Doyle, A. P., Davies, G. R., Smalley, B., Chaplin, W. J., & Elsworth, Y. 2014, MNRAS, 444, 3592, doi: 10.1093/mnras/stu1692

Durisen, R. H., Boss, A. P., Mayer, L., et al. 2007, in Protostars and Planets V, ed. B. Reipurth, D. Jewitt, & K. Keil, 607, doi: 10.48550/arXiv.astro-ph/0603179

Espinoza, N., & Jordán, A. 2015, MNRAS, 450, 1879, doi: 10.1093/mnras/stv744

Fabrycky, D. C., & Winn, J. N. 2009, Astrophysical Journal, 696, 1230, doi: 10.1088/0004-637X/696/2/1230

Feiden, G. A. 2016, Astronomy & Astrophysics, 593, A99, doi: 10.1051/0004-6361/201527613

Feiden, G. A., & Chaboyer, B. 2013, The Astrophysical Journal, 779, 183, doi: 10.1088/0004-637X/779/2/183

Feinstein, A. D., David, T. J., Montet, B. T., et al. 2022, The Astrophysical Journal, 925, L2, doi: 10.3847/2041-8213/ac4745

Fernández, D., Figueras, F., & Torra, J. 2008, Astronomy and Astrophysics, 480, 735, doi: 10.1051/0004-6361:20077720

Foreman-Mackey, D., Agol, E., Ambikasaran, S., & Angus, R. 2017, The Astronomical Journal, 154, 220, doi: 10.3847/1538-3881/aa9332

Foreman-Mackey, D., Hogg, D. W., Lang, D., & Goodman, J. 2013, Publications of the Astronomical Society of the Pacific, 125, 306, doi: 10.1086/670067

Freund, S., Czesla, S., Robrade, J., Schneider, P. C., & Schmitt, J. H. M. M. 2022, Astronomy & Astrophysics, 664, A105, doi: 10.1051/0004-6361/202142573

Gagné, J., David, T. J., Mamajek, E. E., et al. 2020, The Astrophysical Journal, 903, 96, doi: 10.3847/1538-4357/abb77e

Gagné, J., Faherty, J. K., Moranta, L., & Popinchalk, M. 2021, The Astrophysical Journal Letters, 915, L29, doi: 10.3847/2041-8213/ac0e9a

Gagné, J., Mamajek, E. E., Malo, L., et al. 2018, The Astrophysical Journal, 856, 23, doi: 10.3847/1538-4357/aaae09

Gaia Collaboration, Prusti, T., Bruijne, J. H. J. d., et al. 2016, Astronomy & Astrophysics, 595, A1, doi: 10.1051/0004-6361/201629272

Gaia Collaboration, Brown, A. G. A., Vallenari, A., et al. 2021, Astronomy & Astrophysics, 649, A1, doi: 10.1051/0004-6361/202039657

Gaia Collaboration, Vallenari, A., Brown, A. G. A., & Prusti, T. 2022, Astronomy & Astrophysics, doi: 10.1051/0004-6361/202243940

Gaidos, E., & Mann, A. W. 2014, The Astrophysical Journal, 791, 54, doi: 10.1088/0004-637X/791/1/54

Gaidos, E., Mann, A. W., Rojas-Ayala, B., et al. 2022, Monthly Notices of the Royal Astronomical Society, 514, 1386, doi: 10.1093/mnras/stac1433

Giacalone, S., Dressing, C. D., Jensen, E. L. N., et al. 2021, The Astronomical Journal, 161, 24, doi: 10.3847/1538-3881/abc6af

Gillen, E., Hillenbrand, L. A., David, T. J., et al. 2017, The Astrophysical Journal, 849, 11, doi: 10.3847/1538-4357/aa84b3

Goldman, B., Röser, S., Schilbach, E., Moór, A. C., & Henning, T. 2018, The Astrophysical Journal, 868, 32, doi: 10.3847/1538-4357/aae64c

Gray, R. O., & Corbally, C. J. 1994, The Astronomical Journal, 107, 742, doi: 10.1086/116893

Grevesse, N., & Sauval, A. 1998, Space Science Reviews, 85, 161, doi: 10.1023/A:1005161325181

Guerrero, N. M., Seager, S., Huang, C. X., et al. 2021, The Astrophysical Journals, 254, 39, doi: 10.3847/1538-4365/abefe1

Gully-Santiago, M. A., Herczeg, G. J., Czekala, I., et al. 2017, The Astrophysical Journal, 836, 200

Gupta, A., & Schlichting, H. E. 2019, Monthly Notices of the Royal Astronomical Society, 487, 24, doi: 10.1093/mnras/stz1230

Gutiérrez Albarrán, M. L., Montes, D., Gómez Garrido, M., et al. 2020, Astronomy& Astrophysics, 643, A71, doi: 10.1051/0004-6361/202037620

Hardegree-Ullman, K. K., Cushing, M. C., Muirhead, P. S., & Christiansen, J. L. 2019, Astronomical Journal, 158, 75, doi: 10.3847/1538-3881/ab21d2

Hattori, S., Foreman-Mackey, D., Hogg, D. W., et al. 2021, arXiv e-prints, arXiv:2106.15063. https://arxiv.org/abs/2106.15063

Heap, S. R., & Lindler, D. 2016, in Astronomical Society of the Pacific Conference Series, Vol. 503, The Science of Calibration, ed. S. Deustua, S. Allam, D. Tucker, & J. A. Smith, 211

Helmi, A. 2020, Annual Review of Astronomy and Astrophysics, 58, 205, doi: 10.1146/annurev-astro-032620-021917

Hinkley, S., Pueyo, L., Faherty, J. K., et al. 2013, The Astrophysical Journal, 779, 153, doi: 10.1088/0004-637X/779/2/153

Hinkley, S., Kraus, A. L., Ireland, M. J., et al. 2015, The Astrophysical Journall, 806, L9, doi: 10.1088/2041-8205/806/1/L9

Høg, E., Fabricius, C., Makarov, V. V., et al. 2000, Astronomy & Astrophysics, 355, L27

Hogg, D. W., Bovy, J., & Lang, D. 2010, Data analysis recipes: Fitting a model to data, Tech. Rep. arXiv:1008.4686, arXiv, doi: 10.48550/arXiv.1008.4686

Horne, K. 1986, Publications of the Astronomical Society of the Pacific, 98, 609, doi: 10.1086/131801

Howell, S. B., Everett, M. E., Sherry, W., Horch, E., & Ciardi, D. R. 2011, The Astronomical Journal, 142, 19, doi: 10.1088/0004-6256/142/1/19

Hsieh, C.-H., Laughlin, G., & Arce, H. G. 2021, The Astrophysical Journal, 917, 20, doi: 10.3847/1538-4357/ac0729

Huang, C. X., Vanderburg, A., Pál, A., et al. 2020, Research Notes of the American Astronomical Society, 4, 204, doi: 10.3847/2515-5172/abca2e

Husser, T.-O., von Berg, S. W., Dreizler, S., et al. 2013, Astronomy & Astrophysics, 553, A6, doi: 10.1051/0004-6361/201219058

Ibata, R. A., Malhan, K., Martin, N. F., & Starkenburg, E. 2018, The Astrophysical Journal, 865, 85, doi: 10.3847/1538-4357/aadba3

Jackson, R. J., & Jeffries, R. D. 2014, Monthly Notices of the Royal Astronomical Society, 445, 4306, doi: 10.1093/mnras/stu2076

Jenkins, J. M. 2002a, The Astrophysical Journal, 575, 493, doi: 10.1086/341136

—. 2002b, The Astrophysical Journal, 575, 493, doi: 10.1086/341136

Jenkins, J. M., Tenenbaum, P., Seader, S., et al. 2020, Kepler Data Processing Handbook: Transiting Planet Search, Kepler Science Document KSCI-19081-003, id. 9. Edited by Jon M. Jenkins.

Jenkins, J. M., Chandrasekaran, H., McCauliff, S. D., et al. 2010, in Society of Photo-Optical Instrumentation Engineers (SPIE) Conference Series, Vol. 7740, Software and Cyberinfrastructure for Astronomy, ed. N. M. Radziwill & A. Bridger, 77400D, doi: 10.1117/12.856764

Jenkins, J. M., Twicken, J. D., McCauliff, S., et al. 2016, in Society of Photo-Optical Instrumentation Engineers (SPIE) Conference Series, Vol. 9913, Software and Cyberinfrastructure for Astronomy IV, ed. G. Chiozzi & J. C. Guzman, 99133E, doi: 10.1117/12.2233418

Johns-Krull, C. M., McLane, J. N., Prato, L., et al. 2016, Astrophysical Journal, 826, 206, doi: 10.3847/0004-637X/826/2/206

Johnson, M. C., Dai, F., Justesen, A. B., et al. 2018, Monthly Notices of the Royal Astronomical Society, 481, 596, doi: 10.1093/mnras/sty2238

Kapteyn, J. C. 1914, The Astrophysical Journal, 40, 43, doi: 10.1086/142098

Kerr, R. M. P., Rizzuto, A. C., Kraus, A. L., & Offner, S. S. R. 2021, The Astrophysical Journal, 917, 23, doi: 10.3847/1538-4357/ac0251

Kesseli, A. Y., West, A. A., Veyette, M., et al. 2017, The Astrophysical Journal Supplements, 230, 16, doi: 10.3847/1538-4365/aa656d

Kiman, R., Faherty, J. K., Cruz, K. L., et al. 2021, arXiv:2104.01232 [astro-ph]. http://arxiv.org/abs/2104.01232

Kipping, D. M. 2013, MNRAS, 435, 2152, doi: 10.1093/mnras/stt1435

Klein, B., Donati, J.-F., Moutou, C., et al. 2021, MNRAS, 502, 188, doi: 10.1093/mnras/staa3702

Klein, B., Zicher, N., Kavanagh, R. D., et al. 2022, MNRAS, 512, 5067, doi: 10.1093/mnras/stac761

Kounkel, M., & Covey, K. 2019, The Astronomical Journal, 158, 122, doi: 10.3847/1538-3881/ab339a

Kounkel, M., Deng, T., & Stassun, K. G. 2022a, The Astronomical Journal, 164, 57, doi: 10.3847/1538-3881/ac7951

Kounkel, M., Stassun, K. G., Bouma, L. G., et al. 2022b, The Astronomical Journal, 164, 137, doi: 10.3847/1538-3881/ac866d

Kounkel, M., Covey, K., Moe, M., et al. 2019, The Astronomical Journal, 157, 196, doi: 10.3847/1538-3881/ab13b1

Kraus, A. L., Herczeg, G. J., Rizzuto, A. C., et al. 2017, The Astrophysical Journal, 838, 150, doi: 10.3847/1538-4357/aa62a0

Kraus, A. L., Shkolnik, E. L., Allers, K. N., & Liu, M. C. 2014, The Astronomical Journal, 147, 146, doi: 10.1088/0004-6256/147/6/146

Kreidberg, L. 2015, Publications of the Astronomical Society of the Pacific, 127, 1161, doi: 10.1086/683602

Krolikowski, D. M., Kraus, A. L., & Rizzuto, A. C. 2021, arXiv:2105.13370 [astro-ph]. http://arxiv.org/abs/2105.13370

Kurucz, R. L. 1993, International Astronomical Union Colloquium, 138, 87, doi: 10.1017/S0252921100020327

Kurucz, R. L. 1993, SYNTHE spectrum synthesis programs and line data (Smithsonian Astrophysical Observatory)

Lazzoni, C., Desidera, S., Gratton, R., et al. 2022, Monthly Notices of the Royal Astronomical Society, 516, 391, doi: 10.1093/mnras/stac2081

Leiner, E. M., Mathieu, R. D., Gosnell, N. M., & Geller, A. M. 2015, The Astronomical Journal, 150, 10, doi: 10.1088/0004-6256/150/1/10

Li, J., Tenenbaum, P., Twicken, J. D., et al. 2019, Proceedings of the Astronomical Society of the Pacific, 131, 024506, doi: 10.1088/1538-3873/aaf44d

Lim, P. L. 2020, doi: 10.5281/zenodo.3971036

Lindegren, L., Klioner, S. A., Hernández, J., et al. 2021, Astronomy & Astrophysics, 649, A2, doi: 10.1051/0004-6361/202039709

Linsky, J. L. 2017, Annual Review of Astronomy and Astrophysics, 55, 159, doi: 10.1146/annurev-astro-091916-055327

Lissauer, J. J., Marcy, G. W., Rowe, J. F., et al. 2012, The Astrophysical Journal, 750, 112, doi: 10.1088/0004-637X/750/2/112

Lomb, N. R. 1976, Astrophysics and Space Science, 39, 447, doi: 10.1007/BF00648343

Lucy, L. B., & Ricco, E. 1979, The Astronomical Journal, 84, 401, doi: 10.1086/112434

Luhman, K. L. 2018, The Astronomical Journal, 156, 271, doi: 10.3847/1538-3881/aae831

Madsen, S., Dravins, D., & Lindegren, L. 2002, Astronomy& Astrophysics, 381, 446, doi: 10.1051/0004-6361:20011458

Malo, L., Artigau, É., Doyon, R., et al. 2014, The Astrophysical Journal, 788, 81, doi: 10.1088/0004-637X/788/1/81

Malo, L., Doyon, R., Lafrenière, D., et al. 2012, The Astrophysical Journal, 762, 88, doi: 10.1088/0004-637X/762/2/88

Mamajek, E. E., & Bell, C. P. M. 2014, Monthly Notices of the Royal Astronomical Society, 445, 2169, doi: 10.1093/mnras/stu1894

Mamajek, E. E., Meyer, M. R., & Liebert, J. 2002, The Astronomical Journal, 124, 1670, doi: 10.1086/341952

Mann, A. W., Newton, E. R., Rizzuto, A. C., et al. 2016a, The Astronomical Journal, 152, 61, doi: 10.3847/0004-6256/152/3/61

Mann, A. W., Gaidos, E., Mace, G. N., et al. 2016b, The Astrophysical Journal, 818, 46, doi: 10.3847/0004-637X/818/1/46

Mann, A. W., Dupuy, T., Kraus, A. L., et al. 2019, The Astrophysical Journal, 871, 63, doi: 10.3847/1538-4357/aaf3bc

Mann, A. W., Johnson, M. C., Vanderburg, A., et al. 2020, The Astronomical Journal, 160, 179, doi: 10.3847/1538-3881/abae64

Mann, A. W., Wood, M. L., Schmidt, S. P., et al. 2022, The Astronomical Journal, 163, 156, doi: 10.3847/1538-3881/ac511d

Masuda, K., & Winn, J. N. 2020, The Astronomical Journal, 159, 81, doi: 10.3847/1538-3881/ab65be

Mayor, M., & Queloz, D. 1995, Nature, 378, 355, doi: 10.1038/378355a0

McInnes, L., & Healy, J. 2017, arXiv e-prints, arXiv:1705.07321. https://arxiv.org/abs/1705.07321

Meingast, S., Alves, J., & Fürnkranz, V. 2019, Astronomy & Astrophysics, 622, L13, doi: 10.1051/0004-6361/201834950

Mentuch, E., Brandeker, A., Kerkwijk, M. H. v., Jayawardhana, R., & Hauschildt, P. H. 2008, The Astrophysical Journal, 689, 1127, doi: 10.1086/592764

Messina, S., Nardiello, D., Desidera, S., et al. 2022, Astronomy& Astrophysics, 657, L3, doi: 10.1051/0004-6361/202142276

Miret-Roig, N., Antoja, T., Romero-Gómez, M., & Figueras, F. 2018, Astronomy & Astrophysics, 615, A51, doi: 10.1051/0004-6361/201731976

Miyakawa, K., Hirano, T., Sato, B., Okuzumi, S., & Gaidos, E. 2022, Color Dependence of the Transit Detectability for Young Active M-dwarfs, arXiv, doi: 10.48550/arXiv.2209.05765

Moór, A., Kóspál, Á., Ábrahám, P., et al. 2016, The Astrophysical Journal, 826, 123, doi: 10.3847/0004-637X/826/2/123

Moór, A., Ábrahám, P., Kóspál, Á., et al. 2013, The Astrophysical Journall, 775, L51, doi: 10.1088/2041-8205/775/2/L51

Mordasini, C., Alibert, Y., Benz, W., & Naef, D. 2008, in Astronomical Society of the Pacific Conference Series, Vol. 398, Extreme Solar Systems, ed. D. Fischer, F. A. Rasio, S. E. Thorsett, & A. Wolszczan, 235, doi: 10.48550/arXiv.0710.5667

Morton, T. D. 2015, isochrones: Stellar model grid package, Astrophysics Source Code Library, record ascl:1503.010. http://ascl.net/1503.010

Morton, T. D., Bryson, S. T., Coughlin, J. L., et al. 2016, The Astrophysical Journal, 822, 86, doi: 10.3847/0004-637X/822/2/86

Murphy, S. J., Lawson, W. A., & Bessell, M. S. 2013, Monthly Notices of the Royal Astronomical Society, 435, 1325, doi: 10.1093/mnras/stt1375

Murphy, S. J., Mamajek, E. E., & Bell, C. P. M. 2018, Monthly Notices of the Royal Astronomical Society, 476, 3290, doi: 10.1093/mnras/sty471

Newton, E. R., Irwin, J., Charbonneau, D., et al. 2016, The Astrophysical Journal, 821, 93, doi: 10.3847/0004-637X/821/2/93

Newton, E. R., Mann, A. W., Tofflemire, B. M., et al. 2019, The Astrophysical Journal, 880, L17, doi: 10.3847/2041-8213/ab2988

Newton, E. R., Mann, A. W., Kraus, A. L., et al. 2021, The Astronomical Journal, 161, 65, doi: 10.3847/1538-3881/abccc6

Newton, E. R., Rampalli, R., Kraus, A. L., et al. 2022, arXiv e-prints, arXiv:2206.06254. https://arxiv.org/abs/2206.06254

Nisak, A. H., White, R. J., Yep, A., et al. 2022, The Astronomical Journal, 163, 278, doi: 10.3847/1538-3881/ac63c3

Oh, S., Price-Whelan, A. M., Hogg, D. W., Morton, T. D., & Spergel, D. N. 2017, The Astronomical Journal, 153, 257, doi: 10.3847/1538-3881/aa6ffd

Owen, J. E. 2020, MNRAS, 498, 5030, doi: 10.1093/mnras/staa2784

Owen, J. E., & Wu, Y. 2017, The Astrophysics Journa, 847, 29, doi: 10.3847/1538-4357/aa890a

Parviainen, H., & Aigrain, S. 2015, Monthly Notices of the Royal Astronomical Society, 453, 3821, doi: 10.1093/mnras/stv1857

Pecaut, M. J., & Mamajek, E. E. 2013, The Astrophysical Journal Supplement Series, 208, 9, doi: 10.1088/0067-0049/208/1/9

—. 2016, Monthly Notices of the Royal Astronomical Society, 461, 794, doi: 10.1093/mnras/stw1300

Pecaut, M. J., Mamajek, E. E., & Bubar, E. J. 2012, The Astrophysical Journal, 746, 154, doi: 10.1088/0004-637X/746/2/154

Phillips, M. W., Tremblin, P., Baraffe, I., et al. 2020, Astronomy& Astrophysics, 637, A38, doi: 10.1051/0004-6361/201937381

Platais, I., Kozhurina-Platais, V., & Leeuwen, F. v. 1998, The Astronomical Journal, 116, 2423, doi: 10.1086/300606

Plavchan, P., Barclay, T., Gagné, J., et al. 2020, Nature, 582, 497, doi: 10.1038/s41586-020-2400-z

Poppenhaeger, K., Ketzer, L., & Mallonn, M. 2021, Monthly Notices of the Royal Astronomical Society, 500, 4560, doi: 10.1093/mnras/staa1462

Preibisch, T., & Mamajek, E. 2008, in Handbook of Star Forming Regions, Volume II, ed. B. Reipurth, Vol. 5 (Atlantic Society of the Pacific), 235

Press, W. H., & Rybicki, G. B. 1989, The Astrophysical Journal, 338, 277, doi: 10.1086/167197

Rameau, J., Chauvin, G., Lagrange, A.-M., et al. 2013, The Astrophysical Journal, 779, L26, doi: 10.1088/2041-8205/779/2/L26

Rampalli, R., Agüeros, M. A., Curtis, J. L., et al. 2021, The Astrophysical Journal, 921, 167, doi: 10.3847/1538-4357/ac0c1e

Randich, S., Tognelli, E., Jackson, R., et al. 2018, Astronomy & Astrophysics, 612, A99, doi: 10.1051/0004-6361/201731738

Rayner, J. T., Cushing, M. C., & Vacca, W. D. 2009, The Astrophysical Journal Supplement Series, 185, 289, doi: 10.1088/0067-0049/185/2/289

Rebull, L. M., Stauffer, J. R., Cody, A. M., et al. 2018, The Astronomical Journal, 155, 196, doi: 10.3847/1538-3881/aab605

Rebull, L. M., Stauffer, J. R., Hillenbrand, L. A., et al. 2022, The Astronomical Journal, 164, 80, doi: 10.3847/1538-3881/ac75f1

Ricker, G. R., Winn, J. N., Vanderspek, R., et al. 2015, Journal of Astronomical Telescopes, Instruments, and Systems, 1, 014003, doi: 10.1117/1.JATIS.1.1.014003

Riedel, A. R., Blunt, S. C., Lambrides, E. L., et al. 2017, The Astronomical Journal, 153, 95, doi: 10.3847/1538-3881/153/3/95

Riello, M., Angeli, F. D., Evans, D. W., et al. 2021, Astronomy & Astrophysics, 649, A3, doi: 10.1051/0004-6361/202039587

Rizzuto, A. C., Ireland, M. J., & Kraus, A. L. 2015, Monthly Notices of the Royal Astronomical Society, 448, 2737, doi: 10.1093/mnras/stv207

Rizzuto, A. C., Ireland, M. J., & Robertson, J. G. 2011, Monthly Notices of the Royal Astronomical Society, 416, 3108, doi: 10.1111/j.1365-2966.2011.19256.x

Rizzuto, A. C., Mann, A. W., Vanderburg, A., Kraus, A. L., & Covey, K. R. 2017, The Astronomical Journal, 154, 224, doi: 10.3847/1538-3881/aa9070

Rizzuto, A. C., Newton, E. R., Mann, A. W., et al. 2020, The Astronomical Journal, 160, 33, doi: 10.3847/1538-3881/ab94b7

Rodriguez, J. E., Eastman, J. D., Zhou, G., et al. 2019, Astronomical Journal, 158, 197, doi: 10.3847/1538-3881/ab4136

Santos, N. C., Sousa, S. G., Mortier, A., et al. 2013, Astronomy& Astrophysics, 556, A150, doi: 10.1051/0004-6361/201321286

Savanov, I. S., Dmitrienko, E. S., Karmakar, S., & Pandey, J. C. 2018, Astronomy Reports, 62, 532, doi: 10.1134/S1063772918080073

Scargle, J. D. 1982, The Astrophysical Journal, 263, 835, doi: 10.1086/160554

Schneider, A. C., Shkolnik, E. L., Allers, K. N., et al. 2019, The Astronomical Journal, 157, 234, doi: 10.3847/1538-3881/ab1a26

Scott, N. J., Howell, S. B., Gnilka, C. L., et al. 2021, Frontiers in Astronomy and Space Sciences, 8, 138, doi: 10.3389/fspas.2021.716560

Seager, S., & Mallén-Ornelas, G. 2003, The Astrophysical Journal, 585, 1038, doi: 10.1086/346105

Sergison, D. J., Mayne, N. J., Naylor, T., Jeffries, R. D., & Bell, C. P. M. 2013, Monthly Notices of the Royal Astronomical Society, 434, 966, doi: 10.1093/mnras/stt973

Shkolnik, E. L., Allers, K. N., Kraus, A. L., Liu, M. C., & Flagg, L. 2017, The Astronomical Journal, 154, 69, doi: 10.3847/1538-3881/aa77fa

Silverberg, S. M., Kuchner, M. J., Wisniewski, J. P., et al. 2016, The Astrophysical Journal, 830, L28, doi: 10.3847/2041-8205/830/2/L28

Siverd, R. J., Brown, T. M., Barnes, S., et al. 2018, in Society of Photo-Optical Instrumentation Engineers (SPIE) Conference Series, Vol. 10702, Ground-based and Airborne Instrumentation for Astronomy VII, ed. C. J. Evans, L. Simard, & H. Takami, 107026C, doi: 10.1117/12.2312800

Skrutskie, M. F., Cutri, R. M., Stiening, R., et al. 2006, The Astronomical Journal, 131, 1163, doi: 10.1086/498708

Skumanich, A. 1972, The Astrophysical Journal, 171, 565, doi: 10.1086/151310

Smith, J. C., Stumpe, M. C., Van Cleve, J. E., et al. 2012, Proceedings of the Astronomical Society of the Pacific, 124, 1000, doi: 10.1086/667697

Sneden, C. A. 1973, PhD thesis, THE UNIVERSITY OF TEXAS AT AUSTIN.

Soderblom, D. R. 2010, Annual Review of Astronomy and Astrophysics, 48, 581, doi: 10.1146/annurev-astro-081309-130806

Soderblom, D. R., Hillenbrand, L. A., Jeffries, R. D., Mamajek, E. E., & Naylor, T. 2014, Ages of Young Stars (eprint: arXiv:1311.7024: University of Arizona Press), doi: 10.2458/azu_uapress_9780816531240-ch010

Soderblom, D. R., & Mayor, M. 1993, The Astronomical Journal, 105, 226, doi: 10.1086/116422

Somers, G., Cao, L., & Pinsonneault, M. H. 2020, The Astrophysical Journal, 891, 29, doi: 10.3847/1538-4357/ab722e

Somers, G., Pinsonneault, M. H., & Cao, L. 2019, The SPOTS Models: A Grid of Theoretical Stellar Evolution Tracks and Isochrones For Testing The Effects of Starspots on Structure and Colors, 1.0, Zenodo, doi: 10.5281/zenodo.3593339

Sousa, S. G. 2014, [arXiv:1407.5817]. https://arxiv.org/abs/1407.5817

Sousa, S. G., Santos, N. C., Adibekyan, V., Delgado-Mena, E., & Israelian, G. 2015, Astronomy& Astrophysics, 577, A67, doi: 10.1051/0004-6361/201425463

Souto, D., Cunha, K., Smith, V. V., et al. 2018, The Astrophysical Journal, 857, 14, doi: 10.3847/1538-4357/aab612

Stassun, K. G., Oelkers, R. J., Pepper, J., et al. 2018, The Astronomical Journal, 156, 102, doi: 10.3847/1538-3881/aad050

Stauffer, J. 2000, Stellar Clusters and Associations: Convection, Rotation, and Dynamos, 198, 255. https://ui.adsabs.harvard.edu/abs/2000ASPC..198..255S/abstract

Stelzer, B., Marino, A., Micela, G., López-Santiago, J., & Liefke, C. 2013, Monthly Notices of the Royal Astronomical Society, 431, 2063, doi: 10.1093/mnras/stt225

Stumpe, M. C., Smith, J. C., Catanzarite, J. H., et al. 2014, Proceedings of the Astronomical Society of the Pacific, 126, 100, doi: 10.1086/674989

Stumpe, M. C., Smith, J. C., Van Cleve, J. E., et al. 2012, Proceedings of the Astronomical Society of the Pacific, 124, 985, doi: 10.1086/667698

Sullivan, K., & Kraus, A. 2021, arXiv:2103.09840 [astro-ph]. http://arxiv.org/abs/2103.09840

Tanaka, H., & Ward, W. R. 2004, The Astrophysical Journal, 602, 388, doi: 10.1086/380992

Tayar, J., Claytor, Z. R., Huber, D., & van Saders, J. 2022, The Astrophysical Journal, 927, 31, doi: 10.3847/1538-4357/ac4bbc

Thao, P. C., Mann, A. W., Johnson, M. C., et al. 2020, The Astronomical Journal, 159, 32, doi: 10.3847/1538-3881/ab579b

Tofflemire, B. M., Rizzuto, A. C., Newton, E. R., et al. 2021, The Astronomical Journal, 161, 171, doi: 10.3847/1538-3881/abdf53

Tognelli, E., Prada Moroni, P. G., & Degl'Innocenti, S. 2015, Monthly Notices of the Royal Astronomical Society, 449, 3741, doi: 10.1093/mnras/stv577

Tokovinin, A. 2018, Proceedings of the Astronomical Society of the Pacific, 130, 035002, doi: 10.1088/1538-3873/aaa7d9

Tokovinin, A., Fischer, D. A., Bonati, M., et al. 2013, Publications of the Astronomical Society of the Pacific, 125, 1336, doi: 10.1086/674012

Torres, C. A. O., Quast, G. R., da Silva, L., et al. 2006, VizieR Online Data Catalog, J/A+A/460/695

Torres, C. A. O., Quast, G. R., Melo, C. H. F., & Sterzik, M. F. 2008, Handbook of Star Forming Regions, Volume II, 757. http://adsabs.harvard.edu/abs/2008hsf2.book..757T

Torres, G., Andersen, J., & Giménez, A. 2010, Astronomy and Astrophysics Review, 18, 67, doi: 10.1007/s00159-009-0025-1

Twicken, J. D., Catanzarite, J. H., Clarke, B. D., et al. 2018, Proceedings of the Astronomical Society of the Pacific, 130, 064502, doi: 10.1088/1538-3873/aab694

Vanderburg, A., Huang, C. X., Rodriguez, J. E., et al. 2019, The Astrophysical Journal, 881, L19, doi: 10.3847/2041-8213/ab322d

Wang, D., Hogg, D. W., Foreman-Mackey, D., & Schölkopf, B. 2016, Proceedings of the Astronomical Society of the Pacific, 128, 094503, doi: 10.1088/1538-3873/128/967/094503

Wirth, C. P., Zhou, G., Quinn, S. N., et al. 2021, TOI-942b: A Prograde Neptune in a 60 Myr old Multi-transiting System. https://arxiv.org/abs/2106.14968

Wood, M. L., Mann, A. W., Bush, J., Fields, M., & Thao, P. C. in prep

Wood, M. L., Mann, A. W., & Kraus, A. L. 2021, The Astronomical Journal, 162, 128, doi: 10.3847/1538-3881/ac0ae9

Wood, M. L., Mann, A. W., Barber, M. G., et al. 2023, The Astronomical Journal, 165, 85, doi: 10.3847/1538-3881/aca8fc

Wright, E. L., Eisenhardt, P. R. M., Mainzer, A. K., et al. 2010, The Astronomical Journal, 140, 1868, doi: 10.1088/0004-6256/140/6/1868

Wright, N. J., & Mamajek, E. E. 2018, Monthly Notices of the Royal Astronomical Society, 476, 381, doi: 10.1093/mnras/sty207

Yu, L., Donati, J.-F., Hébrard, E. M., et al. 2017, Monthly Notices of the Royal Astronomical Society, 467, 1342, doi: 10.1093/mnras/stx009

Zapatero Osorio, M. R., Béjar, V. J. S., Pavlenko, Y., et al. 2002, Astronomy and Astrophysics, 384, 937, doi: 10.1051/0004-6361:20020046

Zhou, G., Rodriguez, J. E., Vanderburg, A., et al. 2018, The Astronomical Journal, 156, 93, doi: 10.3847/1538-3881/aad085

Zhou, G., Quinn, S. N., Irwin, J., et al. 2020, The Astronomical Journal, 161, 2, doi: 10.3847/1538-3881/abba22

Ziegler, C., Tokovinin, A., Briceño, C., et al. 2019, The Astronomical Journal, 159, 19, doi: 10.3847/1538-3881/ab55e9

Ziegler, C., Law, N. M., Baranec, C., et al. 2018, The Astronomical Journal, 156, 259, doi: 10.3847/1538-3881/aad80a

Zucker, C., Peek, J. E. G., & Loebman, S. 2022a, The Astrophysical Journal, 936, 160, doi: 10.3847/1538-4357/ac898c

Zucker, C., Goodman, A. A., Alves, J., et al. 2022b, Nature, 1, doi: 10.1038/s41586-021-04286-5

Zuckerman, B., & Song, I. 2004, Annual Review of Astronomy and Astrophysics, 42, 685, doi: 10.1146/annurev.astro.42.053102.134111